# Tensile and micro-compression behaviour of AISI 316L austenitic stainless steel single crystals at 20°C and 300°C: experiments, modeling and simulations

Jean-Michel Scherer, Jérémy Hure, Ronan Madec, Florian Le Bourdais, Laurent van Brutzel, Sergio Sao-Joao, Guillaume Kermouche, Jacques Besson, Benoît Tanguy

# Tensile and micro-compression behaviour of AISI 316L austenitic stainless steel single crystals at 20 °C and 300 °C: experiments, modeling and simulations

Jean-Michel Scherer,[a,b,*], Jérémy Hure[b], Ronan Madec[c,d], Florian Le Bourdais[e], Laurent van Brutzel[f], Sergio Sao-Joao[g], Guillaume Kermouche[g], Jacques Besson[a], Benoît Tanguy[b]

[a] *Mines Paris, Université PSL, Centre des Matériaux (MAT), UMR7633 CNRS, 91003 Evry, France*
[b] *Université Paris-Saclay, CEA, Service d'Étude des Matériaux Irradiés, 91191, Gif-sur-Yvette, France*
[c] *CEA, DAM, DIF, F-91297, Arpajon, France*
[d] *Université Paris-Saclay, CEA, Laboratoire Matière en Conditions Extrêmes, F-91680 Bruyères-le-Châtel, France*
[e] *French Alternative Energies and Nuclear Energy Commission—Laboratory for Integration of Systems and Technology (CEA List), 91191 Gif-sur-Yvette, France*
[f] *Université Paris-Saclay, CEA, Service de recherche en Corrosion et Comportement des Matériaux, 91191, Gif-sur-Yvette, France*
[g] *Mines Saint-Etienne, CNRS, UMR 5307 LGF, Centre SMS, 42023, Saint Etienne, France*

**Abstract**

The mechanical behaviour of 316L stainless steel single crystal is characterised at room temperature and 300 °C. Elasticity moduli at room temperature are obtained with resonant ultrasound spectroscopy. Their dependence on temperature is calibrated with molecular dynamics simulations. The plastic behaviour is characterised by tensile tests on millimetre-sized single crystal specimens and compression tests on micrometre-sized single crystal specimens. A constitutive model of crystal plasticity based on dislocation density hardening at finite strains is developed and implemented in an open-source material subroutine compatible with several finite element (FE) and fast Fourier transform (FFT) solvers. Tensile curves at room temperature and 300 °C are used to calibrate the interaction coefficients for self and coplanar dislocation interactions. The dislocation mean free path for obstacle dislocations and the annihilation distance are also calibrated. The calibrated model predicts tensile curves in excellent agreement with experimental data. In addition, the predicted plastic strain fields are in good agreement with the experimental fields obtained by digital image correlation. Semi-quantitative agreement between simulation and experimental data is obtained for micro-compression tests without further calibration of the model. Finally, an extension to polycrystals with grain size effects is finally proposed. The predicted strain hardening behaviour is compared with experimental data on stainless steel polycrystals.

*Keywords:* 316L stainless steel, single crystal plasticity, constitutive model, micro-mechanics, size effects

## 1. Introduction

Because of their excellent chemical and mechanical properties at relatively low cost, austenitic stainless steels are widely used as structural materials in engineering applications (Marshall, 1984). For example, their behaviour in the range of temperatures and pressures encountered in nuclear pressure vessels makes them suitable for internal structural use. The properties of these materials have led to an extensive literature aimed at measuring, understanding, modelling and improving their properties (Song et al., 2011; Trelewicz et al., 2016; Mukherjee and DebRoy, 2019; Dumas et al., 2021). In most studies, the microstuctural characterisation of steels is carried out at the crystalline level. Mechanical tests, on the other hand, are carried out on polycrystalline millimetre-sized specimens, averaging the behaviour of many grains. The reason for this striking gap between the scales of microstructural observation and mechanical characterisation is twofold. Firstly, most applications of steels involve components composed of a large number of grains and therefore do not necessarily require measurement of the mechanical behaviour of individual grains. Second, mechanical testing of individual grains is challenging for steels due to the relatively small grain size obtained during processing, typically a few tens of microns.

*Corresponding author: jean-michel.scherer@minesparis.psl.eu

Nevertheless filling this gap could have significant benefits. Indeed, fundamental mechanisms of plasticity and fracture often occur at sub-grain size scales (Pineau, 2006). Furthermore, models of material behaviour have become increasingly sophisticated. For example, the continuum theory of crystal plasticity (Roters et al., 2011) is a modelling tool of paramount importance for bridging sub-grain features to the macroscopic mechanical behaviour. However, when applied to austenitic stainless steels (Monnet and Mai, 2019), crystal plasticity models rely on material parameters, some of which remain imprecisely known due to the lack of experimental work at this scale. To some extent, the evaluation of these parameters can be carried out by inverse identification on conventional experiments on polycrystals (Han, 2012). In addition, discrete dislocation dynamics (DDD) numerical simulations allow the study of the interactions between dislocations and have been used to inform and calibrate continuum crystal plasticity models (Madec et al., 2003; Kubin et al., 2008; Madec and Kubin, 2017). However, an experimental investigation of the mechanical behaviour of austenitic stainless steel single crystals would help to validate, or if not modify, the numerical values of the material parameters used in the literature. The present work aims to perform this task.

Two approaches can be used to characterise stainless steel single crystals. Millimetre-sized single crystal samples can be tested using conventional methods, or micro-sized samples can be characterised using small-scale experimental platforms. Several techniques exist in order to grow millimetre-sized (or even larger) metallic single crystals such as the Bridgman–Stockbarger (Bridgman, 2013; Stockbarger, 1936) method or the Czochralski (Czochralski, 1918) method. They can therefore be used in order to produce ingots from which single crystal samples can be machined while controlling the orientation of the crystal lattice within the sample geometry. Experiments on pure metallic single crystals have been carried out, for example, on aluminium (Taylor and Elam, 1925), copper (Demir and Raabe, 2010), magnesium (Syed et al., 2012) and $\alpha-$iron (Keh and Nakada, 1967). Experiments on single crystals of metallic alloys are more scarce, as their preparation is often more sophisticated. The available studies mainly focus on nickel-based superalloys (Hanriot et al., 1991; Raffaitin et al., 2007) or Hadfield steels (Karaman et al., 2000; Canadinc et al., 2005). To the authors' knowledge a single study performed by Karaman et al. (2001) reports tensile test results on millimeter-sized single crystals of 316L stainless steel. Their tensile experiments were performed on nitrogen-free and nitrogen-strengthened steels at room temperature with a strain rate of $5 \times 10^{-5}\,\mathrm{s}^{-1}$ and with the tensile directions oriented along <111>, <001> and <123> crystal directions. On the other hand, some experimental techniques do not require large grains, such as for instance micropillar compression or nanoindentation. However, small scale experimental techniques are often associated with the difficulty of assessing the size effects that arise as the size of the sample becomes of the same order of magnitude as the length scale of the deformation processes. In addition, temperature control of small scale experiments is challenging (Wheeler et al., 2013; Viat et al., 2017).

If experiments on metallic single crystals are rare in the literature, in contrast, many models of crystal elasto-viscoplasticity are available and used in numerical simulations. A common feature of most models is the consideration of a set of yield criteria to account for several inelastic mechanisms, such as plastic slip on different slip systems. Some differences between the available models are due to their either phenomenological or more physical basis. For instance, (Méric et al., 1991) consider a phenomenological theory of crystal plasticity. On the other hand a variety of dislocation-based crystal plasticity theories have been formulated (Kuhlmann-Wilsdorf, 1999). Some models take into account the edge or screw nature of dislocations (Gurtin, 2006), while others introduce size dependencies by accounting for the presence of geometrically necessary dislocations (Gurtin, 2008). In addition, formulations with a critical stress (threshold) to activate plastic slip (Méric et al., 1991) and formulations without a critical stress (threshold-free) (Kothari and Anand, 1998) are available. Rate-independent settings (Anand and Kothari, 1996; Schmidt-Baldassari, 2003; Forest and Rubin, 2016) and viscoplastic frameworks (Rashid and Nemat-Nasser, 1992; Méric et al., 1991) have also been proposed.

The main objective of this study is to characterise the mechanical behaviour of austenitic stainless steel (316L) single crystals at 20 °C and 300 °C in order to calibrate a continuum crystal plasticity model based on dislocation densities. Millimeter-sized specimens are loaded in tension along different directions of the face-centered cubic

(FCC) crystal lattice. Micropillars are also subjected to compression in order to investigate the hardening behaviour along other crystallographic directions. A crystal plasticity model based on the evolution of dislocation densities is presented and calibrated by inverse identification. The numerical implementation of the constitutive behaviour is done with `MFront` (Helfer et al.), a code generator tool compatible with several FEM and FFT solvers[1]. The numerical implementation of the crystal plasticity model is shared as an open-source code (Hure and Scherer, 2023). Finally, numerical tensile and micro-compression experiments on single and polycrystalline samples are finally performed in order to further assess the validity of the model.

The paper is organised as follows. In Section 2, the material, methods and experimental results are presented, together with numerical results aimed at characterising the elastic behaviour. A crystal plasticity model and its calibration to experimental data are described in Section 3. Numerical finite element simulations of the plastic behaviour of single and polycrystals are presented in Section 4. The results presented in the previous sections are discussed in Section 5. Concluding remarks and prospects are given in Section 6.

## 2. Mechanical behaviour of 316L single crystals at room temperature and 300 °C

### *2.1. Material*

This study investigates the mechanical behaviour of single crystals of AISI 316L stainless steel. This austenitic steel has a face-centered cubic lattice, with lattice parameter $a_0 = 0.362$ nm (Borgioli et al., 2006) at room temperature. A single crystal plate (25.134 × 25.131 × 2.163 mm, mass 10.9855 g and calculated density 8.041 g cm$^{-3}$) was purchased from Princeton Scientific Corporation for mechanical characterisation. The chemical composition of this material is given in Tab. 1. Experimental data on the mechanical behaviour of 316L single crystals is scarce in the literature. To the authors' knowledge, only one study by Karaman et al. (2001) reports the characterisation of millimeter-scale 316L single crystal specimens at room temperature. The tensile curves obtained by Karaman et al. (2001) along the <111>, <001> and <123> crystal directions are digitized and plotted in Section 2.3.

Table 1: Chemical composition (weight %) of the AISI 316L single crystal austenitic stainless steel plate provided by the supplier.

| C | Mn | P | S | Si | Cr | Ni | Mo | N | Fe |
|---|---|---|---|---|---|---|---|---|---|
| ≤ 0.060 | 2.00 | 0.045 | 0.030 | 0.75 | 17.0 | 12.0 | 2.5 | 0.10 | balance |

### *2.2. Determination of elasticity moduli using Resonant Ultrasound Spectroscopy and Molecular Dynamics simulations*

The aim of this section is to determine the elastic constants of the material used in this study. First, the methodology is described.

- **Methodology**

Resonant Ultrasound Spectroscopy (RUS, Migliori et al. (1993)) is used to accurately measure the elastic constants under the hypothesis of linear elasticity. This method is based on the measurement of a spectrum of resonance frequencies of the single crystal sample described in section 2.1 using an ultrasound apparatus. A simplified model proposed by Rossin et al. (2021) relates the resonance frequencies to the elastic properties as follows

$$f_n = \frac{n}{2L}\sqrt{\frac{C^*}{\rho}}, \tag{1}$$

[1] A list of available `MFront` interfaces can be found here https://thelfer.github.io/tfel/web/index.html

where $n$ is the mode index, $L$ is the characteristic length of the single crystal sample, $\rho$ is the sample density and $C^*$ is the effective elastic stiffness along a given direction (i.e. a linear combination of elastic constants of the material). The most important insight given by Eq. (1) is that the resonance frequencies contain the information about the full elastic tensor once the geometry of the sample and its density are known. As will be explained in the following paragraphs, the methodology used, aims to find the unknown elastic constants in order to recover the measured resonance frequencies.

RUS requires (1) solving the elastic wave equation and (2) adjusting the elastic constants to predict the correct resonant frequencies. The equations describing the elastic vibrations of the single crystal are as follows (Bernard, 2014)

$$\begin{aligned} \rho\left(2\pi f\right)^2 u_i + C_{ijkl}\frac{\partial^2 u_k}{\partial x_l \partial x_j} = 0 \quad \text{in the volume} \\ C_{ijkl}\frac{\partial u_k}{\partial x_l} n_j = 0 \quad \text{on boundary of normal n,} \end{aligned} \tag{2}$$

where $u_i$ is the displacement field and the Einstein summation convention is used. Eq. (2) depends on the fourth order stiffness tensor $C_{ijkl}$ which relates the second order stress and elastic strain tensors $\sigma_{ij} = C_{ijkl}\varepsilon_{kl}$. According to Ledbetter (1984), austenitic stainless steel crystals exhibit cubic anisotropy. The stiffness tensor can therefore be parametrised with three coefficients: $C_{11}, C_{12}$ and $C_{44}$. Three additional parameters – so-called Bunge-Euler angles denoted $\phi_1, \Phi, \phi_2$ in the following – are also required to describe the orientation of the crystal in the sample frame in which Eqs. (2) are solved. Details of the dependence of $C_{ijkl}$ on these parameters are given in Appendix A. Eqs. (2) are solved in variational form using a numerically efficient Rayleigh-Ritz method for computing resonant frequencies of rectangular parallelepipeds following Visscher et al. (1991).

Let us now turn to the inverse problem of finding the elastic constants (and the orientation of the crystal) from the measured resonance frequencies. There are several approaches to solving this inverse problem in the literature, starting with gradient-based optimisation (Migliori et al. (1993)) and more recently based on a Bayesian formulation solved with Monte-Carlo Markov chain algorithms. According to Bales et al. (2018) and Goodlet et al. (2018), the Bayesian method is able to provide a robust estimate of the elastic constants. This is the motivation for using this method in the present study. In addition, the Bayesian approach provides a built-in estimation of the error in the estimated constants.

Solving the inverse problem using RUS then consists of finding the point in parameter space that maximises the posterior conditional probability obtained from Bayes' rule as

$$P(\theta|M) \propto P(M|\theta)P(\theta), \tag{3}$$

where $P(M|\theta)$ is the likelihood of a set of frequencies computed using our model with the parameter set $\theta = (C_{11}, C_{12}, C_{44}, \varphi_1, \Phi, \varphi_2, \sigma)$, and $P(\theta)$ is the *a priori* on the values of these parameters.

The likelihood of a set of frequencies (computed from parameters $\theta$) and measured frequencies $M$ is

$$P(M|\theta) = \prod_{k=1}^{N} \frac{1}{\sqrt{2\pi}\sigma} \exp\left\{-\frac{1}{2}\left(\frac{f_k^{\text{exp}} - f_k^{\text{model}}(C_{11}, C_{12}, C_{44}, \varphi_1, \Phi, \varphi_2)}{\sigma}\right)^2\right\} \tag{4}$$

where the subscript $k$ is used to denote the matched experimental $f_k^{\text{exp}}$ and computed frequencies $f_k^{\text{model}}$. As explained earlier, we assume that in Eq. (4) that the dimensions and density of the sample are known. In this work, we use a Python implementation, called `emcee`, of the affine-invariant ensemble sampler for Markov chain Monte Carlo (MCMC), first proposed by Goodman & Weare (Foreman-Mackey et al., 2013) to obtain samples following the probability distribution of Eq. (3). Details about the *a priori* distributions $P(\theta)$ used are given in Appendix A.

- **Results and analysis**

Measurements were made at room temperature. The sample spectrum was measured four times with a frequency

spacing of 17 Hz between each point between the lower and upper limits of 8 and 208 kHz. 50 resonance frequencies were extracted from each spectrum and averaged to give the experimental frequencies that were used for Bayesian inversion. The standard deviation was equal to 30 Hz on average for the 50 frequencies. Three fits were made, varying the number of frequencies $N$ used in the likelihood in Eq. 4. Each fit converged to a low value for the $\sigma$ noise parameter below 1 kHz, indicating a meaningful solution to the inverse problem.

The values obtained are shown in the following Tab. 2.

Table 2: Bayesian inversion results obtained by successive inclusion of resonance frequencies.

| parameter | N=30 inversion | N=40 inversion | N=50 inversion |
|---|---|---|---|
| $C_{11}$ (GPa) | 207.36 ± 14.53 | 218.32 ±11.08 | 200.25 ±8.91 |
| $C_{12}$ (GPa) | 134.06 ± 13.96 | 144.77 ±10.57 | 128.52 ±8.81 |
| $C_{44}$ (GPa) | 128.30 ± 4.10 | 125.38 ± 3.29 | 131.53 ±3.54 |
| $\varphi_1$ (°) | -0.05 ± 4.07 | -0.45 ± 3.82 | 6.77 ±3.64 |
| $\Phi$ (°) | 35.60 ± 1.10 | 35.09 ± 0.56 | 36.30 ±0.85 |
| $\varphi_2$ (°) | 44.65 ± 4.36 | 45.13 ± 3.72 | 38.70 ±2.89 |
| $\sigma$ (kHz) | 0.59 ± 0.15 | 0.59 ± 0.09 | 0.80 ±0.09 |

The $\sigma$ parameter represents the cumulative effect of unknown sources of uncertainty and thus qualifies the goodness of the fit obtained. Previous authors have found values for $\sigma$ in the range of those obtained here (see for example Bales et al. (2018) and Goodlet et al. (2018)). Note that the fits for $N = 30$ and $N = 40$ converge to a similar $\sigma$ value of 0.6 kHz, while the error is higher for the $N = 50$ fit. Careful analysis of the posterior plots of each frequency shows that this is due to an increase in the number of frequencies that do not fit well after frequency 40. We therefore select the $N = 40$ as the best model and report the following diagnostic plots.

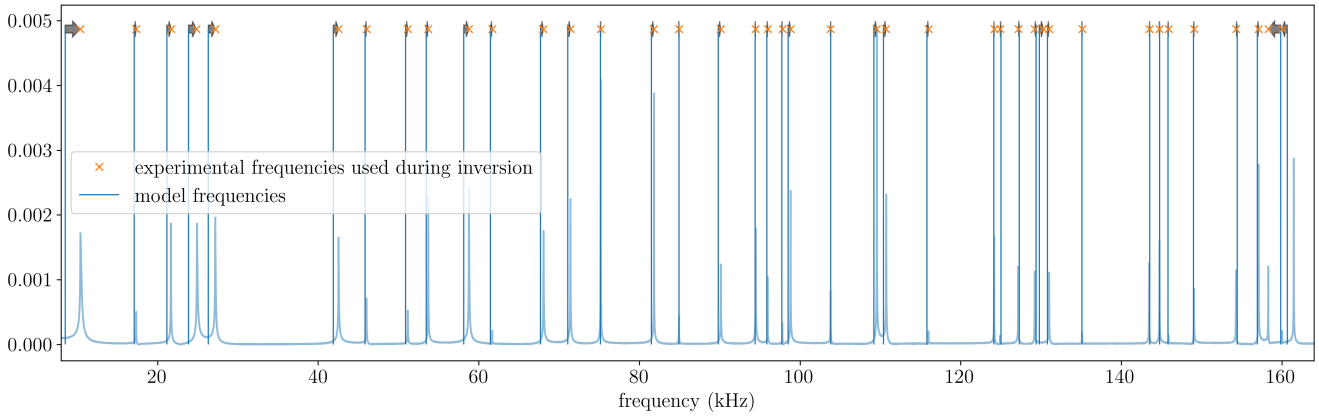


Figure 1: Experimental and best-fit model ($N = 40$) spectra obtained by resonant ultrasound spectroscopy (RUS).

As can be seen in Fig. 1, the model frequencies agree well with the measured data. To go one step further, we can plot the predictive posterior plots, which show where 95% of the representative model frequencies lie with respect to each experimental frequency (see Goodlet et al. (2018) for details on these plots).

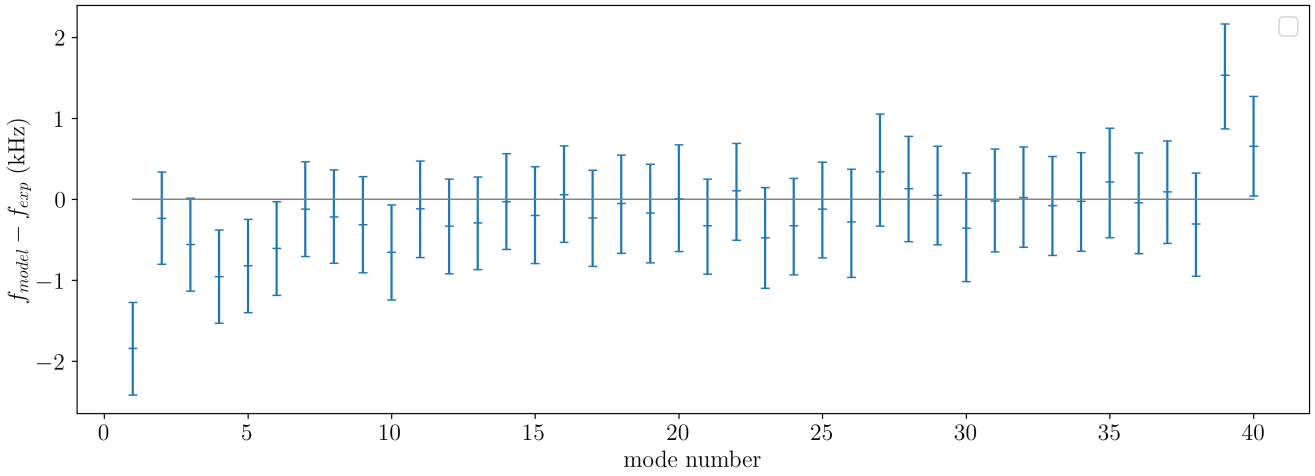


Figure 2: Difference of model and experimental frequencies for the best-fit model with $N = 40$. The relative mean square error of the median is 2.99%.

As can be seen in Fig. 2, 5 out of 40 frequencies have distributions that leave the measured frequency outside of the 95 % interval. This is surprising as we would expect at most 2 frequencies to be outside of this interval. It is difficult to be certain about the cause of this discrepancy, especially since the other frequencies do not exhibit any discernible trend as discussed in Goodlet et al. (2018). Possible reasons could be modelling errors, e.g., small deviations from the parallelepiped shape of the sample that were not taken into account in our forward model. In addition, the literature suggests that it is not uncommon for the first resonance frequency to be difficult to fit (see Bales et al. (2018)).

We can also compare the elastic constants we have found with existing work from Ledbetter (1985b). Our estimates include, in their lower bounds, the values of $C_{11} = 207$ GPa, $C_{12} = 133$ GPa, $C_{44} = 117$ GPa found by extrapolation from experimental data. In addition, the orientation of the crystal (Tab. 2) is in good agreement with that given by the manufacturer $[\varphi_1 = 0.0°, \Phi = 35.26°, \varphi_2 = 45.0°]$. This result seems to confirm the validity of our approach and the confidence we can have in the results presented in this section.

The dependence of Young's modulus and mean Poisson's ratio on loading direction can be computed using the elastic constants obtained in this section. Fig. 3 shows the 3D representation of these two elastic parameters as a function of the direction. For any direction $\mathbf{d}$, one can compute $E(\boldsymbol{d}) = 1/S_{ijkl}d_id_jd_kd_l$ and $\langle\nu(\boldsymbol{d},\boldsymbol{n})\rangle_{\boldsymbol{n}} = \langle -S_{ijkl}d_id_jn_kn_l/S_{ijkl}d_id_jd_kd_l\rangle_{\boldsymbol{n}}$, where $\mathbb{S} = \mathbb{C}^{-1}$. The surface plots are then obtained by scaling the distance between a point on the surface and the origin with $E(\boldsymbol{d})$ (resp. $\nu(\boldsymbol{d})$). As already reported in the literature, the 316 austenitic stainless steel exhibits a strong anisotropy and an auxetic behaviour (negative Poisson's ratio) for some directions.

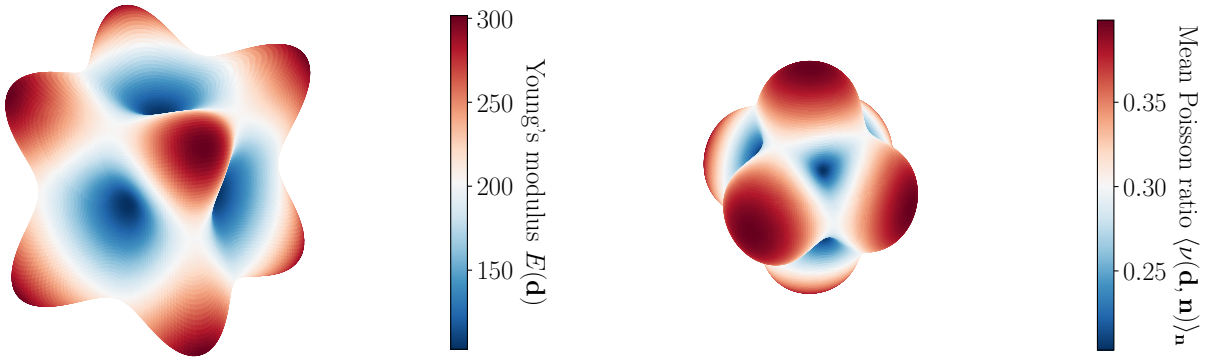


Figure 3: (a) 3D plot of Young's modulus $E(\boldsymbol{d}) = 1/S_{ijkl}d_id_jd_kd_l$, where $\mathbb{S} = \mathbb{C}^{-1}$. The softest directions (the six wells) coincide with <100> axes, while the stiffest directions (the eight peaks) coincide with <111> axes. Values are expressed in GPa. (b) 3D plot of the mean Poisson's ratio $\langle \nu(\boldsymbol{d},\boldsymbol{n})\rangle_{\boldsymbol{n}} = \left\langle -S_{ijkl}d_id_jn_kn_l/S_{ijkl}d_id_jd_kd_l \right\rangle_{\boldsymbol{n}}$. The mean value is computed over all transverse directions $\boldsymbol{n}$ orthogonal to $\boldsymbol{d}$. The Poisson ratio $\nu(\boldsymbol{d},\boldsymbol{n})$ varies in the range $[-0.189, 0.788]$.

Since the purpose of this study is also to investigate the mechanical behaviour at 300 °C, we evaluate the evolution of the elastic constant as a function of temperature. Experimental measurements of these properties in the literature are shallow and do not allow a complete description of the elastic constants with temperature. We have therefore carried out molecular dynamics (MD) simulations using empirical potentials to assess these properties. This method allows us firstly to control the structure configuration and secondly to control the temperature. However, the results of this technique are highly dependent on the reliability of the empirical potential.

For this study we have chosen the embedded atom model (EAM) interatomic potential proposed by Bonny et al. (2011), which provides accurate structural and mechanical properties at room temperature compared to experimental data (Ledbetter, 1985a). The system size used for this evaluation is $5.7\times5.7\times5.7\,\mathrm{nm}^3$ with 16 384 atoms. The atoms are randomly arranged in an FCC crystal structure to form a solid solution with composition close to the 316L alloy, namely $Fe_{0.71}Cr_{0.17}Ni_{0.12}$. For statistical purposes, 10 different configurations are constructed and investigated independently. The results for the elastic constants are then averaged over these 10 configurations for each temperature, which ranges from room temperature to 727 °C (300 °C is approximately in the middle of this range).

The elastic properties are evaluated by computing the stiffness matrix at fixed temperature in a stepwise manner. First, a small deformation ($< 0.1\%$) is imposed on the relaxed system for all the six Voigt components of the strain tensor. This step is followed by a relaxation at constant temperature and volume for 2 ps. At each time step, the six components of the stress tensor are computed with the virial stress and the kinetic energy contribution. This virial stress is shown to be equivalent to the Cauchy stress at the continuum level (Shen and Atluri, 2004; Subramaniyan and Sun, 2008) and is expressed as

$$\sigma_{ij} = \frac{1}{\Omega}\left(\frac{1}{2}\sum_{k}^{N}\sum_{\ell\neq k}^{N-1} r_i^{k\ell} f_j^{k\ell} + \sum_{k}^{N} m^k v_i^k v_j^k\right) \tag{5}$$

where $\Omega$ is the volume of the box containing the $N$ atoms. For each atom $k$, $m^k$ and $v_i^k$ represent the mass and the i$^{th}$ component of the velocity vector, respectively. For the virial contribution, $r_i^{k\ell}$ represents the i$^{th}$ component of the interatomic distance vector, $r^{k\ell} = r^\ell - r^k$, and, $f_j^{k\ell}$ represents the j$^{th}$ component of the force $f^{k\ell}$, acting on atom $k$ due to its interaction with atom $\ell$. Elastic moduli are then calculated from the slopes of the resulting stress-strain curves obtained using appropriate components of the stress and strain tensors.

Based on our simulations, the temperature dependence of the three $C_{ij}$ is nearly linear. Therefore, we compute

linear fits such that the experimental values obtained at 20 °C are retrieved. In other words, the molecular dynamics simulations are used to compute the slopes of the temperature dependence, while the experimental data are used to determine the intercepts of the linear fits. The best fits obtained are

$$C_{11}(\text{GPa}) = 233.36 - 0.0513T(\text{K}) \quad (6)$$

$$C_{12}(\text{GPa}) = 152.88 - 0.0277T(\text{K}) \quad (7)$$

$$C_{44}(\text{GPa}) = 134.43 - 0.0308T(\text{K}) \quad (8)$$

where $T$(K) denotes the temperature expressed in Kelvin. The values at 300 °C are respectively equal to $C_{11} = 204$ GPa, $C_{12} = 137$ GPa and $C_{44} = 117$ GPa.

### *2.3. Plastic behaviour in tension*

Tensile experiments were then carried out on single crystals at 300 °C to determine the plastic behavior for different orientations. Tensile experiments were not conducted at 20 °C due to a limited number of available specimens and because experimental data are already available at this temperature in the literature (Karaman et al., 2001).

- **Methodology**

The geometry of the specimens used for these experiments is shown in Figure 4.

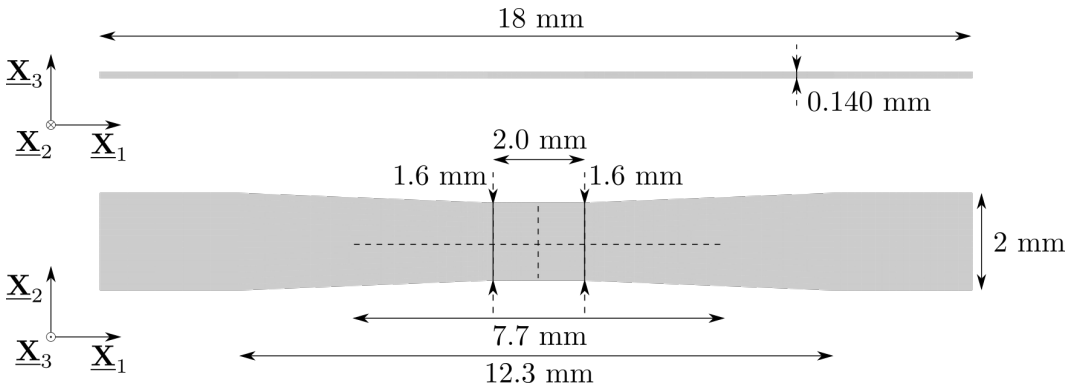


Figure 4: Sketch of the geometry and dimensions of the tensile specimens. Horizontal and vertical dashed profile lines correspond to the principal axes of the rectangular region of interest used for digital image correlation analysis.

Electron backscatter diffraction (EBSD) maps were measured on the surface of the specimens in order to obtain the local crystallographic misorientations. Figure 5 shows the measured misorientations for <111> and <011> specimens along with the corresponding inverse pole figures (IPF). The misorientation angle measures the difference between the crystallographic direction selected for tensile characterisation and the local orientation. The <111> specimen shows a 14° grain boundary located in one of the specimen heads. The second grain is characterised by a secondary spot in the IPFs. The main part of the specimen is a single crystal with less than 5° misorientation with respect to the $[\bar{1}11]$ tensile direction. The <011> specimen has a total misorientation of 12° with respect to the [011] axis. The smaller secondary spots observed in the IPF are due to the small grains observed in the lower right corner and upper left corners of the specimen. The misorientation angle is only plotted for the austenitic phase within the specimens. However the material also contains ferrite inclusions. These inclusions correspond to the white, elongated regions seen in Figures 5a and 5c. The influence of these inclusions on the mechanical response and local strain fields will be discussed later on.

For the tensile tests conducted in this study at 300 °C, $\Delta L$ denotes the variation in the length of the digital image correlation zone which has an initial length of $L_0 = 7.7$ mm. The engineering stress $P_{xx}$ is defined by the applied load $F$ normalised by the area of the minimum cross-section $S_0$. The true strain $\epsilon_{xx}$ is then computed as

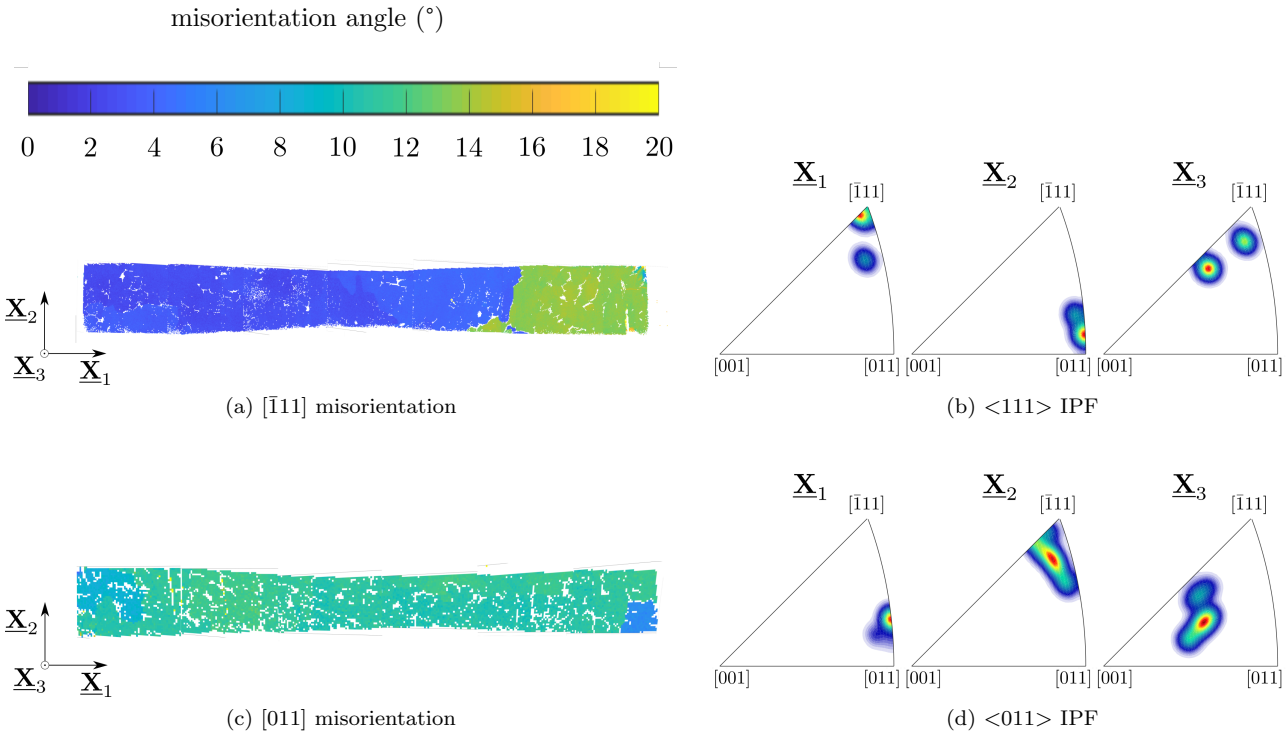


(a) [1̄11] misorientation (b) <111> IPF

(c) [011] misorientation (d) <011> IPF

Figure 5: (a) and (c) EBSD measured misorientation angle of crystal orientation in <111> and <011> specimens with respect to theoretical orientation (b) and (d) inverse pole figure for $\underline{\boldsymbol{X}}_1$, $\underline{\boldsymbol{X}}_2$ and $\underline{\boldsymbol{X}}_3$ directions in both specimens.

$\ln(1 + \Delta L/L_0)$, while the true stress $\sigma_{xx}$ is computed as $P_{xx}(1 + \Delta L/L_0)$. Displacement fields are measured on the surface of the specimens using digital image correlation (DIC). A random speckle pattern of black and white heat-resistant paint is applied using an airbrush. This technique results in a mean speckle diameter size of 20 $\mu$m. The DIC software Ncorr (Blaber et al., 2015) is used to compute the evolution of the in-plane displacements fields over time. These fields are then post-processed in order to extract the in-plane Green-Lagrange strain measure $\boldsymbol{E}^{GL} = \frac{1}{2}\left(\boldsymbol{F}^T \cdot \boldsymbol{F} - \mathbf{1}\right)$, where $\boldsymbol{F} = \partial \boldsymbol{x}/\partial \boldsymbol{X}$ is the deformation gradient. In practice, the three independent components of the 2D Green-Lagrange strain are computed from the displacement gradient $\boldsymbol{H} = \nabla u$ as follows: $E_{11}^{GL} = 0.5(2H_{11} + H_{11}^2 + H_{21}^2)$, $E_{12}^{GL} = 0.5(H_{12} + H_{21} + H_{11}H_{12} + H_{21}H_{22})$, $E_{22}^{GL} = 0.5(2H_{22} + H_{12}^2 + H_{22}^2)$.

- **Results and analysis**

The true stress *vs* true strain curves at room temperature available in the literature (Karaman et al., 2001) and obtained in this study at 300 °C are plotted in Figure 6a and 6b respectively. At both temperatures, the yield stress and the strain hardening behaviour depend strongly on the tensile direction. The yield stress is significantly lower at high temperature. However, the strain hardening rate at the yield point for the <111> orientation is similar for both temperatures. At 20 °C, the <111> and <123> orientations show two stages in the hardening regime. First a stage of intense, almost linear, strain hardening, followed by a second stage of less intense linear hardening. The <001> specimen displays only one stage of almost linear hardening. At 300 °C, a close-up view of the stress-strain curve near the yield point (see the inset in Figure 6b) shows a short range of low strain hardening followed by an almost linear hardening for both orientations <111>, <011> (in the range of applied strains). Looking back at Figure 6a, a small region of low strain hardening after the yield point appears to be present (Karaman et al., 2001). This feature of the stress-strain curves can be attributed to an easy-glide regime (stage I) during which the crystal deforms by single slip. This regime can exist for the highly symmetric orientations considered in this study due to small initial misalignments between the tensile and crystallographic directions. The non-symmetric orientation [123] shows a broader stage I regime.

Figures 7 and 8 show the three in-plane components of $\boldsymbol{E}^{GL}$ at two different macroscopic tensile strains $\Delta L/L_0$

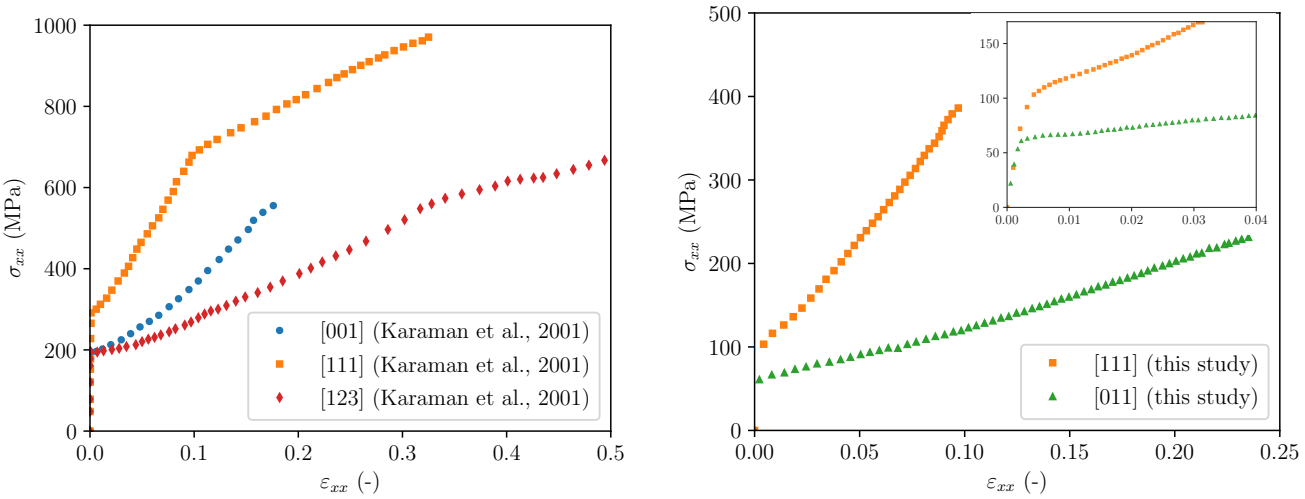


(a) 20 °C (b) 300 °C

Figure 6: Tensile curves of true stress *vs* true strain at (a) 20 °C and (b) 300 °C. The Miller indices corresponding to the directions coinciding with the tensile direction are indicated. A close-up view at the yield point is shown in the inset of figure (b).

for the <111> and <011> specimens respectively. At $\Delta L/L_0 = 0.05$, the strain fields are already very heterogeneous. For each orientation, narrow bands appear in the whole correlation region and are not restricted to the region located in the centre of the specimen, which has a smaller cross section. Overall, the width of localised strain bands is less than about 200 µm. These bands are collectively oriented along preferential directions. For each specimen, essentially two directions can be observed and several parallel bands are visible for each of them. In the <111> specimen, the bands are approximately symmetrically inclined at ±15° with respect to the tensile direction. In the <011> specimen, the bands are approximately inclined at −58° and 30° with respect to the tensile direction. The local maximum of the $E_{11}^{GL}$ strain reaches up to 0.2 in almost all bands, while outside of the bands a strain lower than 0.05 is always observed. In the <111> specimen, all bands have almost the same intensity. On the contrary, in the <011> specimen, a band located in the centre of the specimen is twice as intense as all the others. At a macroscopic strain level of 0.1, the strain heterogeneity persists for both specimens and the same narrow bands remain visible. No new bands are formed between 0.05 and 0.1 macroscopic strain. To accommodate the total strain, the intensity of each band increases. Indeed, most bands show a maximum of the $E_{11}^{GL}$ strain close to 0.3 at $\Delta L/L_0 = 0.10$. These maxima are often located at the intersection of non-parallel bands. The orientation of the bands with respect to the tensile direction does not appear to have evolved significantly.

Recently, several methods (Heaviside DIC, Relative Displacement Ratio (RDR) and slip systems based local identification of plasticity (SSLIP)) have been developed to extract the intensity of plastic slip on each slip system from DIC displacement data (Chen and Daly, 2017; Bourdin et al., 2018; Vermeij et al., 2023). Here, we use the SSLIP approach (Vermeij et al., 2023) and the associated open-source code (`https://github.com/Tijmenvermeij/SSLIP`) in order to evaluate the slip amplitude $\gamma^\alpha$ on each slip system. The SSLIP approach assumes that all the deformation is plastic, thereby neglecting elastic strains, and uses a small deformation framework for crystal plasticity. It is formulated as a local optimisation problem at each point of the material as follows

$$\inf_{\gamma^\alpha,\ \alpha=1,\dots,12} \quad \sum_{\alpha=1}^{12} |\gamma^\alpha| \tag{9}$$

$$\text{s.t.} \quad ||\boldsymbol{H}^{exp} - \boldsymbol{H}^{theor}||_{2D} < H_{thresh} \tag{10}$$

where $\boldsymbol{H}^{exp}$ is the experimentally measured displacement gradient and $\boldsymbol{H}^{theor} = \sum_{\alpha=1}^{12} \gamma^\alpha \boldsymbol{m}^\alpha \otimes \boldsymbol{n}^\alpha$. The vectors $\boldsymbol{m}^\alpha$ and $\boldsymbol{n}^\alpha$ correspond to the slip directions and slip plane normals of the FCC $\{111\}\langle 1\bar{1}0\rangle$ family of slip systems. Since only the in-plane part of $\boldsymbol{H}^{exp}$ is known from DIC fields, the $L_2$-norm of the in-plane displacement gradient

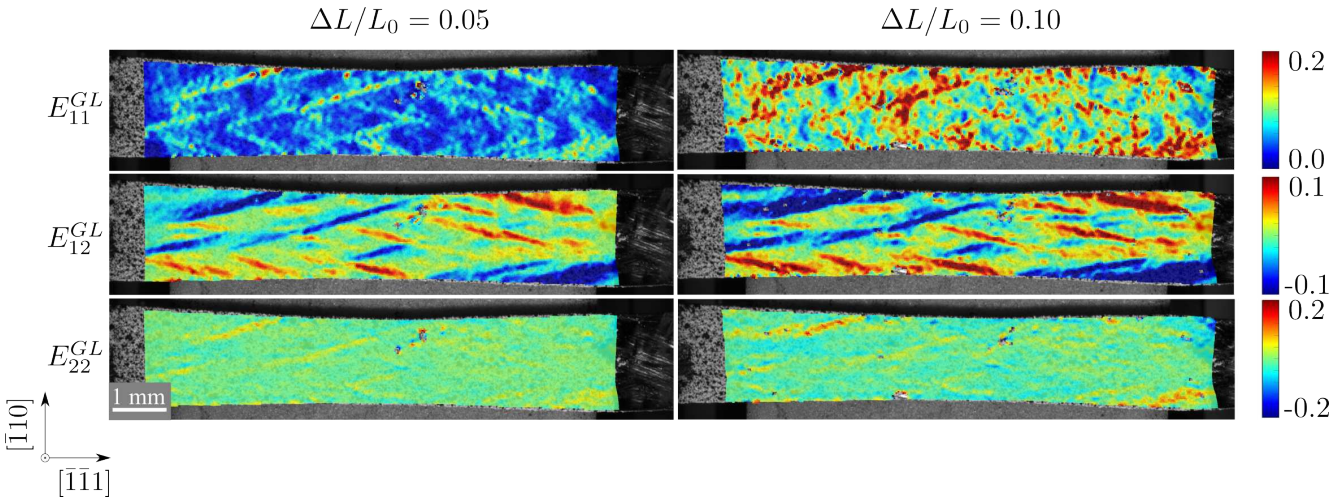


Figure 7: In-plane Green-Lagrange strain fields post-processed from DIC measurements at 300 °C for the <111> specimen at macroscopic strains $\Delta L/L_0 = 0.05$ and 0.10.

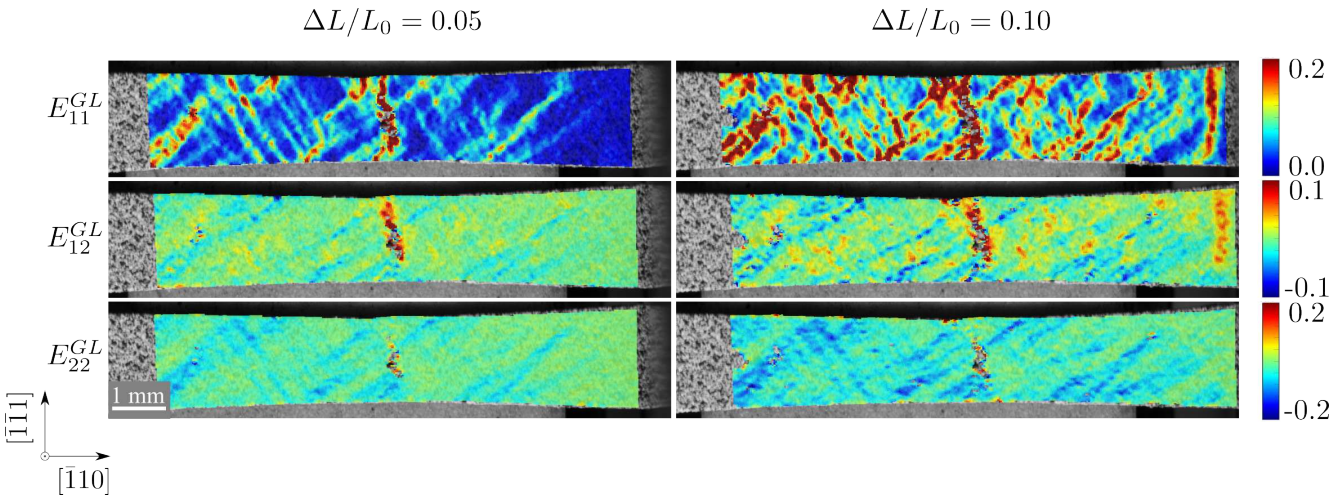


Figure 8: In-plane Green-Lagrange strain fields post-processed from DIC measurements at 300 °C for the <011> specimen at macroscopic strains $\Delta L/L_0 = 0.05$ and 0.10.

difference is used in Eq. (10). Vermeij et al. (2023) have shown that Eq. (9) and (10) generally define a well-posed problem and have been able to obtain very accurate results on virtual (HCP) experiments (with known solutions) as well as on real experiments (FCC and BCC). The main idea of this approach is to find locally a set of slip amplitudes that are consistent with the in-plane kinematics measured by DIC and for which the accumulated plastic slip is minimal. Instead of minimising the accumulated plastic slip, one could minimise the plastically dissipated energy. However, in the case of FCC crystals with 12 equivalent slip systems, both approaches are expected to give similar results (at least in the early stages of plastic yielding). An important aspect of the SSLIP method is that it treats each pixel independently. It therefore has no intrinsic notion of slip bands.

Figure 9a shows the 4 in-plane components of the displacement gradient ($H_{11}, H_{12}, H_{21}$ and $H_{22}$) obtained from the DIC data of the <111> specimen at $\Delta L/L_0 = 0.05$. These fields correspond to the inputs of the SSLIP approach described above. The outputs of the SSLIP method are shown in Figure 9b. Each field corresponds to a different slip system and the associated Schmid factor (SF) is computed. A red line and a red arrow are drawn on top of each field to denote the slip plane trace and the slip direction of the corresponding slip system respectively. In total, 8 out of 12 slip systems have plastic slip amplitude fields not equal to zero. The 6 slip systems with the highest Schmid factors clearly show the highest amplitude of plastic slip. Note that the 6 highest Schmid factors are not strictly equal because the tensile direction is not perfectly aligned with a <111> crystallographic direction (see Figure 5b). The apparent activation of two additional slip systems with low Schmid factors (systems #2 and #7) could be attributed to a stress state that is locally different from uniaxial tension (*e.g.* due to ferrite inclusions) or to crystal lattice rotation, which is not accounted for in the SSLIP approach. It may also be an artefact of the optimisation approach chosen. Nevertheless, this method provides relevant distributions of slip amplitudes across the slip systems. The two types of localised bands observed in Figure 7 are perfectly consistent with the $(\bar{1}11)$ and $(1\bar{1}1)$ slip plane traces. Two slip directions are active for each of these planes. In addition, the SSLIP method predicts the activation of two slip directions in the (111) plane. The activation of this plane is difficult to detect by looking only at the DIC fields. However, the post-mortem analysis of the specimen surface in Figure 9c clearly shows the presence of many slip lines almost perpendicular to the tensile direction. The inclination of all the observed slip line bundles agrees remarkably well with the slip plane traces predicted by the Schmid criterion. Indeed, many slip lines can be observed as straight parallel lines crossing the entire image. It is worth noting that two of these directions are almost symmetrically inclined with angles of about $\pm 18°$ with respect to the tensile direction represented by the white vertical arrow. These two directions coincide remarkably well with the directions of the more macroscopic bands observed in the DIC strain fields. In fact, the narrow bands described in the previous section are caused by the formation of slip line bundles as shown in Figure 9c. For reference, the FCC slip systems and their corresponding indices used throughout this study are listed in Figure 9d.

It is well known that deformation occurs at the lowest energy cost. However, from an energetic point of view, the most penalising dislocation interaction is the collinear interaction, in which two dislocations with collinear Burgers vectors glide in intersecting planes (Madec et al., 2003). In the <111> specimen, three pairs of active slip systems form a collinear interaction (#1, #3), (#4, #5) and (#8, #11). The SSLIP analysis shows that plastic slip on slip systems #8 and #11 occurs in complementary regions of the specimen. Similar trends can also be observed for the other two pairs of slip systems forming a collinear interaction. This observation is consistent with the higher strength of the collinear interaction and has already been noted by Dequiedt et al. (2015).

The same SSLIP analysis is performed on the <011> specimen, using the displacement gradient field shown in Figure 10a used as input and the computed slip amplitudes in Figure 10b obtained as output. For this orientation, there are mainly five slip systems with non-zero slip amplitude. The four systems with higher Schmid factors concentrate most of the slip activity. Again, the maximum Schmid factors are not perfectly equal due to a slight misorientation between the tensile axis and the <011> direction (see Figure 5d). The decomposition of the plastic activity is also relevant in this case. For slip systems #1 and #2 the slip plane trace is almost parallel to the localised deformation bands. For systems #3 and #11 the alignment between the slip plane trace and the localised deformation band is less perfect. This may be an artefact of the SSLIP method, but can also be due to lattice

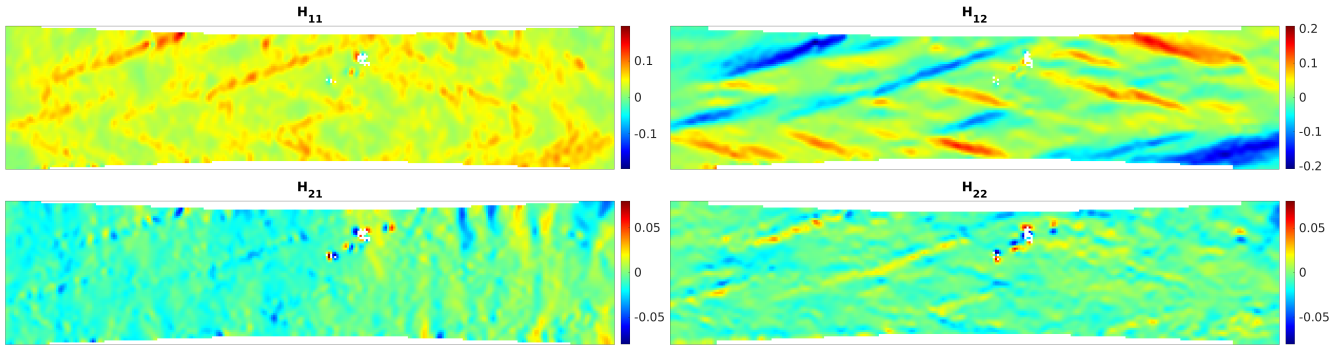


(a)

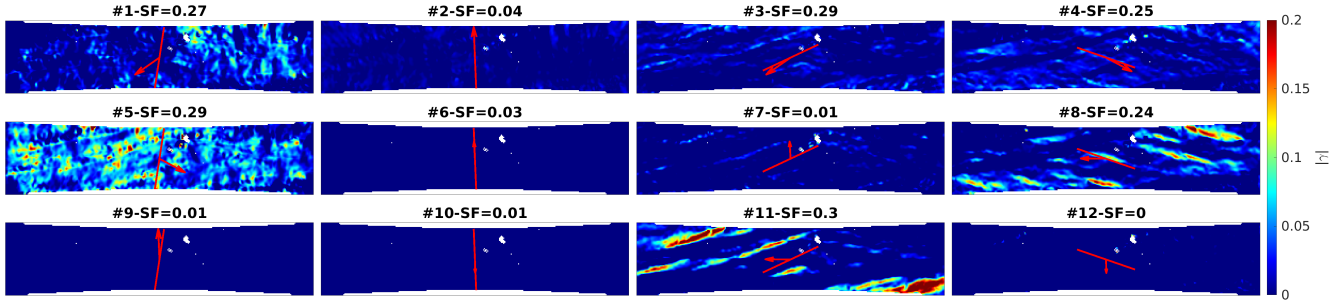


(b)

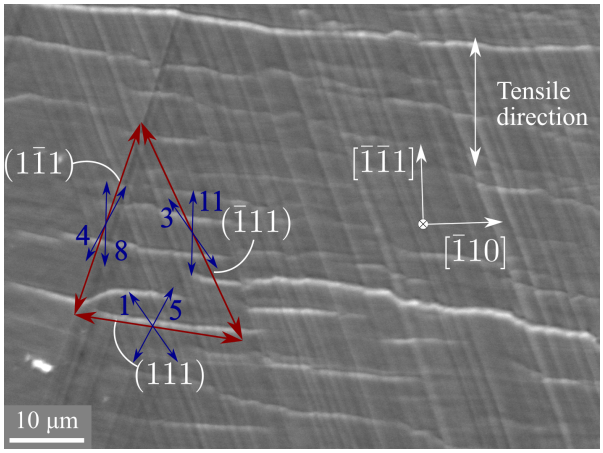


(c)

| Slip systems # | Slip directions $\boldsymbol{m}^\alpha$ | Slip planes $\boldsymbol{n}^\alpha$ |
|---|---|---|
| 1 | [01$\bar{1}$] | (111) |
| 2 | [1$\bar{1}$0] | (11$\bar{1}$) |
| 3 | [01$\bar{1}$] | ($\bar{1}$11) |
| 4 | [$\bar{1}$01] | (1$\bar{1}$1) |
| 5 | [$\bar{1}$01] | (111) |
| 6 | [101] | (11$\bar{1}$) |
| 7 | [101] | ($\bar{1}$11) |
| 8 | [110] | (1$\bar{1}$1) |
| 9 | [1$\bar{1}$0] | (111) |
| 10 | [011] | (11$\bar{1}$) |
| 11 | [110] | ($\bar{1}$11) |
| 12 | [011] | (1$\bar{1}$1) |

(d)

Figure 9: (a) Components of the in-plane displacement gradient in the the <111> specimen at $\Delta L/L_0 = 0.05$ used for the SSLIP analysis (Vermeij et al., 2023). (b) Slip system activity on each slip system obtained by post-processing the DIC field with the SSLIP analysis. The Schmid factor (SF) is computed for each slip system. The colour scale represents the absolute plastic slip magnitude. (c) Slip lines observed post-mortem on the specimen surface by SEM. Red arrows (resp. blue arrows) indicate the slip plane trace (resp. slip direction) of the six slip systems with the highest Schmid factors. (d) Nomenclature of the 12 FCC slip systems of the {111}<1$\bar{1}$0 family.

rotation to some extent. A scanning electron microscopy (SEM) analysis carried out post-mortem on the surface of the specimen, within a localised deformation band, shows in Figure 10c how the slip lines are almost aligned with the slip traces predicted by the Schmid criterion. It can be seen that the slip lines are slightly more oriented towards the tensile direction than what is predicted by the Schmid criterion. This effect may be due to the lattice rotation during loading.

In the <011> specimen the four active slip systems have different Burgers vectors, so there are no collinear interactions. The second strongest dislocation interaction is the Lomer junction. This junction occurs for the slip systems pairs (#10,#11) and (#2,#3). From the SSLIP analysis it can observed that for slips systems #10 and #11 the plastic slip occurs predominantly in complementary regions. This mutual exclusion is emphasized for this pair, because #11 is the most activated slip system.

### *2.4. Plastic behaviour in micro-compression*

Micro-compression tests were then carried out on singles crystals at 20 °C and 300 °C. First, the methodology is described

- **Methodology**

It is well known that size effects become significant as the specimen characteristic size approaches the characteristic size of the plastic mechanism (Nix and Gao, 1998). Micropillar compression is widely used in the literature to characterise the behaviour of single crystals (Dehm et al., 2018). However, due to the size of micropillars, typically between 1 and 10 µm, size effects can contribute to the mechanical behaviour measured in this type of experiment (Greer and De Hosson, 2011). The contribution of size effects can be assessed by comparing the behaviour of micropillars of different diameters. We perform the compression of micropillar specimens of diameters $\phi \simeq 3$, 6.5 and 12 µm at room temperature and at 300 °C. Two crystallographic directions <112> and <111> are tested.

Micropillar specimens were machined on the mirror-polished surface of the same stainless steel single crystal as used for the tensile tests presented in Section 2.3. The micropillars were machined by Focus Ion Beam (FIB) machining using a Thermo Scientific Helios NanoLab DualBeam microscope. The micropillar specimens have the shape of a truncated cone with a cone angle of ∼5°. The micropillar diameters are measured at the top of the specimens and range from 2.9 µm to 12.8 µm. The aspect ratio of pillar height to diameter ranges from 1.67:1 to 3.02:1. Figure 11 shows representative specimens for the three diameters considered in this study. The thickness of the material beneath a micropillar specimen is always at least 60 times greater than the maximum height of a specimen. The neighbourhood of a micropillar specimen always has the same crystallographic orientation as the micropillar itself, because the specimens are machined within a single crystal plate.

Micropillar compression tests were performed using an ALEMNIS in-situ nanoindenter apparatus in a Zeiss Gemini supra 55VP scanning electron microscope (SEM). Micro-compression tests were conducted at 20 °C and 300 °C. For high temperature tests, the temperature of the specimen and the indenter is controlled to ensure a homogeneous and steady temperature throughout the specimen. The flat punch is moved at a constant speed of 50 µm s$^{-1}$ in a direction coaxial with the micropillar specimen. The offset between the cone axis and the flat punch axis is less than 1°. The flat punch diameter is 15 µm. A more detailed description of this type of equipment can be found in Wheeler and Michler (2013).

- **Results and analysis**

Figure 12 and 13 show the stress-strain curves of micropillar specimens with the cone axis close to a <112> crystallographic axis at 20 °C and 300 °C respectively. The exact Bunge-Euler angles of this set of specimens are $\phi_1 = 98°$, $\Phi = 35.0°$ and $\phi_2 = 38.0°$. Stress is defined as the compressive load (counted positively) normalised by the surface area of the cross section at the top of the specimen $S_0$. The strain is defined as the compressive displacement (counted positively) normalized by the initial specimen height $H_0$. Several specimens are tested for

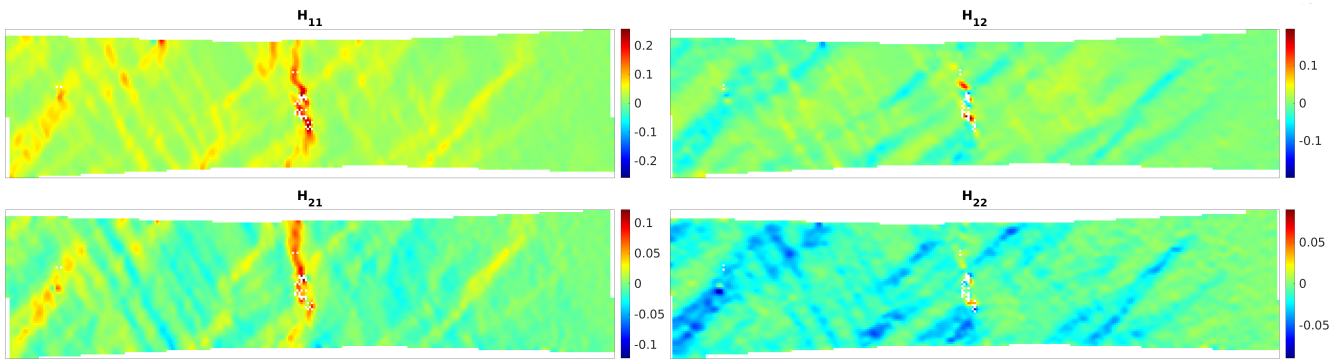


(a)

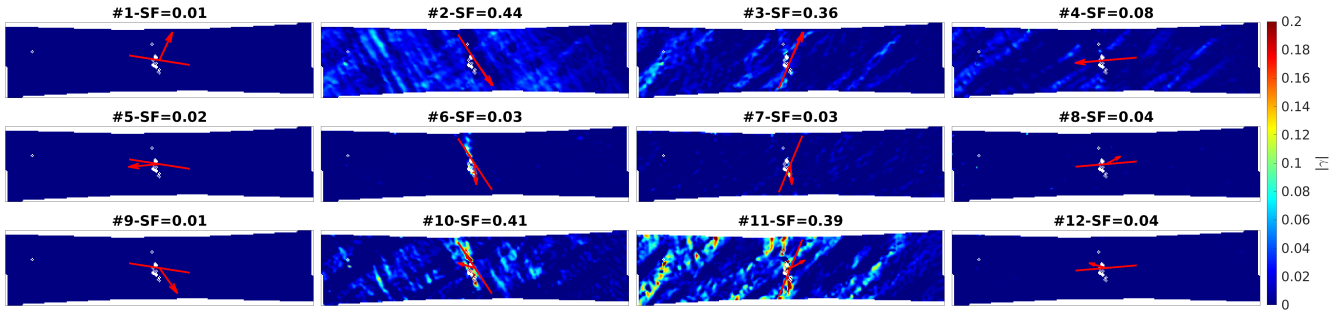


(b)

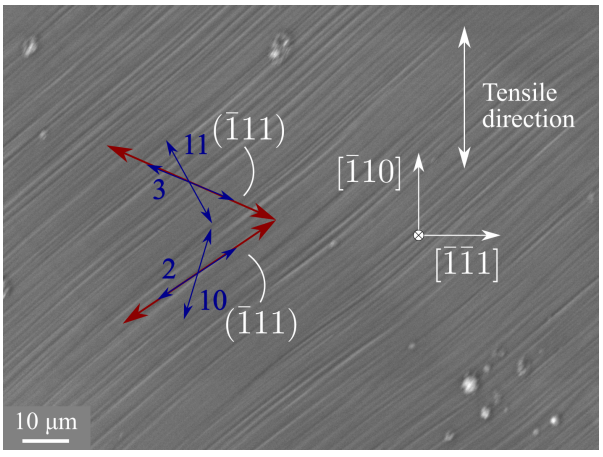


(c)

Figure 10: (a) Components of the in-plane displacement gradient in the <011> specimen at $\Delta L/L_0 = 0.05$ used for the SSLIP analysis (Vermeij et al., 2023). (b) Slip system activity on each slip system obtained by post-processing the DIC field with the SSLIP analysis. The Schmid factor (SF) is computed for each slip system. The colour scale represents the absolute plastic slip magnitude. (c) Slip lines observed post-mortem on the specimen surface by SEM. Red arrows (resp. blue arrows) indicate the slip plane trace (resp. slip direction) of the four slip systems with the highest Schmid factors.

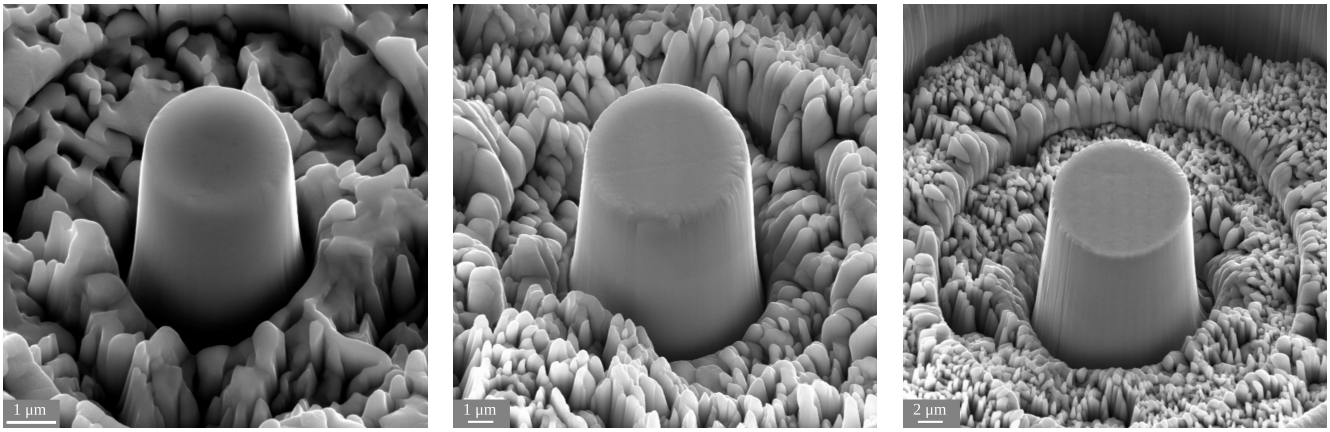


(a) $\phi = 2.9\,\mu m$ (b) $\phi = 6.5\,\mu m$ (c) $\phi = 11.1\,\mu m$

Figure 11: Representative micropillar specimens with diameter $\phi \in [2.9, 11.1]$ µm. The diameter is measured at the top of the conical micropillars. The cone angle is 5°.

each micropillar diameter. The FIB machining process introduces some variability in the shape of specimens, which are therefore not completely geometrically identical.

At both temperatures, the stress-strain curves can be divided into four distinct phases. First, the macroscopic mechanical behaviour is essentially elastic. The second phase is characterised by an apparent hardening with saturation to a plateau value. This is followed by a steep linear increase in load. Finally, the elastic unloading returns the specimen linearly to zero load.

With the exception of one specimen ($\phi = 3.0\,\mu m$ at 300 °C), the linear increase of the load during phase 1 is steeper for smaller micropillar specimens. As we plot the load against the indenter displacement, this elastic slope also includes the intrinsic compliance of the machine. In Figures 12 to 15 the contribution of the machine compliance is not subtracted from experimental results. In section 4.2, this correction is made to compare experimental and numerical results.

It can then be seen that the stress at the apparent yield point, which marks the transition from phase 1 to phase 2, decreases as the specimen diameter $\phi$ increases. This is in qualitative agreement with the expected size effect of the type *smaller is stronger*. The yield stress decreases more between $\phi = 3\,\mu m$ and $\phi = 6.5\,\mu m$ than between $\phi = 6.5\,\mu m$ and $\phi = 12\,\mu m$, thus indicating a possible elimination of size effects at $\phi = 12\,\mu m$.

The range of strains over which the phase 2 extends decreases as $\phi$ increases. Furthermore, the smaller micropillar specimens show a steeper strain hardening slope than the larger specimens. This observation is also consistent with the expected type of size effects. Interestingly, the larger specimens show a complete absence of apparent strain hardening during phase 2. A brief softening regime can even be observed at 20 °C in Figure 12c and for one of the specimens after the yield point at 300 °C in Figure 13c.

Despite some level of variability between different specimens, the strain hardening slope observed during phase 3 is similar across the two temperatures and the three diameters considered in this study. The origin of this secondary hardening phase could be due to the formation of a kink band. This mechanism is discussed in more detail in Section 4.2. The elastic unloading phase follows the same observation as the elastic loading phase. A steeper elastic slope is observed for the smaller specimens.

Figure 14 and 15 show the stress-strain curves of micropillar specimens with the cone axis close to a <111> crystallographic axis. The exact Bunge-Euler angles of this set of specimens are $\phi_1 = 125°$, $\Phi = 85°$ and $\phi_2 = 135°$. Several specimens are tested for the three diameters considered in this study. With quantitative differences to be discussed below, the same four stages described for the <112> orientation are also observed for the <111> orientation.

Although the <111> orientation is the stiffest crystallographic direction for a crystal with a Zener ratio greater than 1 (El Shawish et al., 2021), the apparent elastic stage has a lower slope than the <112> orientation. As the

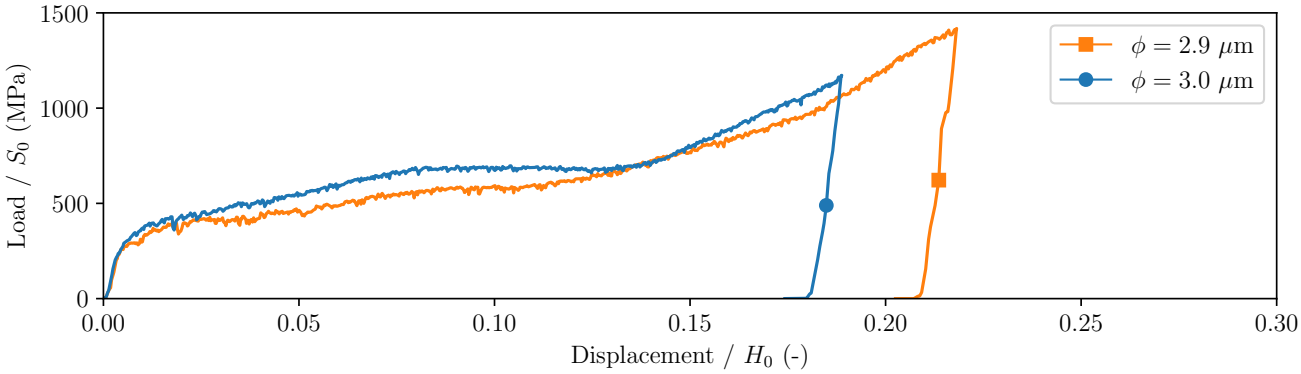


(a) $\phi \sim 3\,\mu m$

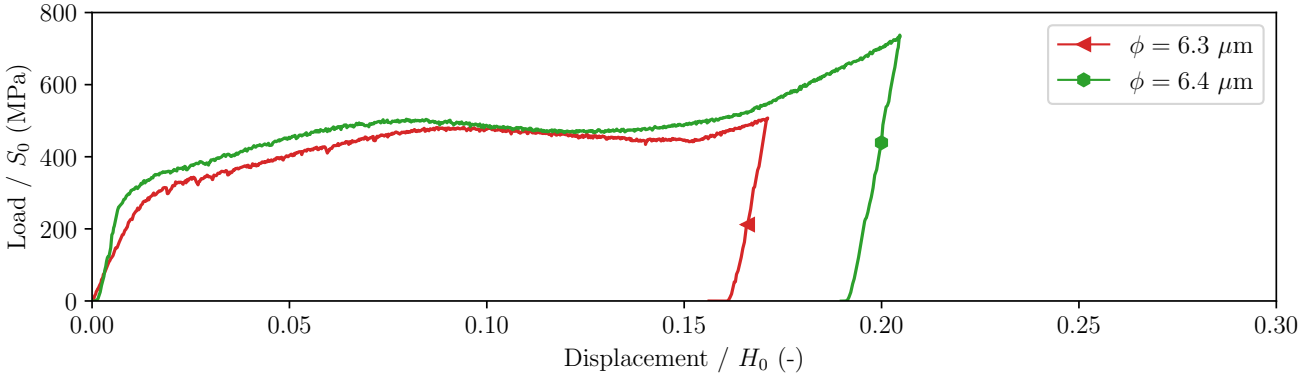


(b) $\phi \sim 6.5\,\mu m$

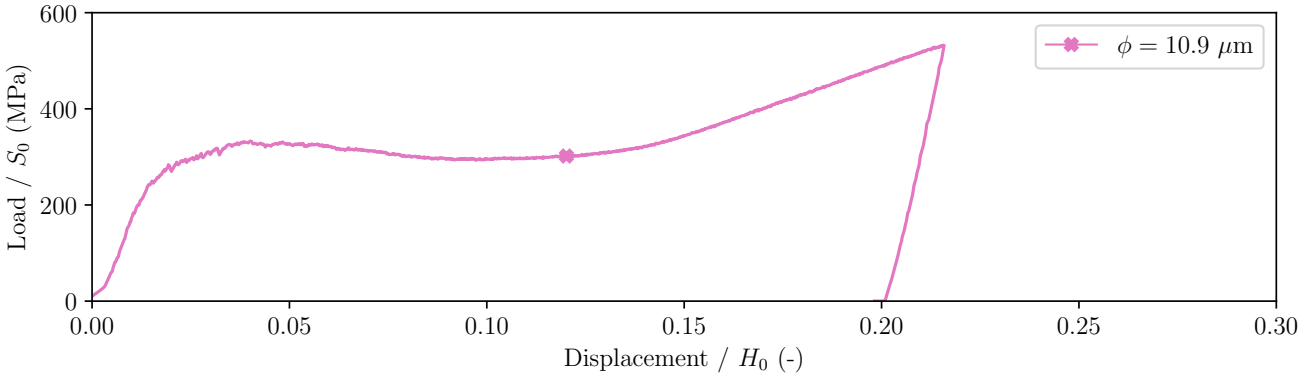


(c) $\phi \sim 12\,\mu m$

Figure 12: Load normalised by micropillar cross-section at the base *vs* displacement normalised by the micropillar height at 20 °C. The micropillar compression axis coincides with a <112> crystal axis. Micropillar diameter $\phi$ equal to (a) ∼3 µm, (b) ∼6.5 µm and (c) ∼12 µm.

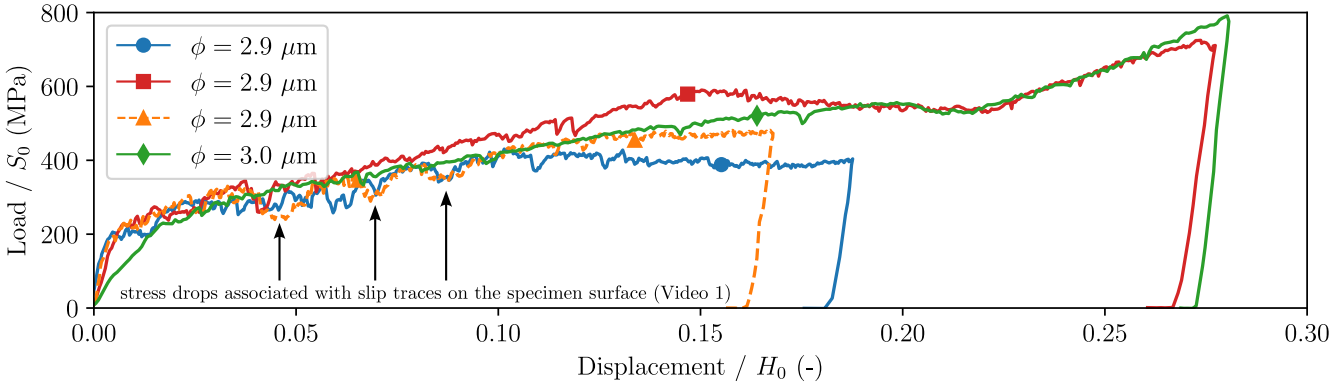


(a) $\phi \sim 3\,\mu m$

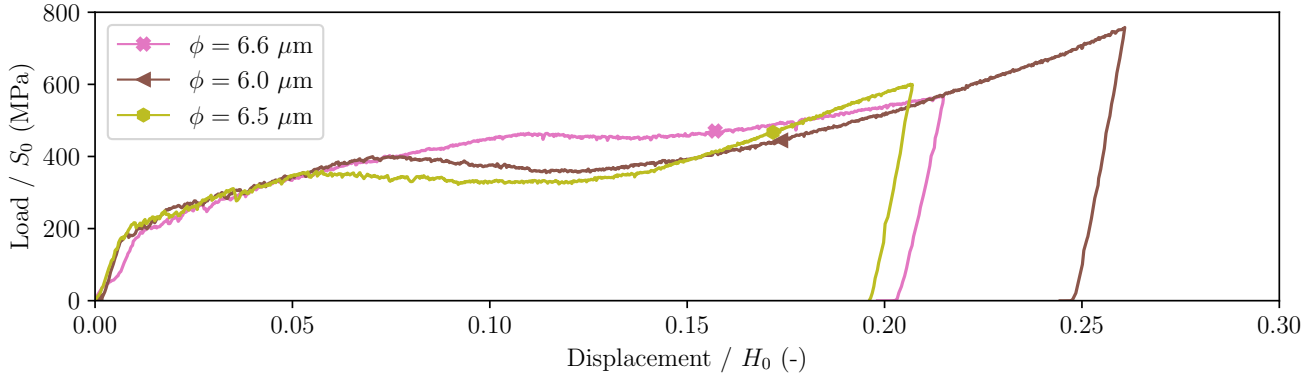


(b) $\phi \sim 6.5\,\mu m$

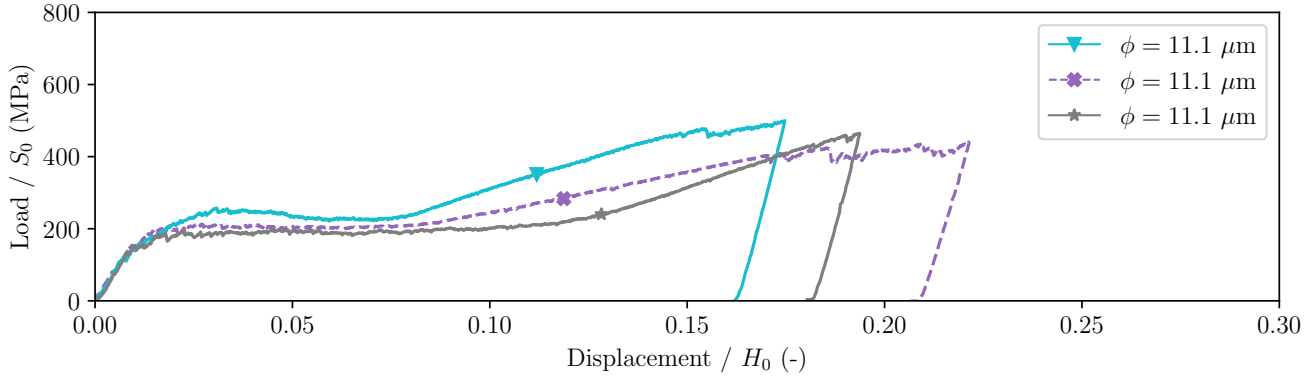


(c) $\phi \sim 12\,\mu m$

Figure 13: Load normalised by micropillar cross-section at the base *vs* displacement normalised by the micropillar height at 300 °C. The micropillar compression axis coincides with a <112> crystal axis. Micropillar diameter $\phi$ equal to (a) ~3 µm, (b) ~6.5 µm and (c) ~12 µm.

elastic phase has a lower slope for the <111> orientation, the transition between phase 1 and phase 2 is more difficult to define accurately. Nevertheless, it appears that plastic yielding occurs at a lower stress for the <111> orientation than for the <112> orientation. This is particularly interesting as the Schmid factor for the <111> orientation under uniaxial loading (equal to $2/3\sqrt{6}$) is 1.5 times lower than the Schmid factor for the <112> orientation (equal to $1/\sqrt{6}$). This may indicate that the shape of the specimens contributes significantly to the apparent behaviour. Alternatively, despite having a lower maximum Schmid factor, the <111> orientation has three times more equivalent slip systems with high Schmid factors than the <112> orientation. In small micropillar specimens, with a low dislocation density, a larger number of available slip planes could also explain why the <111> orientation shows a lower stress at plastic yield. Early and localised yielding could explain why the slope during phase 1 is lower for the <111> orientation.

At 20 °C (see Figure 14), the stress-strain behaviour of micropillar specimens with $\phi = 3\,\mu m$ shows significant variability. This could be due to a combination of effects such as variations in specimen geometry and size effects. With the exception of one specimen ($\phi = 3.3\,\mu m$ in Figure 14a), the post-yielding behaviour is characterised by a stress plateau followed by a sudden increase of the stress. Specimens with $\phi = 6.5\,\mu m$ in Figure 14b show a reduced variability. However, a clear transition from phase 2 to phase 3 is more difficult to define for these specimens. This is due to the fact that the post-yielding behaviour is not characterised by a plateau, but by a linear increase in stress. For sufficiently large strains, the apparent hardening becomes greater, suggesting a transition between a phase 2 and a phase 3. Specimens with $\phi = 12\,\mu m$ show a low apparent hardening after the yield point, followed by an increased hardening slope.

At 300 °C (see Figure 15), micropillar specimens with $\phi = 3\,\mu m$ and $\phi = 6.5\,\mu m$ show a phase 2 with a quasi-linear strain hardening behaviour without saturation. At this temperature, the transient hardening saturation observed for the <112> orientation is not observed for the <111> orientation for the smaller micropillar diameters. However, specimens with $\phi = 12\,\mu m$ show an almost flat stress level during phase 2. The specimen with $\phi = 6.2\,\mu m$ was subjected to a cyclic loading, hence the multiple elastic unloading and reloading slopes observed in Figure 15b.

For the smaller specimens, the transition between phase 2 and phase 3 at high temperature is smoother for the <111> orientation than for the <112> orientation. This is due to the lack of saturation of the apparent hardening during phase 2. A sharp transition is observed for the larger specimens. Similar to the <112> orientation, the apparent hardening slope during phase 3 appears to be size independent.

At both temperatures, the elastic unloading shows a much steeper slope than that observed during phase 1. This supports the existence of early and localised yielding during phase 1 for the <111> orientation. It is also interesting to observe that, at 20 °C and 300 °C, all the stress-strain curves show an inflection at the end of the elastic phase, between 2 and 3 % macroscopic strain.

The micro-compression tests were filmed throughout the whole loading history. In Figure 16 we show the slip lines appearing on the surface of <112> micropillar specimens at the onset of plasticity (a) and (c) and at the end of the test (b) and (d) for small and a large diameter specimens. In Figure 16a the specimen diameter (at the top) is $\phi = 2.9\,\mu m$, while in Figure 16c the specimen diameter is $\phi = 11.1\,\mu m$. Red and blue arrows indicate the location of visible slip lines. The colour of the arrow corresponds to the colour of the slip plane in Figure 16e which shows the inclination of the four {111} planes within the specimens. For both specimens, the first slip system to become active is the one with the highest Schmid factor, namely the $(\bar{1}11)[\bar{1}0\bar{1}]$ system, with a Schmid factor of -0.44. The predicted angle of 32° between the specimen axis and the slip plane trace agrees very well with the observed orientation of the slip lines at the onset of plastic slip. The specimen with the smallest diameter only shows only one type of parallel slip lines from the onset of plastic slip till the end of the test. The plastic activity is very localised in a few apparent slip lines. In Supplementary Video 1, it can be clearly seen that the onset of two intense slip lines is associated with sudden load drops. Throughout the load history, the slip lines show a significant amount of clockwise rotation around an axis almost perpendicular to the image. The same type of slip line rotation is observed in the specimen with the largest diameter. In addition, a secondary type of slip line is observed on the surface of this specimen at the very end of the test. One such a slip line is indicated by blue arrows in Figure 16d.

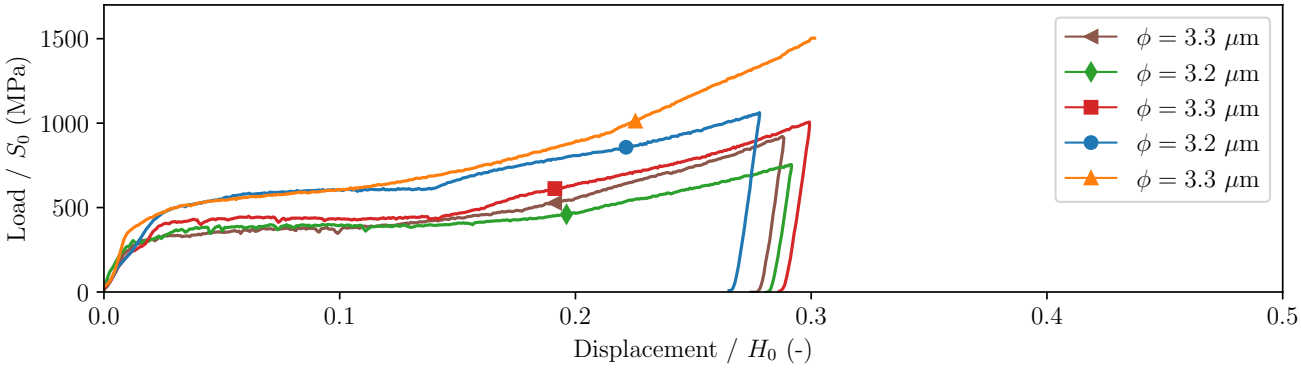


(a) $\phi \sim 3\,\mu m$

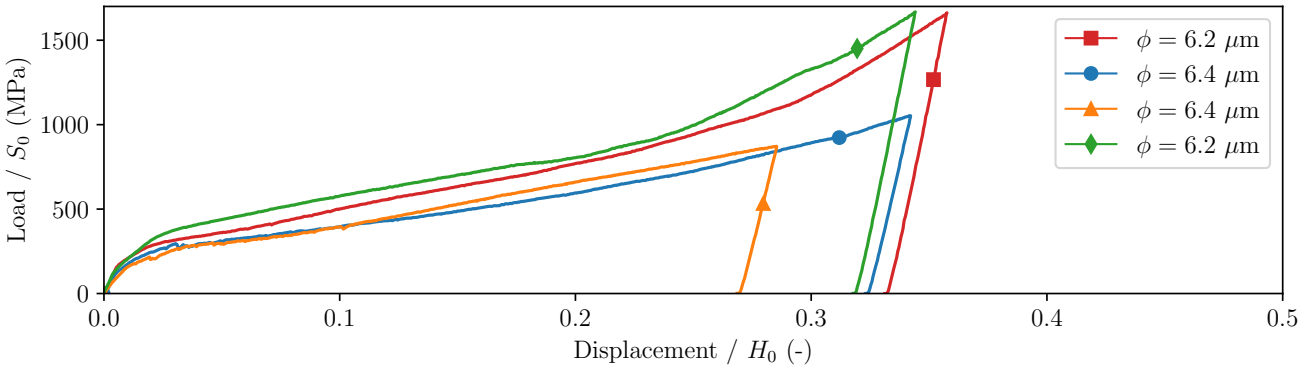


(b) $\phi \sim 6.5\,\mu m$

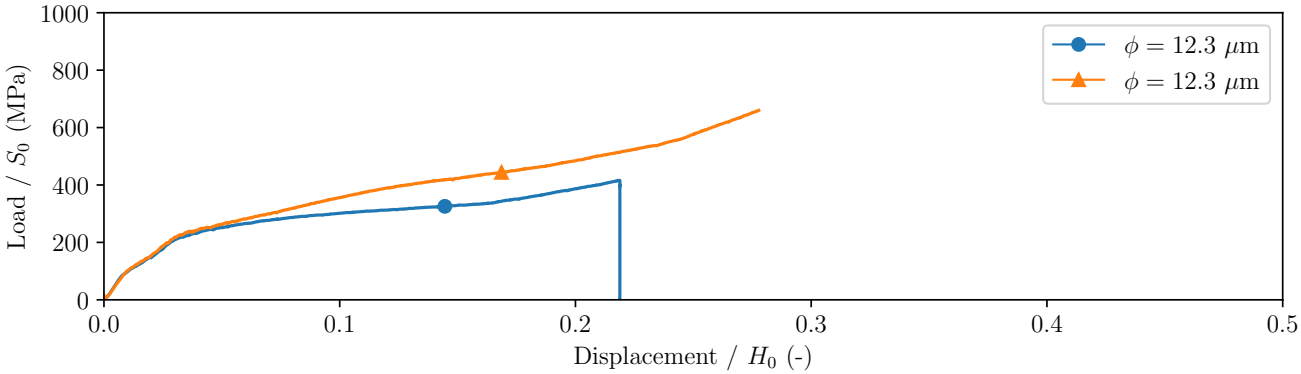


(c) $\phi \sim 12\,\mu m$

Figure 14: Load normalised by micropillar cross-section at the base *vs* displacement normalised by the micropillar height at 20 °C. The micropillar compression axis coincides with a <111> crystal axis. Micropillar diameter $\phi$ equal to (a) ∼3 µm, (b) ∼6.5 µm and (c) ∼12 µm.

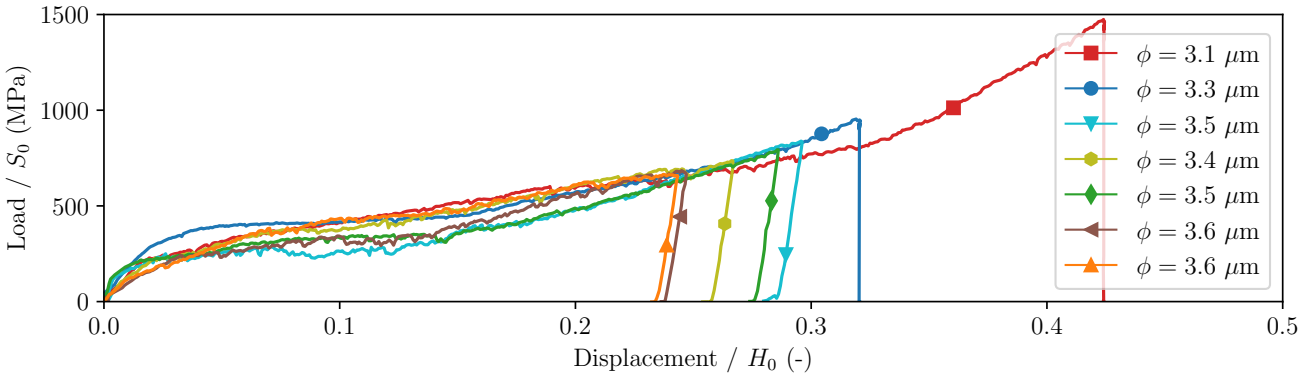


(a) $\phi \sim 3\,\mu$m

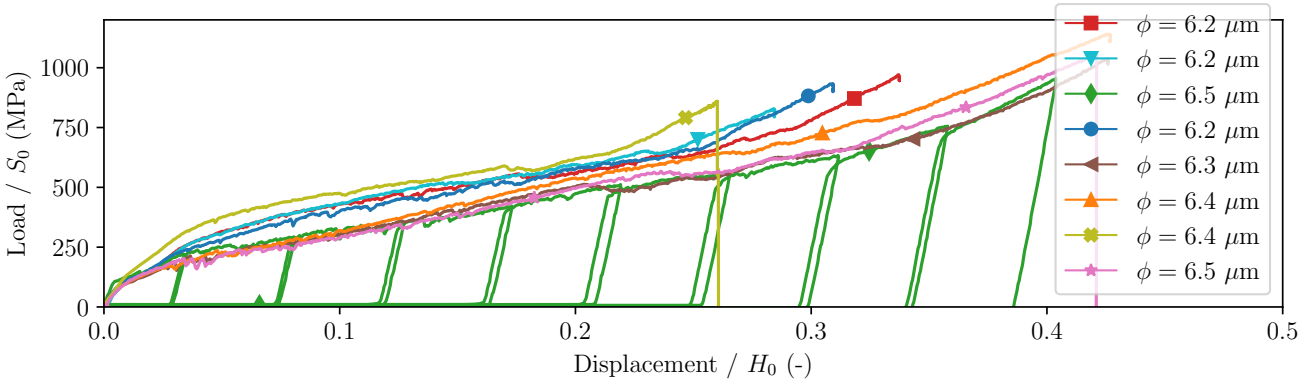


(b) $\phi \sim 6.5\,\mu$m

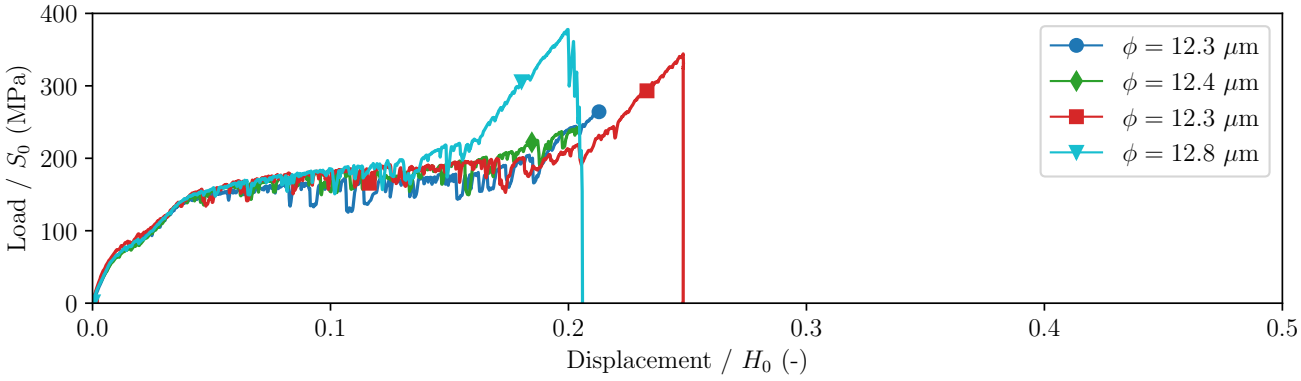


(c) $\phi \sim 12\,\mu$m

Figure 15: Load normalised by micropillar cross-section at the base *vs* displacement normalised by the micropillar height at 300 °C. The micropillar compression axis coincides with a <111> crystal axis. Micropillar diameter $\phi$ equal to (a) ∼3 µm, (b) ∼6.5 µm and (c) ∼12 µm.

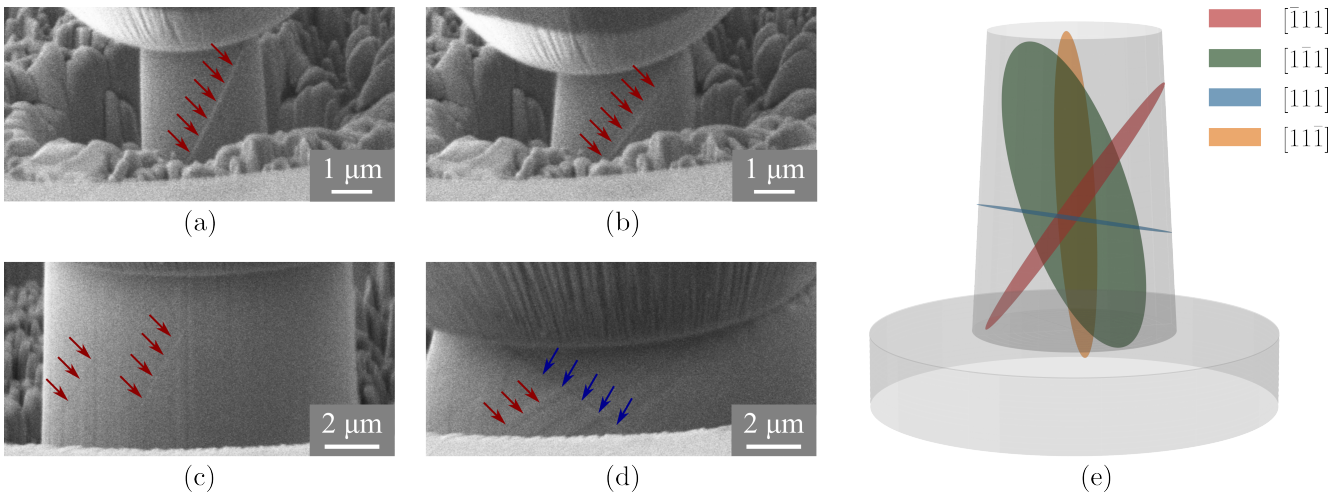


Figure 16: Slip lines observed (a) at the onset of plastic slip and (b) at the end of a micro-compression test at 300 °C on a <112> axis and a specimen diameter of $\phi = 2.9\,\mu m$ (dashed orange line in Figure 13a). Arrows indicate the position of visible slip lines. Slip lines observed (c) at the onset of plastic slip and (d) at the end of a micro-compression test at 300 °C on a <112> axis and a specimen diameter $\phi = 11.1\,\mu m$ (dashed purple line in Figure 13c). Red and blue arrows indicate the position of visible slip lines. (e) Schematic of slip planes within the <112> micropillar. The colours of the arrows in (a) to (d) correspond to the colours of the planes in (e).

The sequence of lattice rotation and secondary slip activation is clearly observed in Supplementary Video 2. The angle formed by the secondary slip lines with the specimen axis does not correspond to any of the slip planes in the initial configuration shown in Figure 16e. However, from the rotation of the first type of slip lines, we can confirm that a significant amount of lattice rotation has occurred. This rotation has probably reduced the angle between the (111) slip plane and the specimen axis. The Schmid factor (-0.31) of the (111)[10$\bar{1}$] slip system, ranked $3^{rd}$ in the initial configuration, has probably increased significantly due to the load-induced lattice rotation. In contrast, the Schmid factor (-0.37) of the (1$\bar{1}$1)[0$\bar{1}\bar{1}$] slip system, ranked $2^{nd}$ in the initial configuration, has decreased upon loading because the angle between the (1$\bar{1}$1) plane and the cone axis has decreased due to the lattice rotation. This explains why the second type of slip line, which appears at the very end of the test, coincides with the (rotated) (111) plane.

Lattice rotation often occurs in kink bands, *i.e.* bands where the deformation is localised in a direction perpendicular to the slip direction. The formation of such bands could be the origin of the transition between the phase 2 with limited apparent hardening and phase 3 with strong apparent hardening. This mechanism is discussed in more detail in Section 4.2.

In Figure 17 we plot the resolved shear at onset of plastic yielding $\tau_0^c$ in micro-compression and tensile tests. We define the threshold $\tau_0^c$ as the applied stress at onset of plastic yielding ($R_{p0.2}$) multiplied by the maximum Schmid factor. $\tau_0^c$ depends on temperature because of the temperature-dependent friction stress (later denoted $\tau_0$), but also because of the temperature-dependence of the elasticity moduli, which affects the forest hardening. Figure 17 clearly shows a size effect in the micropillar specimens with the smallest diameter. As the micropillar diameter increases, $\tau_0^c$ measured in the micro-compression tests approaches the value measured in millimetre-scale tensile tests. For the <111> micropillar specimen orientation, the size-effect seems to have completely vanished between $\phi = 6.5\,\mu m$ and $\phi = 12\,\mu m$. However, for the <112> orientation, although $\tau_0^c$ has decreased significantly between $\phi = 3\,\mu m$ and $\phi = 12\,\mu m$, it is still higher than the value measured in the tensile tests. This suggests that the size effects depend on the crystallographic orientation. In addition, the <112> orientation has 2 available equivalent slip planes with high Schmid factors, while the <111> has 6 of them. Assuming that all slip systems are equally active for both orientations, the effective deformation rate for the <112> orientation is greater than for the <111> orientation. Due to the viscosity of the material, this can in principle lead to a harder apparent response of the <112> orientation.

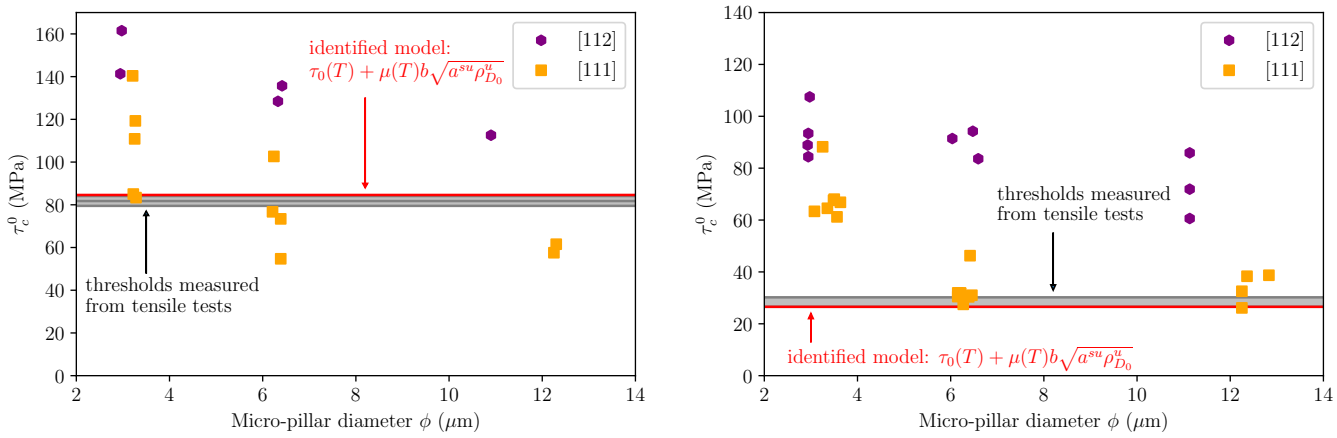


(a) 20 °C (b) 300 °C

Figure 17: Resolved shear stress at onset of plastic yielding at (a) 20 °C and (b) 300 °C as a function of micropillar diameter $\phi$. Values measured from tensile tests are shown as horizontal grey lines.

## 3. Calibration of a crystal plasticity model based on dislocation densities

In this section, a set of constitutive equations is described and calibrated in order to reproduce the experimental results that were presented in the previous section. The numerical implementation of the constitutive behaviour is available as an open-source code (Hure and Scherer, 2023) using the `MFront` generator compatible with several FEM and FFT solvers. The details of the FEM and FFT implementations can be found in Scherer and Besson (2022) and Gélébart (2020) respectively.

### *3.1. A dislocation densities-based model*

The crystal-scale constitutive equations for austenitic stainless steels for finite strains are described below. The set of equations is basically the same as that proposed in Monnet and Mai (2019), but incorporates the latest developments available in the literature regarding the interactions between dislocations. The numerical implementation is briefly described.

- ***Kinematics***

The deformation gradient $\boldsymbol{F}$ is decomposed into elastic and plastic contributions using a multiplicative split (Mandel, 1973)

$$\boldsymbol{F} = \boldsymbol{E} \cdot \boldsymbol{P} \tag{11}$$

where $\boldsymbol{E}$ and $\boldsymbol{P}$ are the elastic and plastic parts respectively. In the framework of continuum crystal plasticity, the rate of plastic deformation is governed by the rate of plastic slip on the slip planes. This is discussed in detail below.

- ***Elasticity***

Hooke's law is used to account for the cubic anisotropy of austenitic stainless steels (Ledbetter, 1984). In the finite strain framework used here, we use the elastic Green-Lagrange strain defined as

$$\boldsymbol{E}^{GL} = \frac{1}{2} \left( \boldsymbol{E}^T \cdot \boldsymbol{E} - \boldsymbol{1} \right) \tag{12}$$

The relevant stress measure associated with $\boldsymbol{E}^{GL}$ is the Piola (or second Piola-Kirchhoff) stress tensor $\boldsymbol{\Pi}^e$. This stress tensor is related to the usual Cauchy stress $\boldsymbol{\sigma}$ by $\boldsymbol{\Pi}^e = \det(\boldsymbol{E}) \boldsymbol{E}^{-1} \cdot \boldsymbol{\sigma} \cdot \boldsymbol{E}^{-T}$. Given these measures of strain

and stress, Hooke's law takes the following form

$$\boldsymbol{\Pi}^e = \mathbb{C} : \boldsymbol{E}^{GL} \tag{13}$$

- ***Plastic flow***

Austenitic stainless steel crystals have a face-centered cubic (FCC) crystal lattice. The FCC lattice has 12 main slip systems, which are composed of slip plane normals $\boldsymbol{n}$ {111} and slip directions $\boldsymbol{m}$ $<1\bar{1}0>$. Plasticity is assumed to depend solely on dislocation glide along these slip systems (Roters et al., 2011). The rate of plastic deformation is then expressed in terms of the rate of plastic slip $\dot{\gamma}^\alpha$ on each system as follows

$$\dot{\boldsymbol{P}} \cdot \boldsymbol{P}^{-1} = \sum_{\alpha=1}^{12} \dot{\gamma}^\alpha \boldsymbol{m}^\alpha \otimes \boldsymbol{n}^\alpha \tag{14}$$

$$\dot{\gamma}^\alpha = \left\langle \frac{|\tau^\alpha| - \tau_c^\alpha}{K} \right\rangle^n \text{sign}(\tau^\alpha), \quad \text{with} \quad \langle x \rangle = \begin{cases} x & \text{if } x > 0 \\ 0 & \text{if } x \leq 0 \end{cases} \tag{15}$$

where $\tau^\alpha = \boldsymbol{\Pi}^M : \boldsymbol{m}^\alpha \otimes \boldsymbol{n}^\alpha$ is the resolved shear stress on the slip system $\alpha$, where $\boldsymbol{\Pi}^M$ is the Mandel stress tensor defined as $\boldsymbol{\Pi}^M = \boldsymbol{E}^T \cdot \boldsymbol{E} \cdot \boldsymbol{\Pi}^e$. The viscoplastic Norton-like law is used to resolve the slip indeterminacy (Forest and Rubin, 2016). For $[K, n] \to [0, +\infty]$ the rate-independence is recovered.

- ***Hardening***

According to (Franciosi et al., 1980), the critical resolved shear stress (CRSS) is a function of the dimensionless dislocation densities per system $r_D^\beta = \rho_D^\beta b^2$

$$\tau_c^\alpha = \tau_0 + \mu \sqrt{\sum_{\beta=1}^{12} a^{\alpha\beta} r_D^\beta} \tag{16}$$

where $b$ is the norm of the Burgers vector, $\tau_0$ is the temperature-dependent friction stress. The shear modulus $\mu$ is computed using the Bacon-Scattergood approximation (Bacon et al., 1980; Madec and Kubin, 2017) to have the correct anisotropic energy of screw dislocations (a Poisson ratio $\nu$ is also calibrated to have the correct anisotropic energy of edge dislocations). $\mu$ is computed using the dislocation energies computed with `DisDi` (Douin, 2023). These energies are computed from the stiffness constants $C_{ij}$, the lattice parameter $a_0$ and their variation with temperature obtained in Section 2. $a^{\alpha\beta}$ is a $12 \times 12$ matrix describing the strength of the interactions between dislocations for each pair of slip planes $(\alpha, \beta)$. Note that this matrix is not symmetric (Madec and Kubin, 2017). In FCC materials, due to the crystallographic symmetry, only seven different interactions exist: the self and coplanar interactions, the Hirth lock, the Lomer junction, the collinear interaction and the 0° and 60° glissile junctions. The latter are responsible for the matrix asymmetry (the angle given refers to the character of a $\alpha$ dislocation lying at the intersection of the $\alpha$ and $\beta$ slip planes). DDD simulations have shown that the strengths of these interactions evolve with the dislocation densities (Devincre et al., 2006). Given a reference total dislocation density $\rho_{ref} = 10^{12}\text{m}^{-2}$, the interaction coefficients evolve according to the approximate form proposed by Kubin et al. (2008).

$$a^{\alpha\beta} = a_{ref}^{\alpha\beta} \left[ 0.145 + 0.855 \left( \frac{\ln\left(\sqrt{\sum_{\beta=1}^{12} a_{ref}^{\alpha\beta} r^\beta}\right)}{\ln\left(\sqrt{a_{ref}^{\alpha\beta} r_{ref}}\right)} \right) \right]^2 \tag{17}$$

Its numerical parameters are obtained by fitting this form of the deviation to DDD results (Madec and Kubin, 2017).

It should be emphasized that Eq. (16) does not account for size effects. Since the scope of this work is to capture the behaviour of large specimens, we have not used size-dependent models available in the literature at the single

crystal scale (Von Blanckenhagen et al., 2001; von Blanckenhagen et al., 2003; Xiao et al., 2015b). However, to capture the Hall-Petch effect which arises in polycrystals, the phenomenological model proposed in Haouala et al. (2020) is used to validate the model in Section 4.3.

- ***Evolution laws***

The CRSS depends on the dislocation densities (Eq. (16)) which evolve under mechanical loading. The evolution of dimensionless dislocation densities is adapted from the storage-recovery model (Kocks, 1976; Kocks and Mecking, 2003) in its generalised form (Teodosiu et al., 1993; Kubin, 2013) and is given by

$$\dot{r}_D^\alpha = \left( \frac{1}{K_{cop}} \sqrt{\sum_{\beta \in \text{coplanar}(\alpha)} a^{\alpha\beta} r_D^\beta} + \frac{1}{K_{obs}} \sqrt{\sum_{\beta \notin \text{coplanar}(\alpha)} a^{\alpha\beta} r_D^\beta} - y r_D^\alpha \right) |\dot{\gamma}^\alpha| \tag{18}$$

The first two terms correspond to dislocation trapping due to dislocation interactions between coplanar and non-coplanar slip systems, respectively. In the first case dipolar interactions induce large mean free paths, while in the second case dislocation contact reactions such as junctions are associated with short mean free paths and consequently a stronger storage rate. The last term models dislocation annihilation under the effect of screw dislocation cross-slip and $y$ is the critical distance for annihilation (here normalised by $b$). There is no direct relationship between the value of $y$ in the models and the few experimental results (where available) because the dislocation densities considered in the models include non-screw dislocations. As a consequence, $y$ is smaller in the models and may also change with loading orientation in relation to the effect of the loading on the cross-slip propensity (Kubin et al., 2009).

In (18) the material parameters are chosen independent of temperature. However, Beyerlein and Tomé (2008); Xiao et al. (2015a) have proposed extensions of the Kocks-Mecking evolution of dislocations densities accounting for the effect of temperature. This effect was neglected in our study because it would increase the number of parameters to be calibrated. Furthermore, measures of dislocations densities at different applied strains and temperatures would be required to calibrate these coefficients.

A fully implicit scheme is used to perform the numerical integration, either in the `Z-set` finite element code (Besson and Foerch, 1998) or in the `MFront` code generator (Helfer et al., 2015). Both implementations give the same results and are not distinguished in the following. Details of the numerical implementation can be found in Hure et al. (2016).

### *3.2. Calibration of the model*

The constitutive equations described in Section 3.1 involve a large number of parameters. The elastic moduli (Eq. 13) are taken from the results obtained in Section 2 (Eqs. 8). The Norton parameters involved in the viscoplastic flow rule (Eq. 15) are set to $K = 1$ and $n = 15$, resulting in a limited rate-dependent behaviour for the simulations reported below. The following procedure is used to determine the thermal part of the critical resolved shear stress $\tau_0$. Feaugas and Haddou (2003) investigated the effect of grain size on the tensile behaviour of AISI 316L stainless steel at room temperature. All the materials presented in their paper had initial dislocation densities below $10^{10}$ m$^{-2}$. The forest dislocation hardening term is of the order of 0.5 MPa or less and can therefore be neglected in Eq. 16 in order to evaluate $\tau_0$. From their data (see Figure 3.(b) in Feaugas and Haddou (2003)), we can extrapolate the yield stress at infinite grain size $\sigma_0^\infty$ as the vertical intercept of the curve corresponding to $5 \times 10^{-3}$ total deformation. We find $\sigma_0^\infty(293\text{K}) = 117.28$ MPa, which gives us $\tau_0(293\text{K}) = \sigma_0^\infty(293\text{K})/M = 38.33$ MPa, where $M = 3.06$ is the Taylor factor for FCC materials. Pawel et al. (1996) studied the temperature dependence of the yield stress of 316 stainless steels. From their data (see Figure 1 in Pawel et al. (1996)), we approximate the temperature dependence with the following linear fit: $\sigma_0(T) = -0.2345T + 361.80$ (in MPa and T in K). We then assume, to a first approximation, that the parameter $k$ is constant with the temperature in the Hall-Petch relation: $\sigma_0(T) = \sigma_0^\infty(T) + k/\sqrt{d}$ where $d$ is the grain size. We can then conclude that $\sigma_0$ and $\sigma_0^\infty$ have the same

Table 3: Model parameters and retained ranges of variation. Ranges of variation are selected based on values and hierarchies commonly used in the literature (Devincre et al., 2006; Kubin et al., 2008; Madec and Kubin, 2017; Monnet and Mai, 2019).

| Parameter | $K_{obs}$ | $K_{cop}$ | $y$ | $a_{ref}^{self}$ | $a_{ref}^{coplanar}$ | $a_{ref}^{Hirth}$ | $a_{ref}^{Lomer}$ | $a_{ref}^{collinear}$ | $a_{ref}^{glissile\ 0°}$ | $a_{ref}^{glissile\ 60°}$ |
|---|---|---|---|---|---|---|---|---|---|---|
| Min. Value | 4 | 50 | 1 | 0.06 | 0.01 | 0.01 | 0.12 | 0.5 | 0.09 | 0.06 |
| Max. Value | 25 | 200 | 10 | 0.16 | 0.12 | 0.06 | 0.25 | 1.0 | 0.16 | 0.12 |

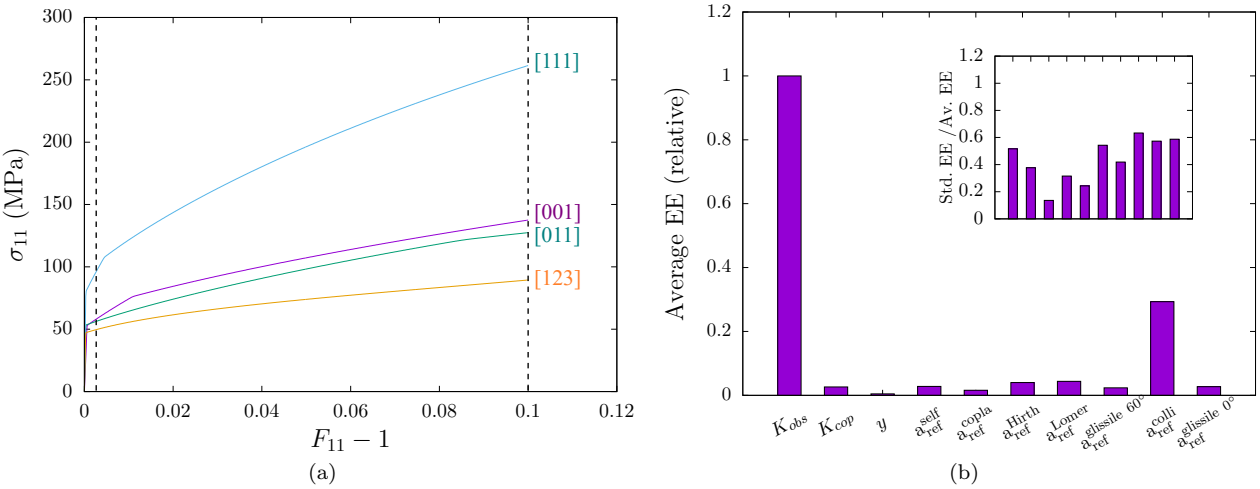


Figure 18: (a) Numerical tensile curves predicted by the model using the mean value of the parameters from Tab. 3 (b) Results of the Morris screening analysis for [001] load axis at 0.2%, using $p = 10$ intervals to discretise the range of variations in the parameters and $r = 10$ trajectories (URANIE, 2020).

linear dependence on temperature and we find: $\sigma_0^\infty(T) = -0.2345(T - 293.15) + 117.28$ (in MPa and T in K). The thermal part of the critical resolved shear stress is therefore $\tau_0(T) = \sigma_0^\infty(T)/M = -0.07662(T - 293.15) + 38.33$ (in MPa and T in K). The magnitude of the Burgers vector is $b = 0.254$ nm. Tab. 3 shows the remaining parameters to be set as well as the variations considered here in the light of the values and ranges reported in the literature.

The influence of these parameters on the tensile curves, and in particular on the hardening modulus, differs depending on the loading axis as a consequence of Eq. (18). For the [001] (resp. [111]) axis, 8 (resp. 6) slip systems are expected to be activated according to Schmid's law, leading to a strong hardening in particular due to collinear interactions. Therefore, $K_{obs}$ and $a_{ref}^{collinear}$ are expected to have a dominant effect on the tensile curves. For the [011] (respectively [123]) axis, 4 (respectively 1) slip systems are activated and the self-interaction coefficient $a_{ref}^{self}$ is expected to play a key role in the hardening modulus. In all cases, the parameter $y$ is expected to have an influence only for large dislocation densities, *e.g.* for large strains.

In order to gain more quantitative insights, a sensitivity analysis is performed to evaluate the parameters that influence the tensile curves. From this analysis we identify which parameters can be calibrated with the available experimental results. For each crystallographic orientation from the experimental database, *i.e.* [001], [011], [111], [123], material point numerical simulations are performed under tensile loading up to 10% strain, for $T = 300°C$ and an initial total dislocation density $\rho_0^{tot} = 10^{12}\text{m}^{-2}$. Fig. 18 shows the numerical tensile curves predicted by the model using the mean value of the parameters from Tab. 3. The hardening modulus at 0.2% and 10% strain (corresponding to the dotted lines in Fig. 18) are chosen as the output of these simulations for the sensitivity analysis.

Note that for the [001] and [111] orientations, slope breaks are observed due to the deactivation of half of the slip systems. For the [111] orientation, due to the strong collinear interaction, for each pair of slip systems sharing the same Burgers vector, only one slip system remains active after the break in the hardening slope. This phenomenon, which has already been reported in the literature, is a numerical instability that can be triggered depending on various parameters such as the method used for the numerical integration and / or the values of

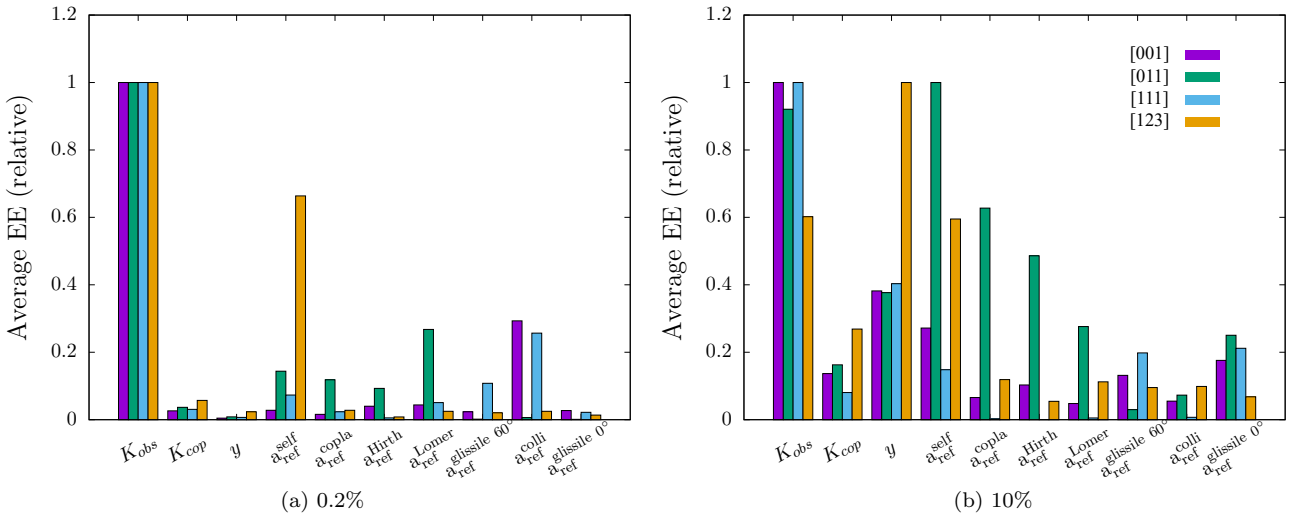


(a) 0.2% (b) 10%

Figure 19: Results of the Morris screening analysis for the different crystallographic orientations, using $p = 10$ intervals to discretise the range of variations of the parameters and $r = 10$ trajectories (URANIE, 2020), for (a) 0.2% and (b) 10% strain.

the viscosity parameters. The Morris method (Morris, 1991) is used to evluate the sensitivity of these hardening moduli to the parameters shown in Tab. 3. This method is based on the calculation of elementary effects, hereafter referred to as EE, which correspond to the first order derivative, when only one factor is varied at a time. The elementary effects are computed at different locations of the hyperspace defined by the parameters. Finally, for each parameter, the mean of the elementary effects and the corresponding standard deviation are computed.

This method allows parameters to be ranked in terms of their influence on the results. More details about this method can be found in Saltelli et al. (2004). In practice, the `URANIE` platform (Blanchard et al., 2019) is used to perform the Morris screening analysis. Roughly speaking, three different cases can be found (URANIE, 2020). High mean / low standard deviation corresponds to a parameter that has an influence on the result regardless of the values of the other parameters, while a high standard deviation indicates interactions with other parameters. Low average corresponds to parameters having little influence. A typical output is shown in Fig. 18b, which shows that the standard deviations are similar for all parameters, *i.e.*, all parameters interact with each other. Therefore, only the mean values of the elementary effects are reported below. The results are shown in Fig. 19 for each crystallographic orientation of the experimental database. At low strain (Fig. 19a), for all loading directions, $K_{obs}$ is the main parameter influencing the hardening slope. Regarding the interaction coefficients, $a_{ref}^{collinear}$ dominates for [001] and [111] directions, while $a_{ref}^{Lomer}$ (respectively $a_{ref}^{self}$) dominates for [011] (respectively [123]). In essence, for each orientation and its corresponding set of active dislocation interactions, the dominant coefficient of the interaction matrix in the Morris analysis corresponds to the coefficient with the largest value (*i.e.* strongest interaction). At higher strains (Fig. 19b), the picture is different as self and weaker interaction coefficients have a strong influence on the hardening slope (as a result for the [001] and [111] directions of the deactivation of half the slip systems). The annihilation distance $y$ also plays an important role.

Based on the available experimental database, the sensitivity analysis leads to the conclusion that $K_{obs}$, $a_{ref}^{self}$, $a_{ref}^{copl}$ and $y$ may be calibrated effectively due to their important global effect ($K_{obs}$, $a_{ref}^{self}$ and $y$) or major effect along a specific orientation ($a_{ref}^{copl}$). These four parameters have been calibrated using material point simulations under tensile loading. For the other coefficients related to dislocation reactions (junctions and collinear interaction/annihilation), DDD results are available for several FCC metals in Madec and Kubin (2017) as a function of their Poisson coefficient. Values for 316L are obtained by interpolation of these results.

The value of $K_{cop}$ is not well known from the literature, but since its effect in the Morris analysis is rather weak, it was decided not to calibrate it with our experimental data. The values of $K_{cop}$ reported in the literature vary in the range [26;180] (Kubin et al., 2008; Monnet and Mai, 2019). Furthermore, $K_{obs}$, $K_{cop}$ and $y$ can in principle be considered as functions of the orientation (Kubin et al., 2008). Different values of these parameters

Table 4: Parameters of the constitutive equations for 316L austenitic stainless steel. Calibrated parameters are highlighted in red.

| $C_{11}$ (MPa) | $C_{12}$ (MPa) | $C_{44}$ (MPa) | $\mu$ (MPa) | |
|---|---|---|---|---|
| 233360 - 51.3$T$(K) | 152880 - 27.7$T$(K) | 134430 - 30.8$T$(K) | $0.02478T(K)^2 - 56.01T(K) + 86070$ | |
| $\tau_0$ (MPa) | $K$ (MPa) | $n$ (-) | $\rho^{\beta}_{D_0}$ (m$^{-2}$) at 20 °C | $\rho^{\beta}_{D_0}$ (m$^{-2}$) at 300 °C |
| $-0.07662T(K) + 60.79$ | 1 | 15 | $3.817 \times 10^{12}$ | $2.224 \times 10^{11}$ |
| $K_{cop}$ (-) | $K_{obs}$ (-) | $y$ (-) | $a^{\text{self}}_{\text{ref}}$ (-) | $a^{\text{coplanar}}_{\text{ref}}$ (-) |
| 100 | 3.74 | 6.68 | 0.0534 | 0.0438 |
| $a^{\text{Hirth}}_{\text{ref}}$ (-) | $a^{\text{Lomer}}_{\text{ref}}$ (-) | $a^{\text{collinear}}_{\text{ref}}$ (-) | $a^{\text{glissile 0°}}_{\text{ref}}$ (-) | $a^{\text{glissile 60°}}_{\text{ref}}$ (-) |
| 0.0484 | 0.1722 | 0.6972 | 0.1156 | 0.0885 |

could have been sought for each orientation. However, for the sake of simplicity and future applicability of the model to complex load paths in polycrystal simulations, the same value of the these parameters is used for each orientation.

In addition, the initial dislocation densities are unknown. Therefore, $\rho^{\beta}_{D_0}$ is also calibrated within the procedure. As different batches of material are used in the tests at 20 °C carried out by Karaman et al. (2001) and the tests done at 300 °C in this study, a different value of $\rho^{\beta}_{D_0}$ is calibrated for each temperature. An objective function measuring the distance between the experimental tensile curves at 20 °C and 300 °C and the simulated curves was minimised until convergence. The set of material parameter values is given in Tab. 4. The coefficients calibrated by the optimisation procedure are highlighted in red. The initial dislocation densities calibrated to fit the yield stress are consistent with a single crystal material that has been allowed to cool down slowly. The obstacle mean free path coefficient $K_{obs}$ takes a value close but lower than the typical values reported in the literature which are typically in the range [4;12] (Kubin et al., 2008; Monnet and Mai, 2019). The value of $y$ found in the calibration is close to the value of 3.9 used by Monnet and Mai (2019)[2]. The self-interaction coefficient $a^{self}_{ref}$ is not well known in the literature and cannot be accurately estimated by DDD (Kubin et al., 2008). The values typically used for $a^{self}_{ref}$ are close to 0.122 (Devincre et al., 2007; Kubin et al., 2008; Monnet and Mai, 2019). Our calibration suggests that the strength of the self-interaction is more than twice lower than what is typically considered. Kubin et al. (2008) discussed how coplanar and self-interactions share the formation of small collinear density via screw dislocation cross-slip and thus justified using the same coefficient for both types of interactions. Interestingly, our calibration resulted in similar values of $a^{self}_{ref}$ and $a^{coplanar}_{ref}$, consistent with the hypothesis of interactions of similar strength, but both took values lower than those typically used in the literature. The following ranking results from our identification of self and coplanar interaction coefficients: $a^{\text{coplanar}}_{\text{ref}} < a^{\text{Hirth}}_{\text{ref}} < a^{\text{self}}_{\text{ref}} < a^{\text{glissile 60°}}_{\text{ref}} < a^{\text{glissile 0°}}_{\text{ref}} < a^{\text{Lomer}}_{\text{ref}} < a^{\text{collinear}}_{\text{ref}}$.

## 4. Numerical experiments on single- and polycrystal specimens

### *4.1. Single crystal specimens in tension*

The material parameters were calibrated using material point simulations as described in the previous section. The calibrated model is then used to simulate the real geometry of the specimen used in tensile tests at 300 °C. The numerical simulations are based on the finite element mesh shown in Figure 20. Only the central part of the specimen, corresponding to the DIC region, is modelled. The displacement boundary conditions used in the simulations are extracted from the DIC measurements. As the material contains many small inclusions of ferrite,

[2]Note that Monnet and Mai (2019) use a non-normalised version of the model with an annihilation distance $y = 1$ nm. After normalisation by the norm of the Burgers vector $b = 2.54 \times 10^{-10}$ nm, we find a nondimensional annihilation distance $y = 3.9$.

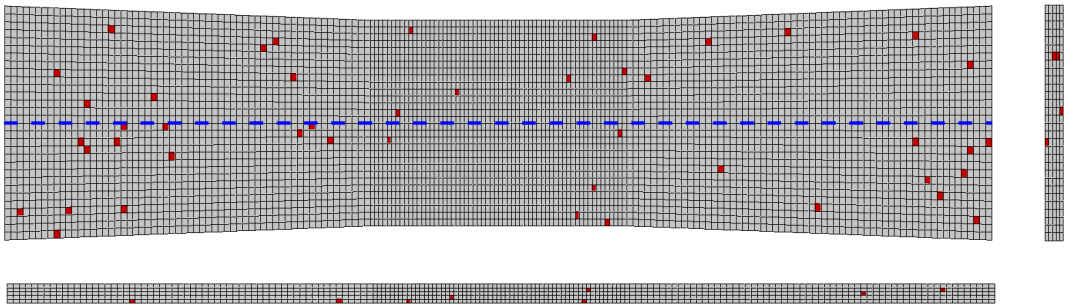

Figure 20: Finite element mesh of the single crystal tensile specimen consisting of 27000 quadratic hexahedral elements with reduced integration using 8 Gauss points. Randomly distributed stiff elastic inclusions representing %1 of the total volume are highlighted in red. The dashed blue line represents the central axis of the specimen along which the strain profiles are plotted in Fig. 24.

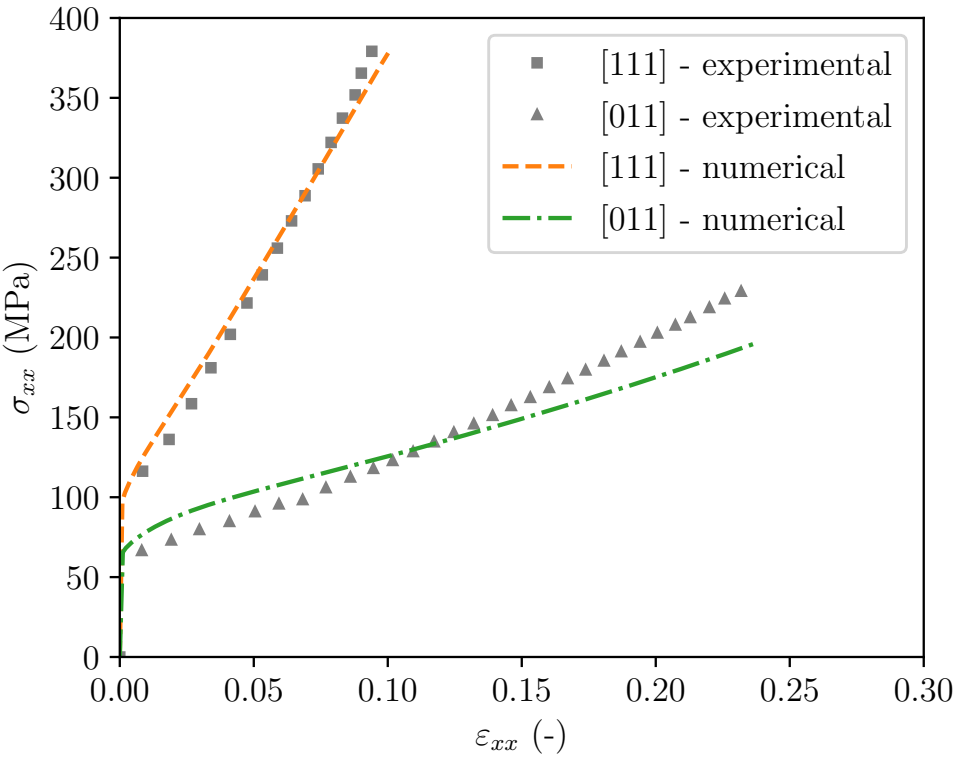


Figure 21: Experimental and numerical true stress *vs* true strain tensile curves at 300 °C.

we introduce a secondary phase of inclusions representing 1% of the specimen volume. Abe and Watanabe (2008) showed that the hardness of the ferrite phase is between 1 and 2 times greater than that of the austenite at 335 °C. In a first approximation the inclusions are therefore considered to be purely elastic with identical crystallographic orientation and elasticity parameters as the single crystal phase. They are randomly distributed as individual finite elements throughout the finite element mesh and are shown in red in Figure 20.

Figure 21 shows the comparison of experimental and numerical true stress-strain curves at 300 °C. Yield stresses and hardening slopes are well captured by the numerical model. The yield stress of the <011> orientation is slightly overestimated and the hardening slope is slightly underestimated in the simulation. Despite the fact that the calibration of the model was carried out with material point simulations – and thus did not take the geometry into account – the agreement between experimental results and numerical simulations on the true specimen geometry is satisfactory.

The in-plane Green-Lagrange strain components post-processed from the numerical simulations are shown in Figures 22 and 23. These fields are the numerical twins of the experimental strain fields post-processed from DIC measurements shown in Figure 7 and 8. In Figure 22, the strain fields are very heterogeneous. Bands of intense

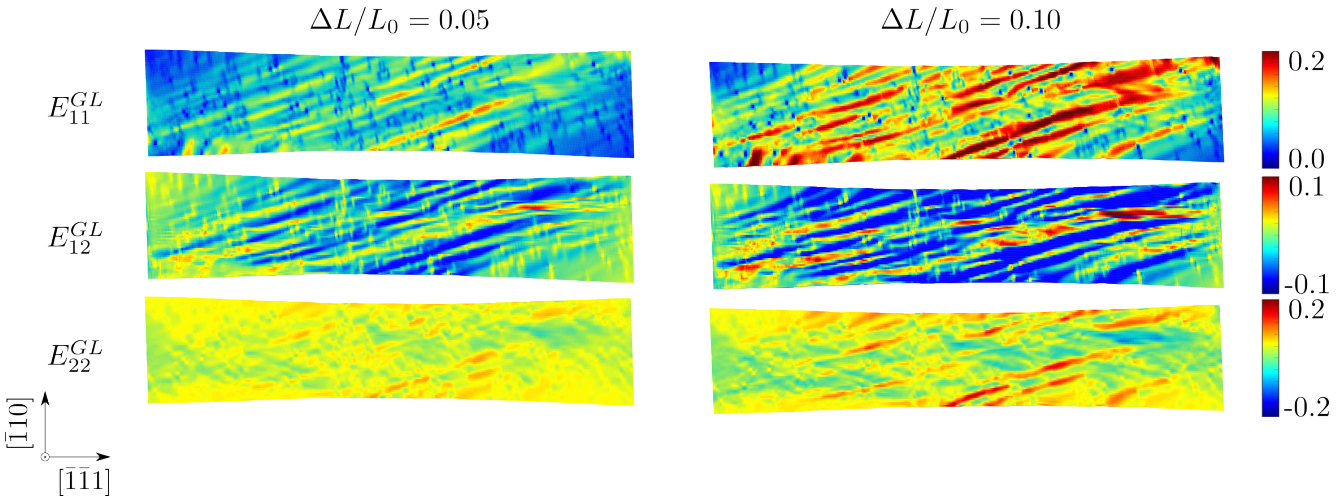


Figure 22: In-plane Green-Lagrange strain fields post-processed from finite element simulations for the <111> specimen at macroscopic strains $\Delta L/L_0 = 0.05$ and 0.10.

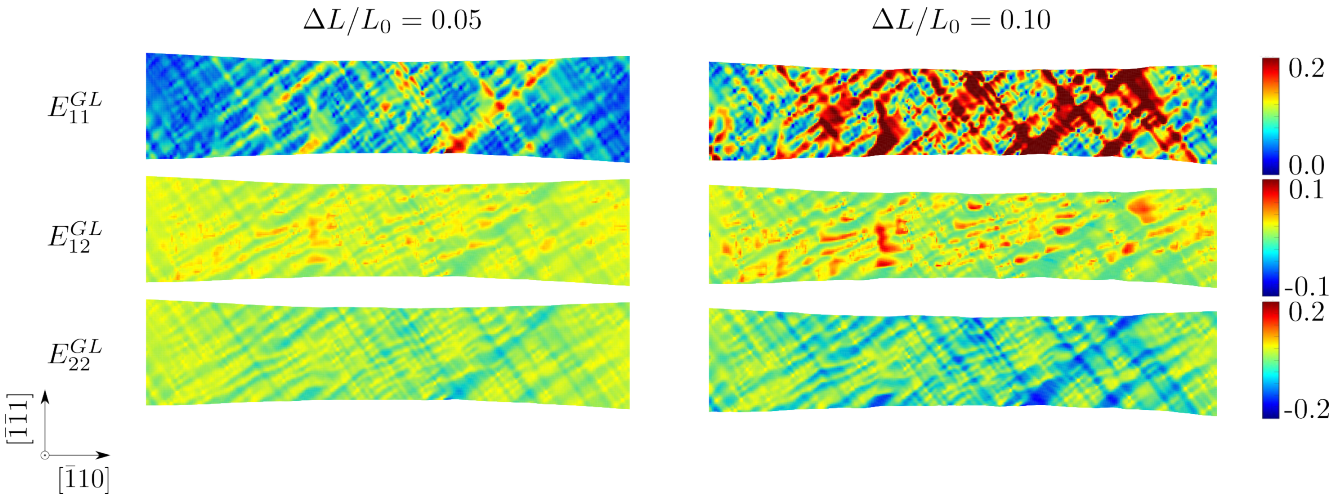


Figure 23: In-plane Green-Lagrange strain fields post-processed from finite element simulations for the <011> specimen at macroscopic strains $\Delta L/L_0 = 0.05$ and 0.10.

plastic strain are formed in the central part of the specimen. At $\Delta L/L_0 = 0.05$, unlike the experimental field in Figure 7, which showed two types of bands, only a single type of band is observed here. However, at $\Delta L/L_0 = 0.10$, a second type of band appears in the $E_{12}^{GL}$ field. The magnitude of the deformation within the bands, as well as the band spacing and orientation, are analogous in the numerical and experimental fields. In Figure 23, bands of intense plastic slip are also observed. The nature of the bands observed in the simulation is in very good agreement with the DIC results in Figure 8. The numerical counterparts of the plastic slip fields shown in Figure 9b and 10b are plotted in Figure C.32 in Appendix C. Overall, a satisfactory agreement between experimental and numerical plastic slip fields is observed.

In Figure 24 we compare the experimental and numerical profiles of the horizontal Green-Lagrange tensile strain along the horizontal central axis of the specimen. The profiles are plotted at the macroscopic strain $\Delta L/L_0 = 0.05$. In Figures 24a and 24c we can see that the local strain is very heterogeneous in both cases. The amplitude of the oscillations around the mean value is comparable between the experiments and the simulations. In order to compare the frequencies of oscillations, we compute the fast Fourier transforms of the different profiles. Figures 24b and 24d show the FFT amplitudes (or weights) associated with the corresponding frequencies. A good agreement between the experimental and numerical distribution of the FFT amplitudes is obtained for both crystallographic orientations.

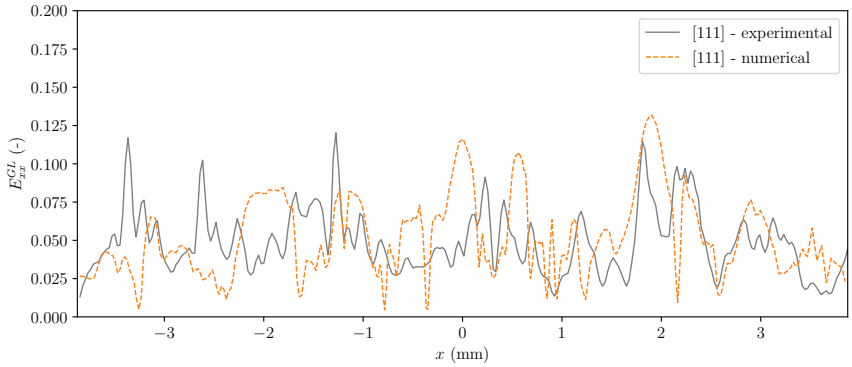


(a) <111> Green-Lagrange strain profile

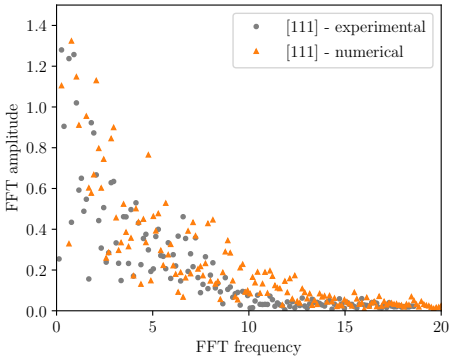


(b) <111> FFT weights

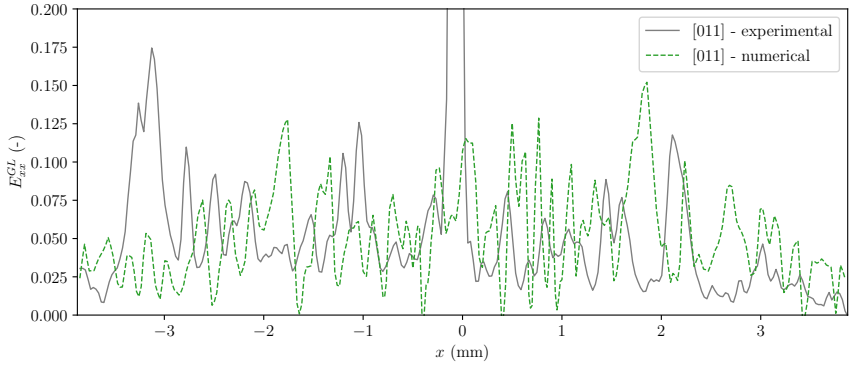


(c) <011> Green-Lagrange strain profile

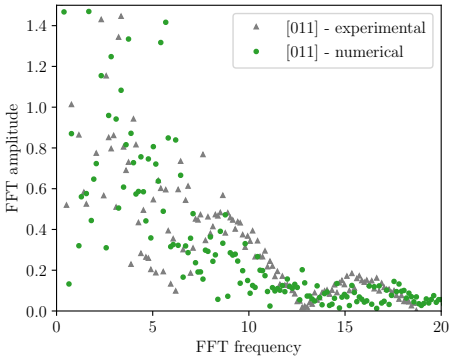


(d) <011> FFT weights

Figure 24: Experimental vs numerical Green-Lagrange strain $E_{xx}^{GL}$ along the horizontal central axis of the specimen for the (a) <111> and (c) <011> specimens at $\Delta L/L_0 = 0.05$. Fast Fourier transforms (FFT) weights computed from the profiles are shown in (b) and (d).

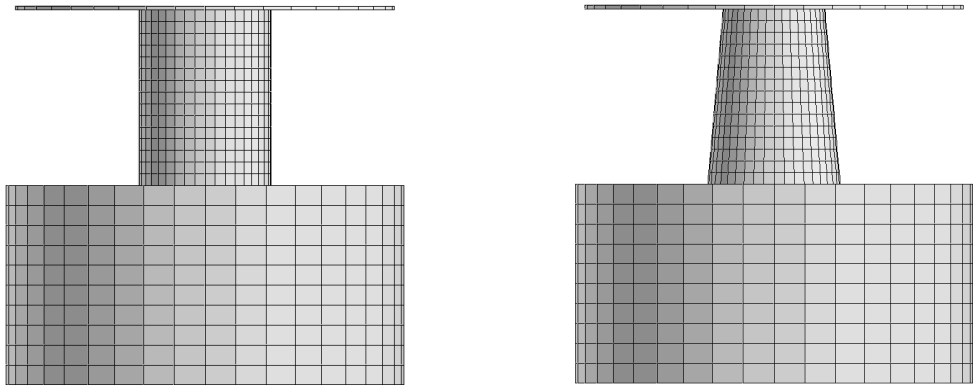

(a) $\alpha = 0°$ (b) $\alpha = 5°$

Figure 25: Finite element meshes of micropillar specimens with taper angles $\alpha$ equal to (a) 0° and (b) 5°.

### *4.2. Single crystal specimens in micro-compression*

The compression experiments at 300 °C on micropillar specimens presented in Section 2.4 are simulated with the calibrated model in order to test its predictive capability for a more complex experiment. There is some variability in the experimental results due to the slight differences in specimen geometry introduced by the FIB machining technique. In addition, the simulation of these experiments is subject to some uncertainties in measuring the exact shape of the specimens. For simplicity, we simulate the compression experiments on two different micropillar geometries with taper angles $\alpha = 0°$ and 5°. As the crystal plasticity model does not include size effects, the size of the micropillar geometry does not play a role in the numerical predictions. The 3D finite element meshes of the corresponding geometries are shown in Figure 25. Each mesh consists of 3741 quadratic hexahedral elements with reduced integration using 8 Gauss points. A Coulomb contact behaviour with a friction coefficient of 0.1 is used to model the interaction between the indenter and the specimen. The indenter axis is assumed to be perfectly aligned with the specimen axis. A constant speed of $50\,\mu m\,s^{-1}$ is applied to the indenter, while the underside of the specimen is clamped. The radius of the base is taken sufficiently large to avoid any influence on the behaviour of the micropillar specimen. Since we are trying to predict the size-independent behaviour of the single crystal, we will compare our predictions with the experimental results obtained on micropillars with the largest diameter ($\sim 12\,\mu m$).

Figure 26 shows the comparison between the experimental results and the numerical simulations. The following procedure is used to construct the mean and standard deviation of the experimental and numerical results. First, a linear interpolation operator is used in order to resample the experimental (respectively numerical) results to equally spaced displacement intervals. Then, for each displacement interval, the mean value and standard deviation of the experimental (respectively numerical) load applied is computed. Finally, the solid lines correspond to the collection of mean loads computed at each displacement interval, while the padding regions are bounded by the collection of mean loads plus or minus twice the collection of standard deviations.

Note that the experimentally measured displacements include the unknown compliance of both the indenter and the entire crosshead. Therefore, the measured displacements have been corrected in order to match the elastic slope predicted by the numerical simulations.

For the <112> orientation, comparing the means, the apparent yield point predicted by the numerical simulation is about 20% lower than the experimentally measured value. This can be partly explained by residual size effects, even for micropillar specimens of 12 µm diameter. In addition, the numerical simulation with a taper angle of $\alpha = 0.0°$ shows a closer agreement with the experimental yield point. The numerical predictions beyond the yield point are characterised by a slightly non-linear hardening behaviour with an inflection point at about 11% strain.

For the <111> orientation, the numerically predicted yield point agrees very well with the experimental value. For the first 1% strain after yielding, the experimental curve shows a convex strain hardening which is not ob-

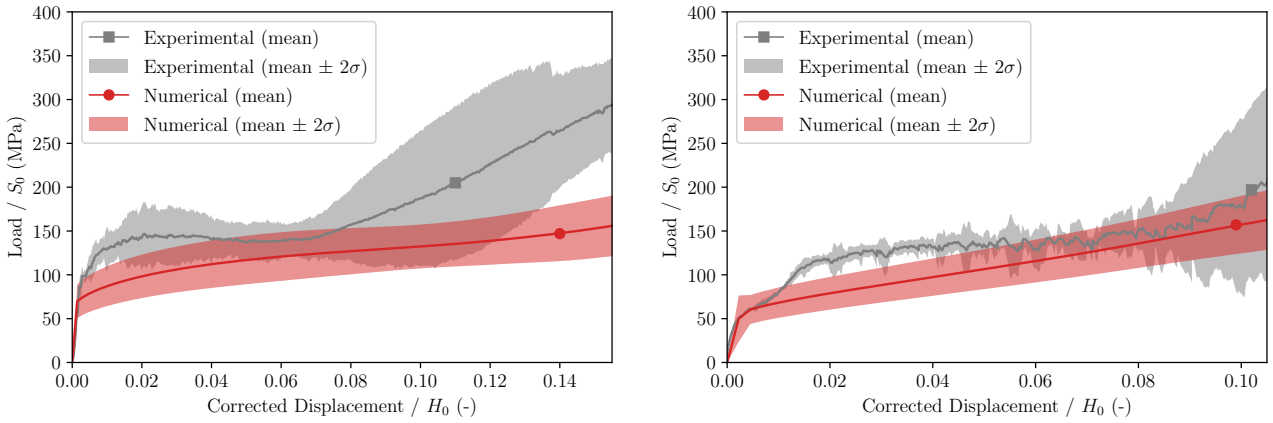


(a) <112>




(b) <111>

Figure 26: Comparison of numerical and experimental stress-strain curves for (a) <112> and (b) <111> micropillar specimens in compression. The solid lines correspond to the mean of several realisations while the shaded areas represent the $2\sigma$ deviation from the mean value observed in the data.

served numerically. However, the almost linear hardening rate predicted numerically agrees well with the concave hardening rate measured experimentally for the remaining part of the curve.

The steep increase in stress (referred to as phase 3 in Section 2.4) measured at about 7% strain for the <112> orientation and 9% strain for the <111> orientation is not observed in the numerical simulations. Although the simulations for the <112> show an inflection point at about 11% strain, the predicted hardening rate after the inflection remains twice lower than the experimental measurement.

Figure 27 shows the plastic slip field at a macroscopic strain of 5%. The Figure 27a corresponds to a taper angle of $\alpha = 0°$ while Figure 27b corresponds to $\alpha = 5°$. The figures show the plastic slip for the slip system $(\bar{1}11)[\bar{1}0\bar{1}]$ (indexed as #7 in 9d) which corresponds to the active slip system shown in Figure 16 and Supplementary Videos 1 and 2. The range of plastic slip is quite similar between both taper angles. However, the slip distribution inside the micropillar is very different. When the taper angle is large, the cross section at the top of the pillar is reduced, therefore plastic slip remains localised in this region. For $\alpha = 0°$, there are two orthogonal bands of intense plastic. Note that the field of view in Figure 27 is the same as the one in Figure 16. One band is a slip band, *i.e.* a band parallel to the slip direction. The other is a kink band, *i.e.* a band perpendicular to the slip direction. Kink bands are associated with large lattice rotations. The slip band is clearly visible in the experiments, but the kink band is not. This could be a possible explanation for the strong apparent hardening in Figure 26a. The curvature of the crystal lattice is indeed related to the density of geometrically necessary dislocations (GND). There is therefore an energetic cost associated with the formation of a kink band, which in turn can be translated into an apparent hardening. The model used in this study neglects the effect of GND, so both slip and kink bands are possible.

### *4.3. Polycrystal specimens in tension*

The calibrated constitutive equations have been shown to give quantitative predictions with respect to experimental results as a function of temperature, crystallographic orientation and loading conditions. Up-scaling is considered in this section by looking at the behaviour of polycrystalline aggregates through homogenisation (Fig. 28a). It is well known that the use of crystal plasticity constitutive equations calibrated at the single crystal scale to perform homogenisation - either analytically or numerically - does not lead to results in quantitative agreement with experiments. The main reason for this discrepancy is the effect of grain boundaries leading to the Hall-Petch effect. Increasing the value of $\tau_0$ (Han, 2012) or adding a grain size dependent term to the CRSS (Monnet and Mai, 2019) allows to recover numerical predictions in agreement with experimental data. However, this modelling implies a rather diffuse effect of grain boundaries within the polycrystalline aggregate, which may not be relevant for some applications, *i.e.*, regarding the prediction of stress-strain fields close to grain boundaries.

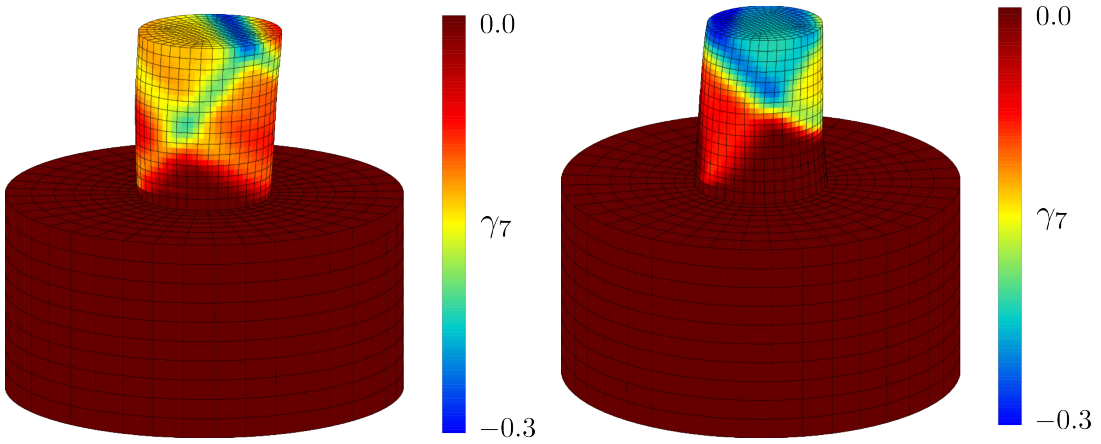


(a) $\alpha = 0°$ (b) $\alpha = 5°$

Figure 27: Comparison of numerical plastic slip fields for <112> micropillar specimens in compression with taper angles (a) $\alpha = 0°$ and (b) $\alpha = 5°$. Only the plastic slip field corresponding to the slip system activated in the experiment is shown. It also corresponds to the dominant slip system in the simulations. The fields are plotted for a macroscopic strain of 5%.

A simple model has recently been proposed based on the consideration of an additional term for the multiplication of dislocations near grain boundaries (Haouala et al., 2020) as follows

$$\dot{r}_D^\alpha = \left( \max \left[ \frac{1}{K_{cop}} \sqrt{\sum_{\beta \in \text{coplanar}(\alpha)} a^{\alpha\beta} r_D^\beta} + \frac{1}{K_{obs}} \sqrt{\sum_{\beta \notin \text{coplanar}(\alpha)} a^{\alpha\beta} r_D^\beta} \; , \; \frac{K_s^\alpha}{\bar{d}_{gb}^\alpha} \right] - y r_D^\alpha \right) |\dot{\gamma}^\alpha| \tag{19}$$

where $\bar{d}_{gb}^\alpha = d_{gb}^\alpha / b$ is the dimensionless distance to the grain boundary along the slip direction $\alpha$, and $K_s^\alpha$ is a dimensionless modulus of dislocation storage. The value of $K_s^\alpha$ depends on the possibility of slip transmission, *e.g.*, by considering the Luster-Morris criterion as in (Haouala et al., 2020). Close to grain boundaries, Eq. (19) leads to a strong hardening, while far from grain boundaries Eq. (18) is recovered. This modelling, though simple, allows to recover the Hall-Petch effect (Nieto-Valeiras et al., 2022). However, to calibrate $K_s^\alpha$, it requires experimental evidences regarding slip transmissions at grain boundaries. As these data are lacking for austenitic stainless steels, a simpler model is considered here where $K_s^\alpha = K_s$ is constant, *i.e.* no slip transmission at all grain boundaries. In addition, another simplification is made, mostly for practical purposes, that the distance $d_{gb}^\alpha$ is taken as the minimum distance to the nearest grain boundary (Fig. 28b). Finally, the value of the parameter $K_s$ needs finally to be calibrated, which is done below.

The `Neper` software (Quey et al., 2011) is used to generate a fully periodic polycrystalline aggregate containing $n_g = 100$ grains by a Voronoi tesselation of a unit cube (Fig. 28a). Random crystallographic orientations are assigned to the different grains. The aggregate is discretised into 50 x 50 x 50 voxels. For each voxel the distance to the nearest grain boundary is computed and normalised by the average grain size $\phi$ computed as $\phi = n_g^{-1/3}$ (Fig. 28b): $d_{gb}^\phi = d_{gb}/\phi$. Thus, the additional term introduced in Eq. (19) can be written as follows

$$\frac{K_s}{\bar{d}_{gb}} = \frac{bK_s}{d_{gb}^\phi \phi} = \frac{K_s'}{d_{gb}^\phi} \Rightarrow K_s' = \frac{bK_s}{\phi} \tag{20}$$

In the following, values of $K_s'$ are considered in the range $[10^{-6} : 10^{-4}]$, corresponding to grain sizes between $10\mu$m - the typical grain size in 304 / 316 austenitic stainless steels - and 1mm - single crystal specimens tested in this study - for the typical value of $K_s \sim 5$ (Haouala et al., 2020) reported in the literature.

Numerical simulations are performed using `AMITEX_FFTP` FFT-based solver (Gélébart, 2023). The aggregate shown on Fig. 28a is used together with the calibrated constitutive equations described in Section 3.2 for three different values of the initial total dislocation density $\rho_0^{tot} = [1; 10; 33]\, 10^{12}\text{m}^{-2}$ and a temperature of $T = 573$K. A volume-average uniaxial tensile load is applied to the unit-cell. Stress-strain curves are computed up to 1%

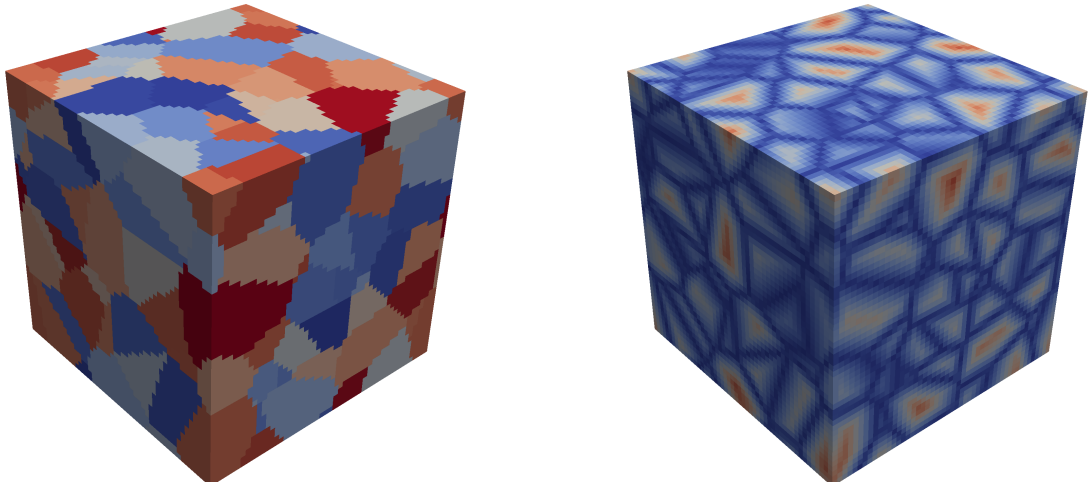

(a) (b)

Figure 28: (a) Periodic Voronoi-based polycrystalline aggregate with 100 grains. (b) Minimum distance to the nearest grain boundary.

strain for different values of $K_s' \in [10^{-6} : 10^{-4}]$. The results are shown on Fig. 29a for $\rho_0^{tot} = 10^{12}\text{m}^{-2}$. Increasing the value of the parameter $K_s'$ leads to a strong hardening at low strain values, consistent with the increase in dislocation densities near grain boundaries modelled in Eq. (19). Additional simulations (not shown here) with finer discretisation lead to the same quantitative results. The conventional yield stress (YS) - for an offset plastic strain of 0.2% - is extracted and plotted in Fig. 29b for different values of $K_s'$ and $\rho_0^{tot}$. For low initial dislocation density, a Hall-Petch effect is obtained, with the yield stress depending on the inverse of the square root of the grain size. For higher initial dislocation density, the Hall-Petch law is recovered only for small grain size. This effect was expected: in the limit of very high initial dislocation density, the modelling of grain boundary effect - based on the multiplication of dislocations - would not be effective. The final step is to check whether such an approach can quantitatively reproduce the stress-strain curves of 300 series polycrystalline austenitic stainless steels. Fig. 30 shows the comparison between the tensile curves obtained at 25°C and 340°C for a 304L austenitic stainless steel with a grain size of 21$\mu$m and an initial dislocation density of $10^{13}\text{m}^{-2}$ (Paccou, 2019; Azihari, 2023) to the numerical simulations of polycrystalline aggregates with the calibrated constitutive equations using $K_s = 3.3$. A good agreement is obtained for both temperatures, except for low strain values where the model underestimates the stress. Interestingly, the value of $K_s$ is close to that used in Haouala et al. (2020); Nieto-Valeiras et al. (2022) and predicted by 3D dislocation dynamics simulations. A linear fit of the linear part of the curves in Figure 29b provides an estimate of the Hall-Petch parameter $K$ which relates the yield stress to the grain size as follows $YS = K/\sqrt{\phi}$. With $K_s = 3.3$ we obtain $K = 0.17\,\text{MPa}.\sqrt{\text{m}}$ which is in the range [0.11;0.19] of the experimental values and agrees remarkably well with the DDD predicted value of $0.16\,\text{MPa}.\sqrt{\text{m}}$ reported by Jiang et al. (2019). Remembering that the term related to $K_s$ in Eq. (19) has no effect on single crystals, the set of constitutive equations proposed in this study allows to predict the mechanical behaviour of austenitic stainless steels for single crystal and polycrystalline samples as a function of temperature.

## 5. Discussion

This section discusses potential improvements and future research avenues for the modelling of the mechanical behaviour of austenitic stainless steel single crystals.

- **Experimental**
  Dislocation-based constitutive equations for single crystals use the dislocation densities in each slip system as state variables. Thus, the initial dislocation density is a parameter of the model, which is then expected

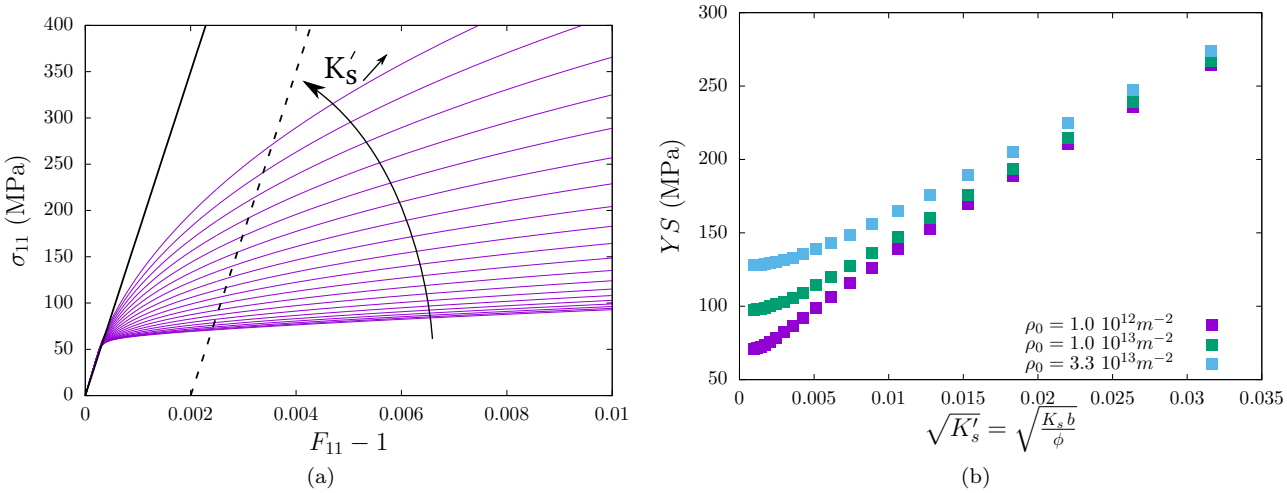


Figure 29: (a) Polycrystalline aggregate stress-strain curves under tensile loading at 300°C for $\rho_0^{tot} = 10^{12}\text{m}^{-2}$, for different values of $K_s' \in [10^{-6} : 10^{-4}]$. (b) Yield stress (for an offset strain of 0.2%) as a function of $K_s'$ for different initial values of dislocation density.

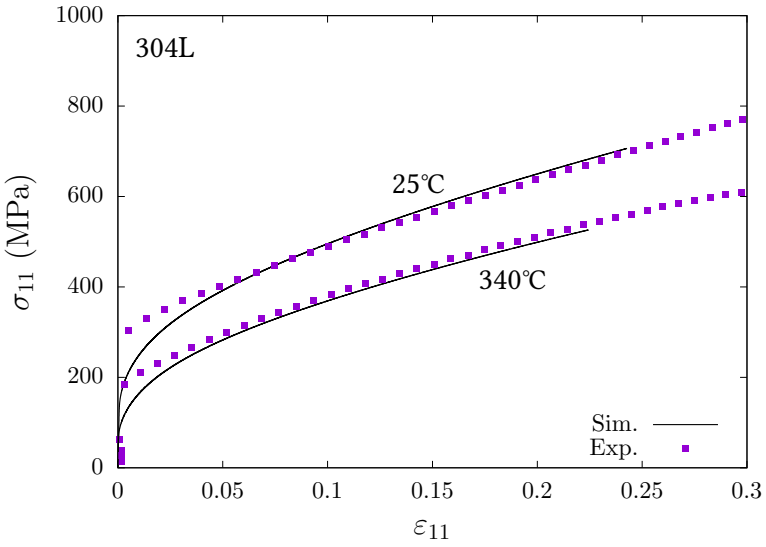


Figure 30: Comparison between experimental tensile curves on a 304L material ($\phi = 21\mu$m and $\rho_0^{tot} = 10^{13}\text{m}^{-2}$) and numerical predictions obtained on polycrystalline aggregates, using $K_s = 3.3$.

to accurately predict the evolution as a function of strain. In this study, the initial dislocation density - assumed to be the same in all slip systems - has been obtained indirectly to recover the experimentally measured initial resolved shear stresses due to the lack of experimental measurements at the initial state. More importantly, the accuracy of the dislocation density evolution with strain needs to be assessed. Both destructive - TEM observations (Pesicka et al., 2003) - and non-destructive techniques - X-ray (Pesicka et al., 2003) or neutron diffraction (Christien et al., 2013) - are available to assess dislocation densities. Such techniques should be used in future studies to measure the evolution of dislocation densities as a function of strain and crystallographic orientations to further validate the constitutive equations.

This study focuses on the hardening behaviour of stainless steel single crystals prior to failure. An important avenue for future research is to consider the finite strain behaviour of notched specimens. Notched and compact tensile specimens are commonly used to quantify and evaluate the mechanisms governing the fracture of materials. In particular, notches act as stress triaxiality risers and therefore promote the typical mechanisms of ductile fracture (nucleation, growth and coalescence of voids). Despite the wealth of studies on the fracture of stainless steels (Mills, 1997), experimental data on their fracture at the single crystal scale are still lacking in the literature. Such studies are needed to evaluate and calibrate ductile fracture models that take into account the anisotropy induced by crystal plasticity (Han et al., 2013; Paux et al., 2015; Ling et al., 2016; Paux et al., 2018; Scherer et al., 2021; Paux et al., 2022). In addition, the effects of grain boundaries were not experimentally analysed in this work, as only single crystal specimens were tested. However, grain boundaries are known to play a critical role in the overall behaviour of stainless steels. Now that the bulk behaviour of stainless steel single crystals is well captured by the calibrated model presented in this study, further experimental work will be carried out on oligo-crystal specimens composed of a few grains (Delaire et al., 2000; Lim et al., 2015). Measurements in the vicinity of grain boundaries coupled with numerical simulations will be used to challenge the grain boundary model proposed by Haouala et al. (2020).

- **Numerical**

  The plasticity behaviour of austenitic stainless steels is determined by different microscopic phenomena depending on the applied conditions, the chemical composition of the alloy and the material state (hardened, irradiated) (Meric de Bellefon and van Duysen, 2016). At high temperatures and / or low strains, slip is the dominant mechanism as modelled in this study. However, twinning is also observed for example at room temperature in addition to slip (Karaman et al., 2001). Twin formation is also observed in highly irradiated austenitic stainless steels deformed at high temperature (Renault-Laborne et al., 2018). A complete set of crystal-scale constitutive equations for austenitic stainless steels therefore requires the inclusion of mechanical twinning as a potential microscopic plastic behaviour. Models have been proposed in the literature for other materials (Roters et al., 2010), which remain to be incorporated and calibrated to the model used in this study.

  As observed in the micro-compression experiments in this study on 316L steel and other studies on 304L steel (Paccou et al., 2019), size effects arise when the specimen size becomes comparable to the intrinsic length scale of plasticity. In a future study, we will introduce the role of GND through a strain gradient plasticity approach (Gurtin, 2002). Marano et al. (2021) has already used this approach to eliminate kink bands in favour of slip bands by introducing a kinematic strain gradient hardening term proportional to the *curl* of Nye's tensor. Alternatively, a Cosserat theory could be adopted to efficiently penalise lattice rotation gradients (Forest et al., 1997). Such higher-order theories will naturally introduce a material length scale and predict a harder response of the micropillar specimens. Since a direct measurement of this material length is still an open question, it could, in principle, be calibrated with the micro-compression curves measured in this work for several micropillar sizes. In polycrystals, the grain size effect is also significant. In addition, strain localisation phenomena occur in irradiated materials (Renault-Laborne et al., 2018) or at incipient fracture (Morin et al., 2018). Material length scales must be included in the model formulation in order to capture

size effects or to regularise strain localisation. Strain gradient crystal plasticity models naturally introduce such length scales (Cordero et al., 2012). Calibration of the material length scales involved in strain gradient plasticity remains a challenge which needs to be addressed in future studies.

In this work we have used a viscoplastic model of crystal plasticity. However, the viscosity parameters $K$ and $n$ were chosen in order to enforce a very weak rate sensitivity of the material behaviour over a wide range of strain rates. The main purpose of the viscoplastic approach was to regularise corners and edges of the crystal plasticity yield surface where the flow direction is not uniquely defined. It is known that this approach can lead to a poor conditioning of the system of governing equations when $n$ tends to infinity and $K$ tends to 0 (Wulfinghoff and Böhlke, 2013). Thus, a trade-off must be made between approximate rate-independence and numerical performance. Alternative approaches of (approximate) rate-independent crystal plasticity implementations are still being proposed in the literature in order to reduce the computational cost of crystal plasticity simulations (Miehe and Schröder, 2001; Schmidt-Baldassari, 2003; Busso and Cailletaud, 2005; Wulfinghoff and Böhlke, 2013; Forest and Rubin, 2016; Scheunemann et al., 2020; Petryk and Kursa, 2022; Mánik et al., 2022).

## 6. Conclusion

In this paper we propose, for the first time, a comprehensive calibration of a crystal plasticity model for AISI 316L stainless steel at room temperature and 300 °C based on experimental data obtained on a single crystal of this material. Resonant ultrasound spectroscopy, tensile and micro-compression tests were carried out on single crystal specimens. RUS data were used to calibrate the three cubic elasticity parameters $C_{11}$, $C_{12}$ and $C_{44}$ at room temperature. Molecular dynamics simulations were performed to calibrate the temperature dependence of these parameters. Screw and edge dislocation energies calculations were used to compute the temperature dependence of the isotropic equivalent shear modulus $\mu$ commonly used in the strain hardening law. Tensile test results at room temperature and 300 °C for different crystal orientations were used as a calibration database for the identification of strain hardening parameters. The identification was carried out on a number of material parameters that have an influence on the macroscopic stress-strain behaviour as revealed by sensitivity analysis. Some of these parameters are difficult to calibrate from DDD simulations alone. In particular, two coefficients of the interaction matrix relating to self and coplanar dislocation interactions were calibrated. In addition, the mean free path parameter relative to non-coplanar obstacles $K_{obs}$ and the dislocation annealing parameter $y$ were also calibrated. The constitutive behaviour calibrated on a material point was then tested on the real geometry of tensile specimens and on micro-compression specimens at 300 °C. The macroscopic tensile stress-strain behaviour is in good agreement with the experimental data and the in-plane Green-Lagrange strain fields obtained in the simulations are similar to the DIC strain fields. The agreement with micro-compression tests is more qualitative as these tests are tainted with more uncertainties. An effort has been made to test specimens of different sizes (diameter ranging between 2.93 and 12.83 µm), but it is not excluded that some size effects remain even in the largest specimens. Furthermore, the exact geometry (taper angle) and boundary conditions (friction coefficient, indenter misalignment) are less well known. Nevertheless, taking into account these uncertainties in the experimental conditions and the scatter in the experimental data, we show that the crystal plasticity model predicts behaviour in agreement with experiment. Finally we extend the model to the polycrystal scale. A Hall-Petch grain size effect is added into the model by introducing a phenomenological term into the dislocation evolution equations that depends on the distance of a material point to the nearest grain boundary. In this way, grain boundaries act as strong barriers, accumulating high dislocation densities and thus introducing the desired size effect.

Future work will be devoted to the experimental and numerical characterisation of the behaviour of oligocrystalline specimens. The role of grain boundaries and associated size effects can be modelled using the most advanced strain gradient plasticity models. Furthermore, the mechanisms of ductile fracture of stainless steels at the single crystal scale (Scherer et al., 2021; Sénac et al., 2023b,a) will be investigated in future work. Combining these two

aspects with the crystal plasticity model calibrated in this work will allow for reliable simulations of the strain hardening and ductile fracture of stainless steel polycrystals. The calibrated crystal plasticity model will also serve as a basis for future work on the mechanical behaviour of irradiated stainless steels (Ling et al., 2017; Scherer et al., 2019). Experiments on irradiated stainless steel single crystals will be required to calibrate the material parameters in relation to the evolution of irradiation defect densities.

## 7. Data availability

The numerical implementation of the crystal plasticity constitutive behaviour is available to download from https://doi.org/10.57745/KAFO01. Other data will be made available on request.


## Acknowledgements


## Appendix A. RUS measurements

The RUS method presented in Section 2.2 requires the fourth-order stiffness tensor $\mathbb{C}$. In the crystal frame and using Voigt notation

$$\mathbb{C}_{\text{Voigt}} = \begin{pmatrix} C_{11} & C_{12} & C_{12} & 0 & 0 & 0 \\ C_{12} & C_{11} & C_{12} & 0 & 0 & 0 \\ C_{12} & C_{12} & C_{11} & 0 & 0 & 0 \\ 0 & 0 & 0 & C_{44} & 0 & 0 \\ 0 & 0 & 0 & 0 & C_{44} & 0 \\ 0 & 0 & 0 & 0 & 0 & C_{44} \end{pmatrix} \tag{A.1}$$

However, since the crystal frame is not aligned with the axes of the sample at our disposal, we still have to apply a change of coordinate system to the matrix shown in Eq. A.1. This change of coordinate system is done directly on the Voigt representation of the elastic tensor using the so-called Bond matrix (Bond, 1943) and a Bunge convention representation of the Euler angles $[\varphi_1, \Phi, \varphi_2]$ describing the rotation around the ZXZ coordinate axes, applied from left to right (Rowenhorst et al., 2015). The elastic constants are then expressed as

$$C'_{kl} = M_{ki} C_{ij} M_{lj} \tag{A.2}$$

where $C'_{kl}$ are the elastic constants expressed in the rotated coordinate system, $C_{ij}$ are the original constants and $M$ is the following matrix

$$M = \begin{pmatrix} a_{11}^2 & a_{12}^2 & a_{13}^2 & 2a_{12}a_{13} & 2a_{13}a_{11} & 2a_{11}a_{12} \\ a_{21}^2 & a_{22}^2 & a_{23}^2 & 2a_{22}a_{23} & 2a_{23}a_{21} & 2a_{21}a_{22} \\ a_{31}^2 & a_{32}^2 & a_{33}^2 & 2a_{32}a_{33} & 2a_{33}a_{31} & 2a_{31}a_{32} \\ a_{21}a_{31} & a_{22}a_{32} & a_{23}a_{33} & a_{22}a_{33} + a_{23}a_{32} & a_{21}a_{33} + a_{23}a_{31} & a_{22}a_{31} + a_{21}a_{32} \\ a_{31}a_{11} & a_{32}a_{12} & a_{33}a_{13} & a_{12}a_{33} + a_{13}a_{32} & a_{13}a_{31} + a_{11}a_{33} & a_{11}a_{32} + a_{12}a_{31} \\ a_{11}a_{21} & a_{12}a_{22} & a_{13}a_{23} & a_{12}a_{23} + a_{13}a_{22} & a_{13}a_{21} + a_{11}a_{23} & a_{11}a_{22} + a_{12}a_{21} \end{pmatrix} \tag{A.3}$$

The $a_{ij}$ terms appearing in eq. A.3 are those of the rotation matrix in the Bunge convention. The matrix can be computed as follows

$$R(\varphi_1, \Phi, \varphi_2) = (a_{ij}) =$$

$$\begin{bmatrix} -\sin(\varphi_1)\sin(\varphi_2)\cos(\Phi) + \cos(\varphi_1)\cos(\varphi_2) & -\sin(\varphi_1)\cos(\Phi)\cos(\varphi_2) - \sin(\varphi_2)\cos(\varphi_1) & \sin(\Phi)\sin(\varphi_1) \\ \sin(\varphi_1)\cos(\varphi_2) + \sin(\varphi_2)\cos(\Phi)\cos(\varphi_1) & -\sin(\varphi_1)\sin(\varphi_2) + \cos(\Phi)\cos(\varphi_1)\cos(\varphi_2) & -\sin(\Phi)\cos(\varphi_1) \\ \sin(\Phi)\sin(\varphi_2) & \sin(\Phi)\cos(\varphi_2) & \cos(\Phi) \end{bmatrix} \tag{A.4}$$

Bayesian inversion method requires to provide *a priori* distributions for the unknown parameters. The following uniform distributions have been used:

- $C_{11} \in [100, 250]$ GPa
- $C_{12} \in [70, 200]$ GPa
- $C_{44} \in [70, 200]$ GPa
- $\varphi_1 \in [-10°, 100°]$
- $\Phi \in [-10°, 100°]$
- $\varphi_2 \in [-10°, 100°]$
- $\sigma \in [0, 5]$ kHz

The Euler angles used above were restricted to the given ranges due to symmetry reasons: since a 316L lattice is known to exhibit cubic anisotropy, we can restrict the optimization region to a principal region of the orientation space defined by the first $[0, 90°]$ sector of each angle. These are padded with 10 ° to allow for solutions existing on the edges of the implicitly periodic parameter space.

## Appendix B. Size effects in micropillar compression tests

Figure B.31 shows all the micropillar stress-strain curves obtained on the <112> and <111> orientations at 20 °C and 300 °C. Each subplot corresponds to one orientation and one temperature and combines all the curves corresponding to the three micropillar diameters tested. These plots clearly highlight the presence of a *smaller is stronger* type of size effect for this material at the micropillar scale. The smaller micropillars exhibit a stiffer behaviour and have a higher yield stress and strain hardening rate. In addition, the variability in the stress-strain response decreases as the micropillar diameter increases. These size effects can be explained by the depletion of dislocation sources as the specimen size decreases.

In addition, the curves at 300 °C are noisier than those at 20 °C. This suggests that there are more dislocation avalanches at 300 °C than there are at 20 °C and/or that the dislocation mobility is less uniform at 300 °C. At both temperatures, the noise amplitude observed on the stress-strain curves decreases with the micropillar diameter.

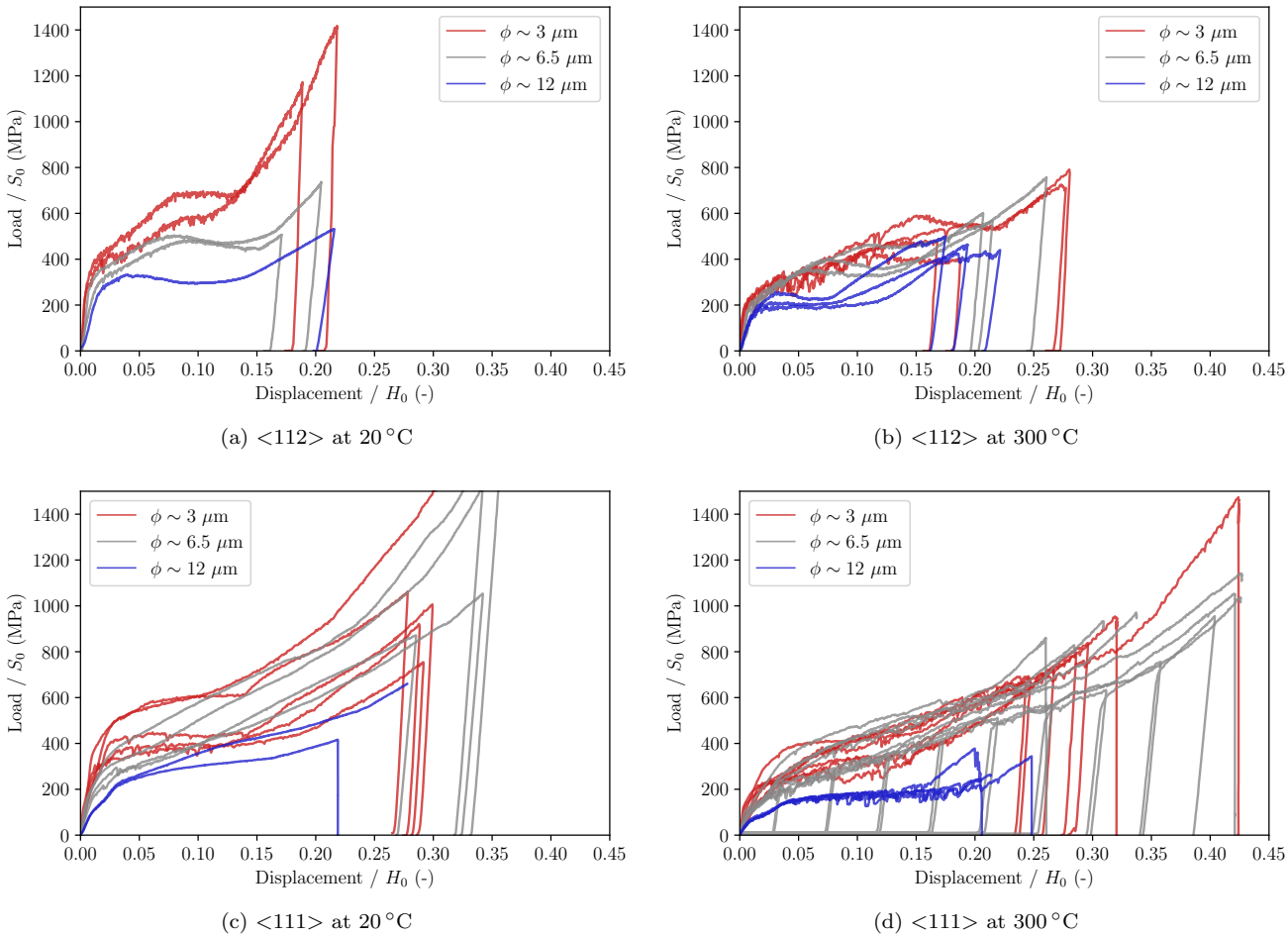


(a) <112> at 20 °C

(b) <112> at 300 °C

(c) <111> at 20 °C

(d) <111> at 300 °C

Figure B.31: Stress-strain curve of micropillar compression tests along (a-b) <112> and (c-d) <111> directions at 20 °C and 300 °C. Three micropillar diameters are tested for each orientation and temperature to quantify size effects.

## Appendix C. Active slip systems in finite element simulations

Figure C.32 shows the numerically predicted plastic slip fields at $\Delta L/L_0 = 0.05$. Figure C.32a can be compared to the experimental results post-processed with the SSLIP analysis shown in Figure 9b, while Figure C.32b is the numerical counterpart to Figure 10b. For both orientations the active slip systems in the numerical analysis are, as expected, those with the largest Schmid factors. The maximum amplitude of plastic slip is also well captured by the numerical simulations.

For the <111> specimen, the numerical analysis predicts that most of the plastic slip occurs on systems #11, #3 and #4, while the SSLIP analysis distributes the plastic slip over a larger number of slip systems (#5, #11, #8, #1, #4, #3). The presence of intense slip bands for slip system #11 is well captured by the finite element model. However, the simulation predicts a greater number of such bands than what is observed experimentally. In addition, the model fails to predict the experimentally observed slip bands in slip system #8 (which forms a strong collinear interaction with the most active system #11). This may possibly be due to uncertainties in the measured crystallographic orientation which is used in the numerical simulations. Additional finite element simulations (not shown here) carried out on slightly different crystallographic orientations have shown secondary slip bands on slip system #8 in regions complementary to slip system #11.

For the <011> specimen, the numerically predicted plastic slip is also distributed over fewer slip systems than what is obtained with the SSLIP analysis. The finite element simulations predict that most of the plastic deformation occurs on slip systems #2 and #10 (the two systems with the highest Schmid factors), while relatively little deformation is predicted on slip systems #3 and #11. Therefore, the amplitude of plastic slip predicted

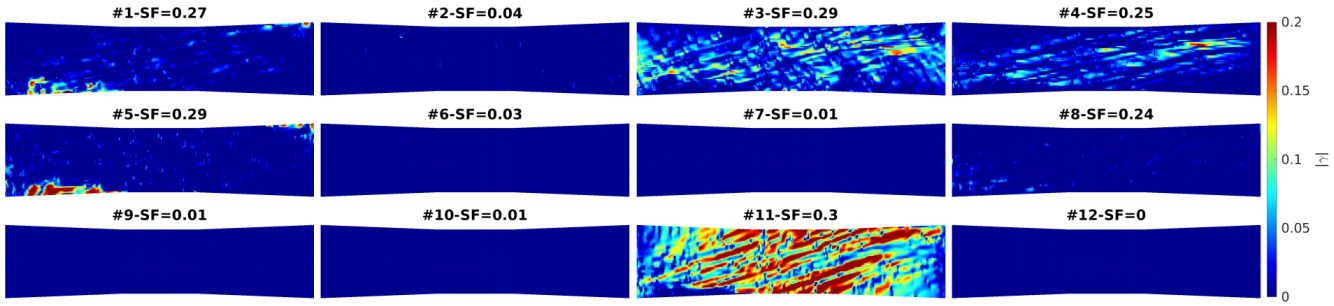


(a) <111>

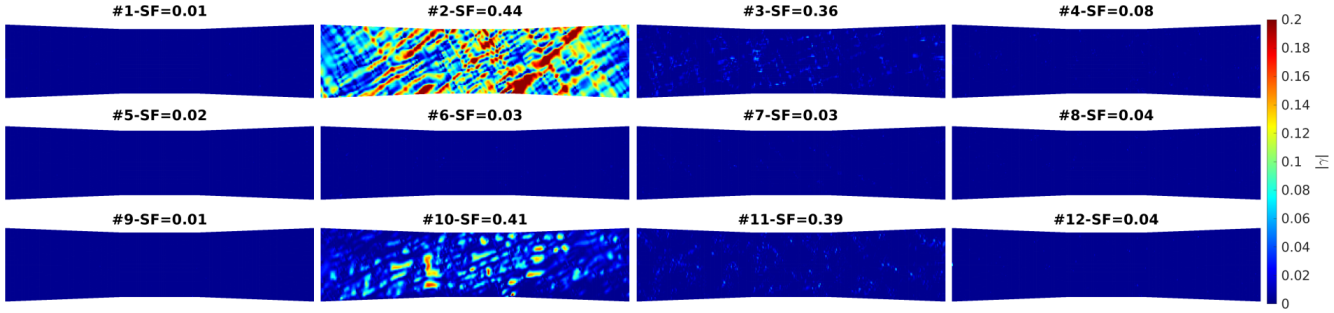


(b) <011>

Figure C.32: Slip system activity for each slip system obtained by the finite element analysis of the (a) <111> and (b) <011> specimens at $\Delta L/L_0 = 0.05$. The colour scale represents the absolute magnitude of the plastic slip.

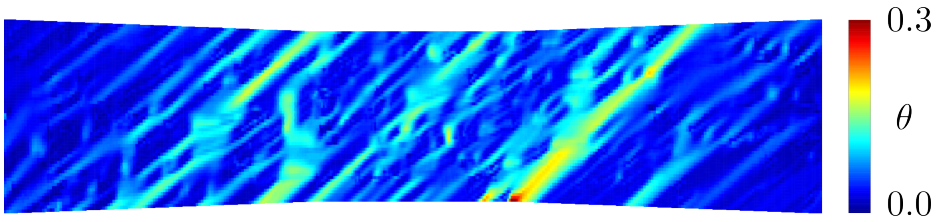


Figure C.33: Lattice rotation field $\theta$ in specimen <011> at $\Delta L/L_0 = 0.05$.

numerically on system #2 is about twice that obtained from the SSLIP analysis. It is interesting to note that the numerical simulation predicts both slip and kink bands (bands parallel and perpendicular to the slip direction) on system #2, while the SSLIP analysis favours the decomposition of the deformation over two slip systems #2 and #11 with a majority of slip bands and few or no kink bands. As discussed in Section 4.2, kink bands are associated with large lattice rotations and hence an increase in GND density. The lattice rotation field $\theta$ is plotted in Figure C.33. The lattice rotation is defined as the rotation angle obtained from the rotation matrix $\boldsymbol{R}$ in the following decomposition of the elastic part of the deformation gradient $\boldsymbol{E} = \boldsymbol{R} \cdot \boldsymbol{U}$, where $\boldsymbol{U}$ is the right stretch tensor. The role of GND and the resulting size effects are not considered in the present work, but a strain gradient plasticity approach will be developed in the future to capture these effects. For instance, strain gradient plasticity models, such as the one proposed by Marano et al. (2021), are known to penalise the formation of kink bands and thus promote the formation of slip bands.

## References

Abe, H., Watanabe, Y., 2008. Low-temperature aging characteristics of type 316L stainless steel welds: dependence on solidification mode. Metallurgical and Materials Transactions A 39, 1392–1398.

Anand, L., Kothari, M., 1996. A computational procedure for rate-independent crystal plasticity. Journal of the Mechanics and Physics of Solids 44, 525–558.

Azihari, R., 2023. Approche micromécanique et modélisation de la rupture intergranulaire - Application à la corrosion sous contrainte assistée par l'irradiation. Ph.D. thesis. CEA Saclay, Université Toulouse III - Paul Sabatier.

Bacon, D., Barnett, D., Scattergood, R.O., 1980. Anisotropic continuum theory of lattice defects. Progress in Materials Science 23, 51–262.

Bales, B., Petzold, L., Goodlet, B.R., Lenthe, W.C., Pollock, T.M., 2018. Bayesian inference of elastic properties with resonant ultrasound spectroscopy. The Journal of the Acoustical Society of America 143, 71–83.

Bernard, S., 2014. Resonant Ultrasound Spectroscopy for the Viscoelastic Characterization of Cortical Bone. Ph.D. thesis. Université Pierre et Marie Curie, Paris 6.

Besson, J., Foerch, R., 1998. Object-oriented programming applied to the finite element method: Part I - General concepts. Revue Européenne des Éléments Finis 7, 535–566.

Beyerlein, I., Tomé, C., 2008. A dislocation-based constitutive law for pure zr including temperature effects. International Journal of Plasticity 24, 867–895.

Blaber, J., Adair, B., Antoniou, A., 2015. Ncorr: open-source 2D digital image correlation matlab software. Experimental Mechanics 55, 1105–1122.

Blanchard, J., Damblin, G., Martinez, J., Arnaud, G., Gaudier, F., 2019. The Uranie platform: an open-source software for optimisation, meta-modelling and uncertainty analysis. EPJ Nuclear Sci. Technol. 5.

von Blanckenhagen, B., Gumbsch, P., Arzt, E., 2003. Dislocation sources and the flow stress of polycrystalline thin metal films. Philosophical Magazine Letters 83, 1–8.

Bond, W.L., 1943. The Mathematics of the Physical Properties of Crystals. Bell System Technical Journal 22, 1–72.

Bonny, G., Terentyev, D., Pasianot, R., Poncé, S., Bakaev, A., 2011. Interatomic potential to study plasticity in stainless steels: the FeNiCr model alloy. Modelling and simulation in materials science and engineering 19, 085008.

Borgioli, F., Fossati, A., Galvanetto, E., Bacci, T., Pradelli, G., 2006. Glow discharge nitriding of AISI 316L austenitic stainless steel: Influence of treatment pressure. Surface and Coatings Technology 200, 5505–5513.

Bourdin, F., Stinville, J., Echlin, M., Callahan, P., Lenthe, W., Torbet, C., Texier, D., Bridier, F., Cormier, J., Villechaise, P., et al., 2018. Measurements of plastic localization by heaviside-digital image correlation. Acta Materialia 157, 307–325.

Bridgman, P.W., 2013. Certain physical properties of single crystals of tungsten, antimony, bismuth, tellurium, cadmium, zinc, and tin. Harvard University Press.

Busso, E.P., Cailletaud, G., 2005. On the selection of active slip systems in crystal plasticity. International Journal of Plasticity 21, 2212–2231.

Canadinc, D., Sehitoglu, H., Maier, H., Chumlyakov, Y., 2005. Strain hardening behavior of aluminum alloyed Hadfield steel single crystals. Acta Materialia 53, 1831 – 1842.

Chen, Z., Daly, S., 2017. Active slip system identification in polycrystalline metals by digital image correlation (DIC). Experimental Mechanics 57, 115–127.

Christien, F., Telling, M., Knight, K., 2013. Neutron diffraction in situ monitoring of the dislocation density during martensitic transformation in a stainless steel. Scripta Materialia 68, 506–509.

Cordero, N.M., Forest, S., Busso, E.P., 2012. Generalised continuum modelling of grain size effects in polycrystals. Comptes Rendus Mécanique 340, 261–274.

Czochralski, J., 1918. Ein neues verfahren zur messung der kristallisationsgeschwindigkeit der metalle. Zeitschrift für physikalische Chemie 92, 219–221.

Dehm, G., Jaya, B., Raghavan, R., Kirchlechner, C., 2018. Overview on micro- and nanomechanical testing: New insights in interface plasticity and fracture at small length scales. Acta Materialia 142, 248–282.

Delaire, F., Raphanel, J.L., Rey, C., 2000. Plastic heterogeneities of a copper multicrystal deformed in uniaxial tension: experimental study and finite element simulations. Acta Materialia 48, 1075–1087.

Demir, E., Raabe, D., 2010. Mechanical and microstructural single-crystal Bauschinger effects: Observation of reversible plasticity in copper during bending. Acta Materialia 58, 6055–6063.

Dequiedt, J., Denoual, C., Madec, R., 2015. Heterogeneous deformation in ductile FCC single crystals in biaxial stretching: the influence of slip system interactions. Journal of the Mechanics and Physics of Solids 83, 301–318.

Devincre, B., Kubin, L., Hoc, T., 2006. Physical analyses of crystal plasticity by DD simulations. Scripta Materialia 54, 741–746.

Devincre, B., Kubin, L., Hoc, T., 2007. Collinear superjogs and the low-stress response of fcc crystals. Scripta Materialia 57, 905–908.

Douin, J., 2023. DisDi. URL: http://joel.douin.free.fr/Disdi-Page.html.

Dumas, M., Kermouche, G., Valiorgue, F., Van Robaeys, A., Lefebvre, F., Brosse, A., Karaouni, H., Rech, J., 2021. Turning-induced surface integrity for a fillet radius in a 316L austenitic stainless steel. Journal of Manufacturing Processes 68, 222–230.

El Shawish, S., Mede, T., Hure, J., 2021. A single grain boundary parameter to characterize normal stress fluctuations in materials with elastic cubic grains. European Journal of Mechanics-A/Solids 89, 104293.

Feaugas, X., Haddou, H., 2003. Grain-size effects on tensile behavior of nickel and AISI 316L stainless steel. Metallurgical and materials transactions A 34, 2329–2340.

Foreman-Mackey, D., Hogg, D.W., Lang, D., Goodman, J., 2013. emcee: The mcmc hammer. PASP 125, 306–312.

Forest, S., Cailletaud, G., Sievert, R., 1997. A Cosserat theory for elastoviscoplastic single crystals at finite deformation. Archives of Mechanics 49, 705–736.

Forest, S., Rubin, M., 2016. A rate-independent crystal plasticity model with a smooth elastic–plastic transition and no slip indeterminacy. European Journal of Mechanics-A/Solids 55, 278–288.

Franciosi, P., Berveiller, M., Zaoui, A., 1980. Latent hardening in copper and aluminium single crystals. Acta Metallurgica 28, 273–283.

Gélébart, L., 2020. A modified fft-based solver for the mechanical simulation of heterogeneous materials with dirichlet boundary conditions. Comptes Rendus. Mécanique 348, 693–704.

Goodlet, B.R., Mills, L., Bales, B., Charpagne, M.A., Murray, S.P., Lenthe, W.C., Petzold, L., Pollock, T.M., 2018. Elastic Properties of Novel Co- and CoNi-Based Superalloys Determined through Bayesian Inference and Resonant Ultrasound Spectroscopy. Metallurgical and Materials Transactions A 49, 2324–2339.

Greer, J.R., De Hosson, J.T., 2011. Plasticity in small-sized metallic systems: Intrinsic versus extrinsic size effect. Progress in Materials Science 56, 654–724.

Gurtin, M.E., 2002. A gradient theory of single-crystal viscoplasticity that accounts for geometrically necessary dislocations. Journal of the Mechanics and Physics of Solids 50, 5–32.

Gurtin, M.E., 2006. The Burgers vector and the flow of screw and edge dislocations in finite-deformation single-crystal plasticity. Journal of the Mechanics and Physics of Solids 54, 1882–1898.

Gurtin, M.E., 2008. A finite-deformation, gradient theory of single-crystal plasticity with free energy dependent on densities of geometrically necessary dislocations. International Journal of Plasticity 24, 702–725.

Gélébart, L., 2023. AMITEX_FFTP URL: https://amitexfftp.github.io/AMITEX/index.html.

Han, X., 2012. Modélisation de la fragilisation due au gonflement dans les aciers inoxydables austénitiques irradiés. Ph.D. thesis. CEA Saclay, École des Mines de Paris.

Han, X., Besson, J., Forest, S., Tanguy, B., Bugat, S., 2013. A yield function for single crystals containing voids. International Journal of Solids and Structures 50, 2115–2131.

Hanriot, F., Cailletaud, G., Remy, L., 1991. Mechanical behaviour of a nickel-based superalloy single crystal. A. Freed, K. Walker, Editeurs: High temperature constitutive modelling-Theory and application, ASME, New-York , 139–150.

Haouala, S., Alizadeh, R., Bieler, T., Segurado, J., LLorca, J., 2020. Effect of slip transmission at grain boundaries in Al bicrystals. International Journal of Plasticity 126, 102600.

Helfer, T., Michel, B., Proix, J., Salvo, M., Sercombe, J., Casella, M., 2015. Introducing the open-source `MFront` code generator: Application to mechanical behaviours and material knowledge management within the pleiades fuel element modelling platform. Computers & Mathematics with Applications 70, 994–1023.

Helfer, T., Michel, B., Proix, J.M., Salvo, M., Sercombe, J., Casella, M., . Introducing the open-source mfront code generator: Application to mechanical behaviours and material knowledge management within the PLEIADES fuel element modelling platform. Computers & Mathematics with Applications 70, 994–1023.

Hure, J., El Shawish, S., Cizelj, L., Tanguy, B., 2016. Intergranular stress distributions in polycrystalline aggregates of irradiated stainless steel. Journal of Nuclear Materials 476, 231 – 242.

Hure, J., Scherer, J.M., 2023. MFront implementation of a crystal plasticity law for 300 series austenitic stainless steels. doi:10.57745/KAFO01.

Jiang, M., Devincre, B., Monnet, G., 2019. Effects of the grain size and shape on the flow stress: A dislocation dynamics study. International Journal of Plasticity 113, 111–124.

Karaman, I., Sehitoglu, H., Gall, K., Chumlyakov, Y., Maier, H., 2000. Deformation of single crystal Hadfield steel by twinning and slip. Acta Materialia 48, 1345 – 1359.

Karaman, I., Sehitoglu, H., Maier, H., Chumlyakov, Y., 2001. Competing mechanisms and modeling of deformation in austenitic stainless steel single crystals with and without nitrogen. Acta Materialia 49, 3919–3933.

Keh, A.S., Nakada, Y., 1967. Plasticity of iron single crystals. Canadian Journal of Physics 45, 1101–1120.

Kocks, U., Mecking, H., 2003. Physics and phenomenology of strain hardening: the FCC case. Progress in Materials Science 48, 171–273.

Kocks, U.F., 1976. Laws for Work-Hardening and Low-Temperature Creep. Journal of Engineering Materials and Technology 98, 76–85.

Kothari, M., Anand, L., 1998. Elasto-viscoplastic constitutive equations for polycrystalline metals: application to tantalum. Journal of the Mechanics and Physics of Solids 46, 51–83.

Kubin, L., 2013. Dislocations, Mesoscale Simulations and Plastic Flow. Oxford University Press.

Kubin, L., Devincre, B., Hoc, T., 2008. Modeling dislocation storage rates and mean free paths in face-centered cubic crystals. Acta materialia 56, 6040–6049.

Kubin, L., Hoc, T., Devincre, B., 2009. Dynamic recovery and its orientation dependence in face-centered cubic crystals. Acta Materialia 57, 2567–2575.

Kuhlmann-Wilsdorf, D., 1999. The theory of dislocation-based crystal plasticity. Philosophical Magazine A 79, 955–1008.

Ledbetter, H., 1984. Monocrystal–polycrystal elastic constants of a stainless steel. Phys. Stat. Sol. 85, 89–96.

Ledbetter, H., 1985a. Monocrystal elastic constants in the ultrasonic study of welds. Ultrasonics 23, 9–13.

Ledbetter, H.M., 1985b. Monocrystal elastic constants in the ultrasonic study of welds. Ultrasonics 23, 9–13.

Lim, H., Carroll, J.D., Battaile, C.C., Boyce, B.L., Weinberger, C.R., 2015. Quantitative comparison between experimental measurements and CP-FEM predictions of plastic deformation in a tantalum oligocrystal. International Journal of Mechanical Sciences 92, 98–108.

Ling, C., Besson, J., Forest, S., Tanguy, B., Latourte, F., Bosso, E., 2016. An elastoviscoplastic model for porous single crystals at finite strains and its assessment based on unit cell simulations. International Journal of Plasticity 84, 58–87.

Ling, C., Tanguy, B., Besson, J., Forest, S., Latourte, F., 2017. Void growth and coalescence in triaxial stress fields in irradiated FCC single crystals. Journal of Nuclear Materials 492, 157–170.

Madec, R., Devincre, B., Kubin, L., Hoc, T., Rodney, D., 2003. The role of collinear interaction in dislocation-induced hardening. Science 301, 1879–1882.

Madec, R., Kubin, L.P., 2017. Dislocation strengthening in FCC metals and in BCC metals at high temperatures. Acta Materialia 126, 166–173.

Mandel, J., 1973. Equations constitutives et directeurs dans les milieux plastiques et viscoplastiques. International Journal of Solids and Structures 9, 725–740.

Mánik, T., Asadkandi, H., Holmedal, B., 2022. A robust algorithm for rate-independent crystal plasticity. Computer Methods in Applied Mechanics and Engineering 393, 114831.

Marano, A., Gélébart, L., Forest, S., 2021. FFT-based simulations of slip and kink bands formation in 3D polycrystals: influence of strain gradient crystal plasticity. Journal of the Mechanics and Physics of Solids 149, 104295.

Marshall, P., 1984. Austenitic stainless steels: microstructure and mechanical properties. Springer Science & Business Media.

Méric, L., Poubanne, P., Cailletaud, G., 1991. Single Crystal Modeling for Structural Calculations: Part 1—Model Presentation. Journal of Engineering Materials and Technology 113, 162–170.

Meric de Bellefon, G., van Duysen, J., 2016. Tailoring plasticity of austenitic stainless steels for nuclear applications: Review of mechanisms controlling plasticity of austenitic steels below 400°C. Journal of Nuclear Materials 475, 168–191.

Miehe, C., Schröder, J., 2001. A comparative study of stress update algorithms for rate-independent and rate-dependent crystal plasticity. International Journal for Numerical Methods in Engineering 50, 273–298.

Migliori, A., Sarrao, J., Visscher, W.M., Bell, T., Lei, M., Fisk, Z., Leisure, R., 1993. Resonant ultrasound spectroscopic techniques for measurement of the elastic moduli of solids. Physica B: Condensed Matter 183, 1–24.

Mills, W., 1997. Fracture toughness of type 304 and 316 stainless steels and their welds. International Materials Reviews 42, 45–82.

Monnet, G., Mai, C., 2019. Prediction of irradiation hardening in austenitic stainless steels: Analytical and crystal plasticity studies. Journal of Nuclear Materials 518, 316–325.

Morin, D., Hopperstad, O.S., Benallal, A., 2018. On the description of ductile fracture in metals by the strain localization theory. International Journal of Fracture 209, 27–51.

Morris, M., 1991. Factorial sampling plans for preliminary computational experiments. Technometrics 33, 161–174.

Mukherjee, T., DebRoy, T., 2019. Printability of 316 stainless steel. Science and Technology of Welding and Joining 24, 412–419.

Nieto-Valeiras, E., Haouala, S., LLorca, J., 2022. On the effect of slip transfer at grain boundaries on the strength of FCC polycrystals. European Journal of Mechanics - A/Solids 91, 104427.

Nix, W.D., Gao, H., 1998. Indentation size effects in crystalline materials: a law for strain gradient plasticity. Journal of the Mechanics and Physics of Solids 46, 411–425.

Paccou, E., 2019. Etude de l'évolution des propriétés mécaniques et de la sensibilité à la fissuration intergranulaire en fonction de la microstructure d'irradiation d'un acier 304 irradié aux ions lourds. Ph.D. thesis. CEA Saclay, Université Toulouse III - Paul Sabatier.

Paccou, E., Tanguy, B., Legros, M., 2019. Micropillar compression study of fe-irradiated 304l steel. Scripta Materialia 172, 56–60.

Paux, J., Brenner, R., Kondo, D., 2018. Plastic yield criterion and hardening of porous single crystals. International Journal of Solids and Structures 132, 80–95.

Paux, J., Morin, L., Brenner, R., 2022. A model of porous plastic single crystals based on fractal slip lines distribution. Journal of the Mechanics and Physics of Solids 167, 104948.

Paux, J., Morin, L., Brenner, R., Kondo, D., 2015. An approximate yield criterion for porous single crystals. European Journal of Mechanics-A/Solids 51, 1–10.

Pawel, J., Rowcliffe, A., Lucas, G., Zinkle, S., 1996. Irradiation performance of stainless steels for ITER application. Journal of nuclear materials 239, 126–131.

Pesicka, J., Kuzel, R., Dronhofer, A., Eggeler, G., 2003. The evolution of dislocation density during heat treatment and creep of tempered martensite ferritic steels. Acta Materialia 51, 4847–4862.

Petryk, H., Kursa, M., 2022. Crystal plasticity algorithm based on the quasi-extremal energy principle. International Journal for Numerical Methods in Engineering 123, 3285–3316.

Pineau, A., 2006. Development of the local approach to fracture over the past 25 years: theory and applications, in: Advances in Fracture Research. Springer, pp. 139–166.

Quey, R., Dawson, P., Barbe, F., 2011. Large-scale 3D random polycrystals for the finite element method: Generation, meshing and remeshing. Computer Methods in Applied Mechanics and Engineering 200, 1729–1745.

Raffaitin, A., Monceau, D., Crabos, F., Andrieu, E., 2007. The effect of thermal cycling on the high-temperature creep behaviour of a single crystal nickel-based superalloy. Scripta Materialia 56, 277–280.

Rashid, M., Nemat-Nasser, S., 1992. A constitutive algorithm for rate-dependent crystal plasticity. Computer Methods in Applied Mechanics and Engineering 94, 201–228.

Renault-Laborne, A., Hure, J., Malaplate, J., Gavoille, P., Sefta, F., Tanguy, B., 2018. Tensile properties and deformation microstructure of highly neutron-irradiated 316 stainless steels at low and fast strain rate. Journal of Nuclear Materials 508, 488–504.

Rossin, J., Leser, P., Pusch, K., Frey, C., Murray, S.P., Torbet, C.J., Smith, S., Daly, S., Pollock, T.M., 2021. Bayesian inference of elastic constants and texture coefficients in additively manufactured cobalt-nickel superalloys using resonant ultrasound spectroscopy. Acta Materialia 220, 117287.

Roters, F., Eisenlohr, P., Bieler, T.R., Raabe, D., 2011. Crystal plasticity finite element methods: in materials science and engineering. John Wiley & Sons.

Roters, F., Eisenlohr, P., Hantcherli, L., Tjahjanto, D., Bieler, T., Raabe, D., 2010. Overview of constitutive laws, kinematics, homogenization and multiscale methods in crystal plasticity finite-element modeling: Theory, experiments, applications. Acta Materialia 58, 1152–1211.

Rowenhorst, D., Rollett, A.D., Rohrer, G.S., Groeber, M., Jackson, M., Konijnenberg, P.J., Graef, M.D., 2015. Consistent representations of and conversions between 3D rotations. Modelling and Simulation in Materials Science and Engineering 23, 083501.

Saltelli, A., Tarantola, S., Campolongo, F., Ratto, M., 2004. Sensitivity analysis in practice. Wiley.

Scherer, J.M., Besson, J., 2022. Implementation of constitutive equations for single crystals in finite element codes, in: Nickel Base Single Crystals Across Length Scales. Elsevier, pp. 473–494.

Scherer, J.M., Besson, J., Forest, S., Hure, J., Tanguy, B., 2019. Strain gradient crystal plasticity with evolving length scale: Application to voided irradiated materials. European Journal of Mechanics-A/Solids 77, 103768.

Scherer, J.M., Besson, J., Forest, S., Hure, J., Tanguy, B., 2021. A strain gradient plasticity model of porous single crystal ductile fracture. Journal of the Mechanics and Physics of Solids 156, 104606.

Scheunemann, L., Nigro, P., Schröder, J., Pimenta, P., 2020. A novel algorithm for rate independent small strain crystal plasticity based on the infeasible primal-dual interior point method. International Journal of Plasticity 124, 1–19.

Schmidt-Baldassari, M., 2003. Numerical concepts for rate-independent single crystal plasticity. Computer Methods in Applied Mechanics and Engineering 192, 1261–1280.

Sénac, C., Hure, J., Tanguy, B., 2023a. Void growth yield criteria for intergranular ductile fracture. Journal of the Mechanics and Physics of Solids 172, 105167.

Sénac, C., Hure, J., Tanguy, B., 2023b. Yield surface for void growth and coalescence of porous anisotropic materials under axisymmetric loading. Journal of the Mechanics and Physics of Solids , 105365.

Shen, S., Atluri, S., 2004. Atomic-level stress calculation and continuum-molecular system equivalence. Computer Modeling in Engineering and Sciences 6, 91–104.

Song, R.B., Xiang, J.Y., Hou, D.P., 2011. Characteristics of mechanical properties and microstructure for 316L austenitic stainless steel. Journal of Iron and Steel Research International 18, 53–59.

Stockbarger, D.C., 1936. The production of large single crystals of lithium fluoride. Review of Scientific Instruments 7, 133–136.

Subramaniyan, A.K., Sun, C., 2008. Continuum interpretation of virial stress in molecular simulations. International Journal of Solids and Structures 45, 4340–4346.

Syed, B., Geng, J., Mishra, R., Kumar, K., 2012. [0001] compression response at room temperature of single-crystal magnesium. Scripta Materialia 67, 700 – 703.

Taylor, G.I., Elam, C.F., 1925. The plastic extension and fracture of aluminium crystals. Proceedings of the Royal Society of London. Series A, Containing Papers of a Mathematical and Physical Character 108, 28–51.

Teodosiu, C., Raphanel, J., Tabourot, L., 1993. Finite element simulation of the large elastoplastic deformation of multicrystals, in: Teodosiu, C., Raphanel, J., Sidoroff, F. (Eds.), Large Plastic Deformations: Fundamental Aspects and Applications to Metal Forming (1st ed.). Routledge, pp. 153–168.

Trelewicz, J.R., Halada, G.P., Donaldson, O.K., Manogharan, G., 2016. Microstructure and corrosion resistance of laser additively manufactured 316L stainless steel. Jom 68, 850–859.

URANIE, 2020. Methodological reference guide for URANIE v4.4.0.

Vermeij, T., Peerlings, R., Geers, M., Hoefnagels, J., 2023. Automated identification of slip system activity fields from digital image correlation data. Acta Materialia 243, 118502.

Viat, A., Guillonneau, G., Fouvry, S., Kermouche, G., Sao Joao, S., Wehrs, J., Michler, J., Henne, J.F., 2017. Brittle to ductile transition of tribomaterial in relation to wear response at high temperatures. Wear 392, 60–68.

Visscher, W.M., Migliori, A., Bell, T.M., Reinert, R.A., 1991. On the normal modes of free vibration of inhomogeneous and anisotropic elastic objects. The Journal of the Acoustical Society of America 90, 2154–2162.

Von Blanckenhagen, B., Gumbsch, P., Arzt, E., 2001. Dislocation sources in discrete dislocation simulations of thin-film plasticity and the hall-petch relation. Modelling and Simulation in Materials Science and Engineering 9, 157.

Wheeler, J., Michler, J., 2013. Elevated temperature, nano-mechanical testing in situ in the scanning electron microscope. Review of Scientific Instruments 84.

Wheeler, J., Niederberger, C., Tessarek, C., Christiansen, S., Michler, J., 2013. Extraction of plasticity parameters of GaN with high temperature, in situ micro-compression. International Journal of Plasticity 40, 140–151.

Wulfinghoff, S., Böhlke, T., 2013. Equivalent plastic strain gradient crystal plasticity–enhanced power law subroutine. GAMM-Mitteilungen 36, 134–148.

Xiao, X., Song, D., Xue, J., Chu, H., Duan, H., 2015a. A self-consistent plasticity theory for modeling the thermomechanical properties of irradiated fcc metallic polycrystals. Journal of the Mechanics and Physics of Solids 78, 1–16.

Xiao, X., Song, D., Xue, J., Chu, H., Duan, H., 2015b. A size-dependent tensorial plasticity model for fcc single crystal with irradiation. International Journal of Plasticity 65, 152–167.